Max-Planck-Institut für Intelligente Systeme
(ehemals Max-Planck-Institut für Metallforschung)
Stuttgart

Precipitation of nitrides in iron-based binary and ternary alloys; influence of defects and transformation-misfit stresses

Maryam Akhlaghi

Dissertation
an der
Universität Stuttgart

Bericht Nr. 252
November 2015

Precipitation of nitrides in iron-based binary and ternary alloys; influence of defects and transformation-misfit stresses

Von der Fakultät Chemie der Universität Stuttgart zur Erlangung

der Würde eines Doktors der Naturwissenschaften (Dr. rer. nat.)

genehmigte Abhandlung

Vorgelegt von

Maryam Akhlaghi

aus Teheran, Iran

Hauptberichter:	Prof. Dr. Ir. E. J. Mittemeijer
Mitberichter:	Prof. Dr. J. Bill
Prüfungsvorsitzender:	Prof. Dr. T. Schleid

Tag der Einreichung:	16.09.2015
Tag der mündlichen Prüfung:	25.11.2015

MAX-PLANCK-INSTITUT FÜR INTELLIGENTE SYSTEME
(ehemals MAX-PLANCK-INSTITUT FÜR METALLFORSCHUNG)
INSTITUT FÜR MATERIALWISSENSCHAFT DER UNIVERSITÄT STUTTGART

2015

Table of contents

Chapter 1. Introduction **1**
1.1. General introduction 1
1.2. Microstructure of nitrided region 1
1.3. Nitriding of binary and ternary Fe-based alloys 2
1.4. Residual stress development in nitrided specimens 3
1.4.1. Development of hydrostatic strain in nitrided case 3
1.4.2. Development of residual macrostresses in nitrided case and unnitrided core 3
1.5. Residual stress development in nitrided specimens 5
1.5.1. The definition of nitriding potential (r_N) 5
1.5.2. Stressed-solid/gas-phase thermodynamic equilibrium 6
1.6. Outline of the thesis 8
References 10

Chapter 2. Low temperature nitriding of ferritic Fe-Cr-Al alloys **15**
2.1. Introduction 16
2.2. Experimental 16
2.2.1. Specimen preparation and nitriding 16
2.2.2. Microstructural characterization 17
2.3. Results 18
2.3.1. Morphology of nitrided region 18
2.3.2. Simultaneous vs. successive precipitation of nitrides 19
2.4. Discussion 22
2.5. Conclusions 24
References 25

Chapter 3. Lattice-parameter change induced by accommodation of precipitate/matrix misfit; misfitting nitrides in ferrite **27**
3.1. Introduction 28

3.2. Elastic strain field in a misfitting system: lattice-parameter changes 29
3.2.1. Change of the lattice parameter of the matrix 29
3.2.2. Change of the lattice parameter of the misfitting phase 30
3.2.3. Change of the lattice parameter of the assembly (matrix plus misfitting phase) 30
3.2.4. Coherent vs. incoherent diffraction of matrix and misfitting precipitates; consequences for interpretation of lattice-parameter changes 31
3.3. Experimental 32
3.3.1. Specimen preparation 32
3.3.2. Nitriding and de-nitriding experiments 33
3.3.3. Specimen characterization 34
3.3.3.1. Weight measurement 34
3.3.3.2. Electron probe microanalysis (EPMA) 34
3.3.3.3. X-ray and synchrotron diffraction 34
3.4. Results and Evaluation 36
3.5. Discussion 38
3.6. Conclusions 43
Acknowledgements 44
References 44

Chapter 4. Diffraction-line shifts and broadenings in continuously and discontinuously coarsening precipitate-matrix systems; coarsening of initially coherent nitride precipitates in a ferrite matrix 49
4.1. Introduction 50
4.2. Experimental Procedures 51
4.2.1. Specimen preparation 51
4.2.2. Nitriding experiments 52
4.2.3. Specimen characterization 52
4.2.3.1. Weight measurement 52
4.2.3.2. Light microscopy (LM) 53
4.2.3.3. X-ray diffraction (XRD) analysis 53
4.2.3.4. Transmission electron microscopy (TEM) analysis 53
4.3. Results 53

4.3.1. Fe-2.0 at.%Cr alloy 53
4.3.2. Fe-4.5 at.%Cr alloy 56
4.4. Discussion 61
4.4.1. Initial state 61
4.4.2. Continuous Coarsening 63
4.4.3. Discontinuous Coarsening 64
4.5. Conclusions 65
Acknowledgements 67
References 67

Chapter 5. Misfit Induced Changes of Lattice Parameters in Two-Phase Systems: Coherent/Incoherent Precipitates in a Matrix 71
5.1. Introduction 72
5.1.1. micro-and macrostrains; coherent and incoherent diffraction 72
5.2. Lattice-parameter changes due to elastically accommodated misfit 73
5.2.1. Change of the lattice parameter of the matrix 73
5.2.2. Change of the lattice parameter of the misfitting phase 74
5.2.3. Change of the lattice parameter of the assembly (matrix plus misfitting phase) 75
5.2.4. The misfit parameter 75
5.3. Observations and discussion 76
5.3.1. Coherent diffraction by the assembly matrix plus second phase particles; transformation misfit 78
5.3.1.1. Misfitting coherent alloying element nitrides in ferrite 78
5.3.1.2. Misfitting coherent cobalt precipitates in copper 79
5.3.2. Incoherent diffraction of the matrix and second phase particles; transformation misfit 81
5.3.2.1. Misfitting incoherent nitrides in ferrite 81
5.3.3. Incoherent diffraction of the matrix and second phase particles; thermal misfit 83
5.3.3.1. Misfitting incoherent silicon in aluminum 83
5.3.3.2. Misfitting incoherent alloying element nitrides in ferrite 84
5.4. Conclusions 85
References 86

Chapter 6. Dependence of the nitriding rate of ferritic and austenitic substrates on the crystallographic orientation of surface grains; gaseous nitriding of Fe-Cr and Ni-Ti alloys **91**

6.1. Introduction 92

6.2. Theoretical background 93

6.2.1. Stressed-solid /gas-phase thermodynamic equilibrium 93

6.3. Experimental 97

6.3.1. Specimen preparation 97

6.3.2. Nitriding experiments 97

6.3.3. Specimen characterization 98

6.3.3.1. Light microscopy 98

6.3.3.2. X- ray diffraction (XRD) 98

6.3.3.3. Electron probe microanalysis (EPMA) 99

6.3.3.4. Electron backscatter diffraction (EBSD) 99

6.4. Results and evaluation 99

6.4.1. Dependence of surface nitrogen content and nitrided zone depth on crystallographic orientation of surface grains 100

6.4.1.1. Ni-Ti (fcc) specimens 100

6.4.1.2. Fe-Cr (bcc) specimens 100

6.4.2. Dependence of residual stress on crystallographic orientation of surface grains 103

6.4.2.1. Ni-Ti (fcc) specimens 103

6.4.2.2. Fe-Cr (bcc) specimens 105

6.5. General discussion 106

6.6. Conclusions 108

Acknowledgements 109

References 109

Chapter 7. Summary **115**

Chapter 8. Zusammenfassung in deutscher Sprache **119**

List of publications **123**

Acknowledgements **125**

Curriculum Vitae **127**

Introduction

1.1. General introduction

Nitriding is a thermochemical surface treatment widely applied to improve the mechanical (fatigue and wear resistances) and chemical (corrosion resistance) properties of metallic materials, in particular Fe-based alloys (steels) [1]. Compared to other processes, upon nitriding minor dimensional changes of the component occur, because of insignificant changes in the crystal structure of the matrix, i.e., no austenite to ferrite/martensite transformation occurs during the application of the nitriding heat treatment. Thus, nitriding is at present the most viable surface treatment process [2, 3].

During nitriding atomic nitrogen diffuses inwardly from the surface to the deeper regions of components. Provision of atomic nitrogen to the surface of specimen is feasible using different methods such as gaseous nitriding, plasma nitriding, laser nitriding and salt-bath nitriding. Due to accurate control of chemical potential of nitrogen in the nitriding atmosphere during gaseous nitriding, this method is mostly applied to achieve reproducible results [2]. Therefore, gaseous nitriding is the most suited nitriding method for fundamental investigations of the nitriding response of iron-based alloys. Upon gaseous nitriding by employing flowing ammonia/hydrogen gas mixture (NH_3/H_2), the atomic nitrogen released during heterogeneous decomposition of ammonia on the surface of steel diffuses into the steel specimen [1].

1.2. Microstructure of nitrided region

Upon the introduction of nitrogen from the surface into the steel components two different types of microstructures, known as diffusion zone and compound layer, develop. The diffusion zone developing just above the unnitrided core of specimen contains dissolved nitrogen and/or

alloying-element-nitrides in the ferrite matrix, whereas the compound layer developing above the diffusion zone consists of iron-nitrides (ε-Fe_3N_{1+y} and γ′-Fe_4N_{1-x}) (see Figure 0-1).

The technological importance of nitriding is derived from the pronounced increases of the resistances of treated components against fatigue (due to development of diffusion zone), wear and corrosion (due to development of the compound layer), which can be achieved by tuned applications of the nitriding process [1].

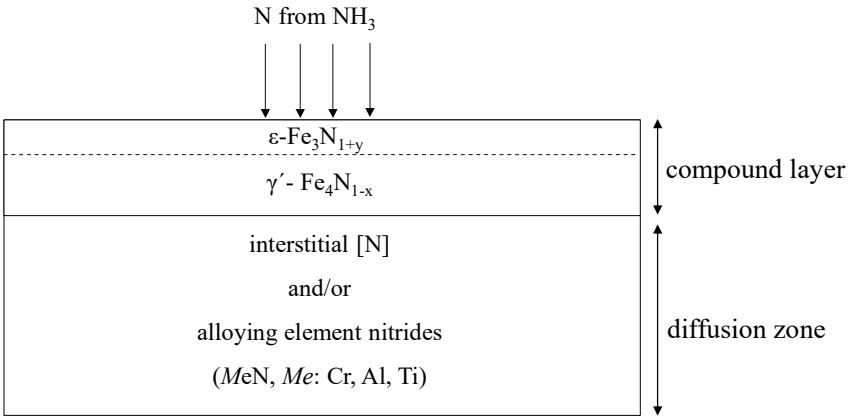

Figure 0-1. Schematic illustration of the nitrided zone of an iron-based specimen. The nitrided zone can be subdivided into the compound layer and the diffusion zone.

1.3. Nitriding of binary and ternary Fe-based alloys

The atomic nitrogen generated at the surface by dissociation of NH_3 gas gets incorporated into the surface of the specimen [2]. The inwardly diffusing nitrogen reacts with alloying elements in steel which have affinity for nitrogen (such as Cr, Al, Mo, Ti, Mn, Si) leading to the development of alloying element nitrides in ferrite matrix. Understanding the collective interaction of multiple alloying elements with inwardly diffusing nitrogen is important for understanding the nitriding behavior of steels [1, 4].

The nitriding response of binary Fe-based alloys has been investigated extensively; Fe-Cr [5-9]), Fe-Al [10, 11], Fe-V [12, 13], Fe-Ti [14-16] and Fe-Si [17-19]. Only few works have been devoted to the fundamental understanding of the nitride-precipitation process taking place in ternary iron-based alloys such as Fe-Cr-Al [20, 21], Fe-Cr-Ti [22, 23], Fe-Ni-Cr [24], Fe-Mo-Cu [25], Fe-Mo-Cr [26, 27], Fe-Al-Si [28], Fe-Mn-Si [29] and Fe-V-Si [30, 31]. In the case of some Si containing ternary Fe-based alloys (Fe-*Me*-Si alloy with *Me*=Ti, Cr and V) development of stable *amorphous* Si_3N_4 and cubic NaCl-type *Me*N nitrides occurs [30, 31]. However, it was shown that, in contrast to the

development of stable binary nitrides in some Si containing ternary Fe-based alloys, metastable ternary, "mixed" nitrides develop during nitriding of other ternary Fe-based alloys: cubic NaCl-type $Cr_{1-x}Al_xN$, $Cr_{1-x}Ti_xN$ and $Cr_{1-x}Mo_xN$ develop upon nitriding of Fe-Cr-Al, Fe-Cr-Ti and Fe-Cr-Mo alloys, respectively [26, 32, 33]. A triclinic $Mn_{1-x}Si_xN$ phase develops in nitrided in Fe-Mn-Si alloy [29].

In addition, it is generally recognized that characteristics of the unnitrided microstructure can decisively influence the nitride-precipitation process. Thus, investigations on recrystallized and cold-rolled specimens of binary Fe-Al [34, 35] and Fe-Mo [36] alloys have revealed that the crystal-lattice defects (dislocations) in cold-rolled specimens can lead to the development of different nitride modifications with enhanced rate of precipitation.

1.4. Residual stress development in nitrided specimens

In view of the formation of misfitting alloying element nitrides in the ferrite matrix of nitrided specimen and the elastic accommodation of misfit between the second phase (nitride) and the matrix, expansion of the matrix occurs due to the hydrostatic component of the misfit- stress field. Because of this hydrostatic component of stress, more nitrogen atoms can be dissolved in the dilated ferrite matrix which is called excess-dissolved nitrogen [15, 37].

The assembly in the nitrided zone of the specimen has a different volume as compared to the unnitrided zone (i.e. the nitrided zone demands for more space). The volume misfit between the nitrided zone and unnitrided zone of specimen brings about a macroscopic, residual, self-equilibrating stress in both nitrided and unnitrided zones [38]. In the following sections, detailed information on aforementioned types of stresses is provided.

1.4.1. Development of hydrostatic strain in nitrided case

A continuum theory for the fully elastic accommodation of the misfit of a point imperfection in a matrix has been presented by Eshelby [39, 40]. This theory can also be applied to the case of precipitation of misfitting second-phase particles in the matrix. As indicated above, alloying element nitrides (*Me*N) developing in the diffusion zone of nitrided specimen have a positive volume misfit with the ferrite matrix. Due to this, a tensile hydrostatic strain develops in the nitrided region of the specimen leading to increase of the lattice parameter of the ferrite matrix (see Figure 0-2(b)). This change in lattice parameter of the matrix can be predicted by applying Eshelby's theory [39, 40] (see chapter 3).

1.4.2. Development of residual macrostresses in nitrided case and unnitrided core

The development of residual macrostresses during nitriding is related to the difference in specific volume between the nitride and unnitrided regions, and can be described (in a simplified way) as follows:

Consider first an unnitrided specimen (see Figure 0-2(a)), during nitriding, alloying element nitrides (*Me*N) develops in the matrix and some part of N atoms dissolve in the matrix. As there is a difference in specific volume between the matrix and the nitrides and as described in section 1.4.1, a positive volume misfit occurs. Due to this volume misfit the nitrided layer tends to expand (see Figure 0-2(b)). However, in the case of partly nitrided specimen, the nitrided layer is attached to the unnitrided region, which obstructs free expansion of the nitrided region. Due to this elastic accommodation of the misfit between nitrided case and unnitrided core, the nitrided region experiences a distinct compressive residual stress parallel to the surface, whereas the unnitrided core experiences a modest tensile residual stress parallel to the surface (see Figure 0-2(c)).

The residual macrostresses can be taken as a biaxial, rotationally symmetric state of stress ($\sigma_{xx} = \sigma_{yy} \equiv \sigma_{//}$ and $\sigma_{zz} = 0$ with x, y and z as the principal axes for the state of stress and with the x and y axes in the plane of the surface and the z axis perpendicular to the surface) [41]. This state of stress can also affect the thermodynamics of gaseous nitriding, which has been dealt with in detail in section 1.5.2.

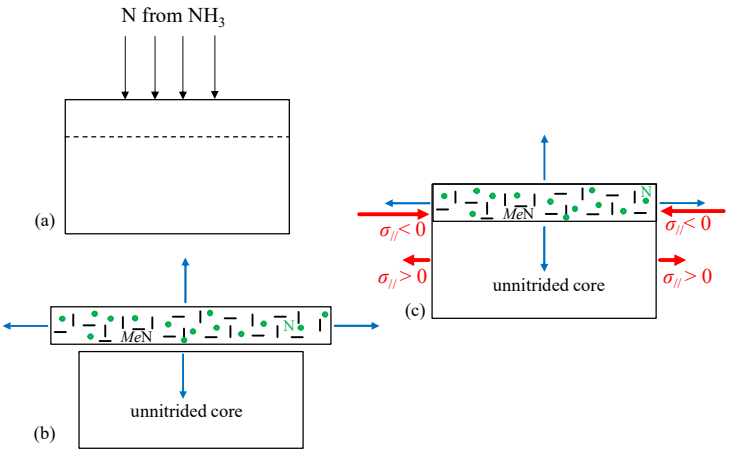

Figure 0-2. Schematic illustration of the hydrostatic strain and the residual macrostress development in a specimen during nitriding. (a) Atomic nitrogen from decomposition of ammonia gas enters the substrate upon nitriding (b) Expansion of nitrided region occurs as a result of the development of hydrostatic strain due to elastic accommodation of the misfit between developing coherent nitrides and matrix and also the interstitial dissolution of N atoms in ferrite matrix (blue arrows represent the hydrostatic expansion of nitrided region) (c) Development of biaxial self-equilibrating macrostresses ($\sigma_{//}$) on nitrided case (compressive stress; red arrows) and unnitrided core (tensile stress; red arrows).

1.5. Thermodynamics of gaseous nitriding

1.5.1. The definition of nitriding potential (r_N)

Gaseous nitriding is usually carried out in flowing ammonia/hydrogen gas mixture. The Gibbs energy of system is a state variable, which means that the route taken to reach a particular state has no effect on the value of the Gibbs energy of that state [42]. Therefore, nitriding in the flowing mixture of NH_3 and H_2 gases can be assumed as the sum of following (hypothetical) reactions [43]:

$$\frac{1}{2}\,\mathrm{N_2} \leftrightarrow [\mathrm{N}] \tag{1-1}$$

$$\mathrm{NH_3} \leftrightarrow \frac{1}{2}\mathrm{N_2} + \frac{3}{2}\mathrm{H_2} \tag{1-2}$$

The sum of the above hypothetical reactions gives the following overall reaction:

$$\mathrm{NH_3} \leftrightarrow [\mathrm{N}] + \frac{3}{2}\mathrm{H_2} \tag{1-3}$$

where [N] represents nitrogen dissolved in matrix. Here, it is assumed the occurrence of local equilibrium between the gas phase and the solid specimen [44].

Considering a state of equilibrium at the surface of the specimen, the chemical potential of nitrogen in the gaseous medium (μ_{N_2}) is the same as the chemical potential of dissolved nitrogen in the solid phase ($\mu_{[N]}$):

$$\frac{1}{2}\,\mu_{N_2} = \mu_{[N]} \tag{1-4}$$

According to the definition of the chemical potential [43], Eq. (1-4) leads to the following Eq. (1-5):

$$\frac{1}{2}\mu^{\circ}_{\mathrm{N_2}} + \frac{1}{2}\mathrm{R}T\ln\left[\frac{P_{\mathrm{N_2}}}{P^{\circ}}\right] = \mu^{\circ}_{\mathrm{N}} + \mathrm{R}T\ln[a_{\mathrm{N}}] \tag{1-5}$$

where $\mu^{\circ}_{N_2}$ and μ°_{N} are the chemical potentials of nitrogen in the reference states and a_N is the activity of dissolved nitrogen in solid phase. P_{N_2} is partial pressure of nitrogen gas in the nitriding medium and P° is the pressure of the gas in the reference state. The chemical potentials in the reference state can be selected in such a way as to satisfy Eq. (1-6):

$$\frac{1}{2}\mu^{\circ}_{N_2} = \mu^{\circ}_{N} \tag{1-6}$$

Thus, considering Eqs. (1-5) and (1-6), it follows:

$$a_N = \sqrt{\frac{P_{N_2}}{P^{\circ}}} \tag{1-7}$$

Eq. (1-7) shows the relation between the activity of dissolved nitrogen in solid phase and the (hypothetical) partial pressure of nitrogen gas in nitriding medium (P_{N_2}).

Now, by using the equilibrium constant for Eq. (1-3); $K_{(1.3)}$, a_N can be expressed as a function of the nitriding potential, r_N:

$$a_N = K_{(3)}\sqrt{P^{\circ}}\, r_N \tag{1-8}$$

where the nitriding potential can be written as: $r_N = P_{NH_3}/P_{H_2}^{3/2}$. Usually, the pressure of the reference state for the gas components is selected as one pressure unit (usually 1 atm).

The very low value of the equilibrium constant for Eq. (1-1), suggests that at the usual nitriding temperatures (450°C-580°C), several thousand atmospheres of nitrogen gas pressures are required to attain a significant value of activity of the nitrogen in the pure iron. Hence, it is impossible to achieve significant nitriding of iron and iron-alloys by employing nitrogen gas at atmospheric pressure [45]. According to Eq. (1-8), applying specific nitriding potential at the certain nitriding temperatures, it is possible to obtain different nitrided microstructures as discussed in section 1.2.

1.5.2. Stressed-solid/gas-phase thermodynamic equilibrium

The chemical potential of the nitrogen dissolved in a stress-free (iron) matrix phase ($\mu_{\mathrm{N}}^{\sigma=0}$) is related to the chemical potential of nitrogen in the standard state (μ_{N}°) and the activity of the dissolved nitrogen ($a_{\mathrm{N}}^{\sigma=0}$) [43]:

$$\mu_N^{\sigma=0} = \mu_N^{\circ} + RTlna_N^{\sigma=0} = \mu_N^{\circ} + RTln(C_N^{\sigma=0}\gamma_N^{\sigma=0}) \tag{1-9}$$

where R is the gas constant and T is the absolute temperature. The nitrogen activity can be written as the product of the corresponding nitrogen concentration ($C_{\mathrm{N}}^{\sigma=0}$) and the nitrogen activity coefficient ($\gamma_{\mathrm{N}}^{\sigma=0}$).

In the presence of the residual macrostress mentioned in section 1.4.2, the chemical potential of nitrogen dissolved in the stressed solid matrix phase ($\mu_{\mathrm{N}}^{\sigma\neq0}$) is described as:

$$\mu_N^{\sigma\neq0} = \mu_N^{\circ} + RTlna_N^{\sigma\neq0} = \mu_N^{\circ} + RTln(C_N^{\sigma\neq0}\gamma_N^{\sigma\neq0}) \tag{1-10}$$

where $a_{\mathrm{N}}^{\sigma\neq0}$ is the activity of nitrogen in the stressed matrix phase and $C_{\mathrm{N}}^{\sigma\neq0}$ and $\gamma_N^{\sigma\neq0}$ are the corresponding nitrogen concentration and nitrogen activity coefficient. Eq. (1-10) can be rewritten according to [46] as:

$$\mu_N^{\sigma\neq0} = \mu_N^{\circ} + RTln(C_N^{\sigma\neq0}\gamma_N^{\sigma=0}) - \bar{V}_N\sigma_h \tag{1-11}$$

where $\bar{V}_{\mathrm{N}}$ is the partial molar volume of nitrogen in the matrix phase and σ_{h} is the hydrostatic component of the state of stress acting on the matrix phase.

Once equilibrium has been attained at the surface of a stressed specimen and of a stress-free specimen with the *same* nitriding atmosphere of defined nitriding potential (at a certain temperature;), the chemical potentials of N in the stress-free specimen ($\mu_{\mathrm{N,eq}}^{\sigma=0}$) and of N in the stressed specimen ($\mu_{\mathrm{N,eq}}^{\sigma\neq0}$) are necessarily the same and equal to the chemical potential of N in the gaseous nitriding medium ($\mu_{\mathrm{N,eq}}^{\mathrm{gas}}$) (see also Eq. (1-4)):

$$\mu_{\mathrm{N,eq}}^{\sigma=0} = \mu_{\mathrm{N,eq}}^{\sigma\neq0} = \mu_{\mathrm{N,eq}}^{\mathrm{gas}} \tag{1-12}$$

Accordingly, it follows from Eqs. (1-9), (1-11) and (1-12) [47]:

$$\frac{C_{N,eq}^{\sigma\neq0}}{C_{N,eq}^{\sigma=0}} = exp\left(\frac{\bar{V}_N\sigma_h}{RT}\right) \quad (1\text{-}13)$$

where $C_{\mathrm{N,eq}}^{\sigma\neq0}$ and $C_{\mathrm{N,eq}}^{\sigma=0}$ are the equilibrium nitrogen solubilities in the matrix phase in the presence and in the absence of stress, respectively. It is important to note that the equilibrium solubility of interstitial atoms (N, C, B and H) can be influenced by the magnitude of stress acting on the specimen (see section 1.4.2).

1.6. Outline of the thesis

The effect of the initial microstructure of the unnitrided specimen (cold-rolled or recrystallized) on the low-temperature nitriding response of ternary Fe-4.3 at.% Cr-8.1 at.% Al alloy has been investigated (chapter 2). It has been shown that in the presence of a high fraction of defect density (cold rolled specimens; the high dislocation density), the precipitation of separate, binary, cubic, NaCl-type nitrides of Cr and Al occurs, whereas during nitriding of defect-poor, recrystallized specimens, the development of metastable, ternary, cubic, NaCl-type $Cr_{1-x}Al_xN$ nitride occurs. This suggests that dislocations facilitate the nucleation of binary CrN and AlN nitrides by serving as heterogeneous nucleation sites. Upon nitriding of recrystallized specimen, (i.e., in which mostly homogenous nucleation of nitride precipitates occurs), only mixed $Cr_{1-x}Al_xN$ precipitates have been observed: the incorporation of Al atoms in cubic CrN nitride decreases the misfit-strain energy for the nucleation of the ternary nitride [21]. Thus, the precipitation of ternary nitride is preferred over the formation of binary, cubic CrN nitride or binary, cubic/hexagonal AlN nitride [34, 35] in recrystallized specimens.

The effect of development of tiny, misfitting, coherent precipitates of CrN and VN on the increase of ferrite-matrix lattice parameter has been investigated by nitriding of binary Fe-Cr and Fe-V alloys (chapter 3). The ferrite-matrix lattice parameter changes linearly as a function of volume fraction of nitrides developed in the ferrite matrix. A model explaining the observed change of lattice parameter of the matrix, the second-phase (here nitride precipitate particles) and the assembly (matrix and second-phase) has been presented, which is based on the Eshelby elastic misfit accommodation model originally developed for point-imperfections in solids [39]. Good agreement between the experimental observations and the theoretical results was observed. The distinction of coherent or incoherent diffraction of matrix and precipitates is essential to employ the appropriate model to describe the measured changes in the lattice parameters of the different phases.

During prolonged nitriding/ageing of Fe- 2 at.% Cr and Fe- 4 at.% Cr alloys at higher nitriding temperatures, the type of accommodation of the volume misfit between the nitride precipitates

and the ferrite matrix changes from elastic to plastic in association with coarsening of the nitrides leading to the loss of coherency between precipitates and matrix (see chapter 4). Correspondingly, the diffraction of the assembly consisting of coherent precipitates and matrix changes from coherent diffraction to incoherent (separate) diffraction of relaxed matrix and relaxed coarsened precipitates. The plastic accommodation of misfit is revealed by contraction of initially expanded ferrite matrix. The relaxation of misfit strain is gradual upon Continuous Coarsening (CC) of CrN precipitates, occurring during aging (i.e., prolonged nitriding) of Fe- 2at.% Cr alloy, and is abrupt upon Discontinuous Coarsening (DC) of CrN precipitates [48], occurring during nitriding of Fe- 4.5 at.% Cr alloy.

Misfit induced lattice-parameter changes of matrix and second-phase in crystalline multi-phase systems have been neglected in various diffraction analysis studies in the literature. Ignorance of this effect results in flawed data for the analysis of phase-transformation kinetics. Therefore, chapter 5 presents a review and reevaluation of the effect of misfit strain developing in various two-phase systems. The published experimental lattice-parameter changes of matrix and second-phase obtained by X-ray diffraction methods were gathered and compared with predictions obtained using the model discussed in chapter 3. Diffraction analysis of such lattice-parameter changes requires distinction of the type of diffraction and the type of misfit of matrix and second-phase particles. The diffraction can occur coherently (diffraction by assembly) or can occur incoherently (separate diffraction of matrix and second phase). The type of misfit in different two-phase systems has been classified as (i) specific, intrinsic volume misfit and (ii) cooling induced thermal misfit. By understanding the type (elastic/plastic) of misfit accommodation and the type of diffraction, it is possible to predict the change of lattice parameters in two-phase systems. Good to very good agreements were obtained for predicting the change of lattice parameters in two-phase systems such as nitrided Fe-Cr and Fe-V alloys (coherent CrN/VN precipitates in ferrite matrix) (see chapter 3), Co clusters in Cu-Co alloys [49], aged Fe-N alloys (coarsened incoherent α''-$Fe_{16}N_2$ precipitates in ferrite matrix) [50], aged Al-Si alloys (incoherent Si precipitates in Al matrix) [51] and nitrided/subsequently aged Fe-Cr alloys (coarsened incoherent CrN precipitates in ferrite matrix) (see chapter 4).

Dependence of the nitriding rate of ferrite and austenite substrates on crystallographic orientation of surface grains has been studied for nitrided ferritic Fe- 4.5 at.% Cr and nitrided austenitic Ni- 5at.% Ti alloys (chapter 6). It has been found that the extent of nitriding (surface nitrogen concentration and nitrided depth) is a function of the orientation factor of the surface grains. The orientation factor, defined for cubic crystal structure systems, provides a measure of how large the deviation of the (100) planes of a particular grain from the specimen surface is [41]. This effect has been attributed to the fact that the compressive residual macrostress (see section 1.4.2) developing on the differently oriented surface grains of heterogeneously nitrided specimens is different due to the elastically anisotropic nature of cubic austenitic and ferritic substrates. Due to this, the aforementioned grain-orientation dependent nitriding phenomenon cannot occur for the homogenously nitrided stress-free thin-foil. A simple thermodynamic theory was developed

that relates the rotationally symmetric biaxial planar state of macrostress acting parallel to the surface of the specimens to the solubility of the dissolved nitrogen for the surface grains, depending on their orientation (see section 1.5.2).

References

[1] E.J. Mittemeijer. Fundamentals of Nitriding and Nitrocarburizing. in: Dossett J, Totten GE, (Eds.). ASM Handbook, vol. 4A. Steel Heat Treating Fundamentals and Processes, 2013. pp. 619-646.

[2] K.-M. Winter, J. Kalucki. Gas Nitriding and Gas Nitrocarburizing of Steels. in: Dossett J, Totten GE, (Eds.). ASM Handbook, vol. 4A. Steel Heat Treating Fundamentals and Processes, 2013. pp. 647-675.

[3] E.J. Mittemeijer, M.A.J. Somers. Thermochemical Surface Engineering of Steels Woodhead Publishing, 2015.

[4] D.H. Jack, K.H. Jack. Invited Review - Carbides and Nitrides in Steel, Materials Science and Engineering 11 (1973) 1-27.

[5] B. Mortimer, P. Grieveson, K.H. Jack. Precipitation of Nitrides in Ferritic Iron Alloys Containing Chromium, Scandinavian Journal of Metallurgy 1 (1972) 203-209.

[6] E.J. Mittemeijer, a.B.P. Vogels, P.J. Schaaf. Morphology and lattice distortions of nitrided iron and iron-chromium alloys and steels, Journal of Materials Science 15 (1980) 3129-3140.

[7] R.E. Schacherl, P.C.J. Graat, E.J. Mittemeijer. Gaseous nitriding of iron-chromium alloys, Zeitschrift Fur Metallkunde 93 (2002) 468-477.

[8] M. Sennour, P.H. Jouneau, C. Esnouf. TEM and EBSD investigation of continuous and discontinuous precipitation of CrN in nitrided pure Fe-Cr alloys, Journal of Materials Science 39 (2004) 4521-4531.

[9] G. Miyamoto, A. Yonemoto, Y. Tanaka, T. Furuhara, T. Maki. Microstructure in a plasma-nitrided Fe–18 mass% Cr alloy, Acta Materialia 54 (2006) 4771-4779.

[10] M.H. Biglari, C.M. Brakman, E.J. Mittemeijer. Crystal-Structure and Morphology of AlN Precipitating on Nitriding of an Fe-2 at Percent Al-Alloy, Philosophical Magazine A 72 (1995) 1281-1299.

[11] H.H. Podgurski, H.E. Knechtel. Nitrogenation of Fe-Al Alloys .1. Nucleation and Growth of Aluminum Nitride, Transactions of the Metallurgical Society of AIME 245 (1969) 1595-1602.

[12] W.D. Welch, Carpente.Sh. Investigation of Abnormal Snoek Peak in Iron-Vanadium-Nitrogen System, Acta Metallurgica 21 (1973) 1169-1179.

[13] S.S. Hosmani, R.E. Schacherl, E.J. Mittemeijer. Nitriding behavior of Fe-4wt%V and Fe-2wt%V alloys, Acta Mater 53 (2005) 2069-2079.

[14] D.H. Jack. Structure of Nitrided Iron-Titanium Alloys, Acta Metall Mater 24 (1976) 137-146.

[15] H.H. Podgurski, F.N. Davis. Thermochemistry and nature of nitrogen absorption in nitrogenated Fe-Ti alloys, Acta Metallurgica 29 (1981) 1-9.

[16] G.P. Huffman, H.H. Podgurski. Mossbauer Study of Nitrided Fe-Mo and Fe-Ti Alloys, Acta Metallurgica 23 (1975) 1367-1379.

[17] S.R. Meka, K.S. Jung, E. Bischoff, E.J. Mittemeijer. Unusual precipitation of amorphous silicon nitride upon nitriding Fe-2at.%Si alloy, Philos Mag 92 (2012) 1435-1455.

[18] S.R. Meka, E. Bischoff, B. Rheingans, E.J. Mittemeijer. Octapod-shaped, nanosized, amorphous precipitates in a crystalline ferrite matrix, Philosophical Magazine Letters 93 (2013) 238-245.

[19] H.P. Van Landeghem, M. Gouné, S. Bordère, F. Danoix, A. Redjaïmia. Competitive precipitation of amorphous and crystalline silicon nitride in ferrite: Interaction between structure, morphology, and stress relaxation, Acta Materialia 93 (2015) 218-234.

[20] A.R. Clauss, E. Bischoff, R.E. Schacherl, E.J. Mittemeijer. Phase transformation of mixed Cr1-xAlxN nitride precipitates in ferrite, Philosophical Magazine 89 (2009) 565-582.

[21] A.R. Clauss, E. Bischoff, R.E. Schacherl, E.J. Mittemeijer. The microstructure of the diffusion zone of a gaseously nitrided Fe-1.5 wt-% Cr-1.5 wt-%Al alloy, Materials Science and Technology 26 (2010) 297-308.

[22] K.S. Jung, R.E. Schacherl, E. Bischoff, E.J. Mittemeijer. The kinetics of the nitriding of ternary Fe-2 at pct Cr-2 at pct Ti alloy, Metallurgical and Materials Transactions A: Physical Metallurgy and Materials Science 43 (2012) 763-773.

[23] K.S. Jung, S.R. Meka, R.E. Schacherl, E. Bischoff, E.J. Mittemeijer. Nitride formation and excess nitrogen uptake after nitriding ferritic Fe-Ti-Cr alloys, Metallurgical and Materials Transactions A: Physical Metallurgy and Materials Science 43 (2012) 934-944.

[24] M. Udyavar, D.J. Young. Precipitate morphologies and growth kinetics in the internal carburisation and nitridation of Fe-Ni-Cr alloys, Corrosion Science 42 (2000) 861-883.

[25] A.M. Maliska, J.A. de Cezaro, J.G. Justino, A.N. Klein. Microstructural and mechanical characterization of plasma nitriding Fe-Mo-Cu P/M steels with different alloy contents. Advances in Powder Metallurgy and Particulate Materials, vol. 2, 1997. p.13-169.

[26] T. Steiner, S.R. Meka, B. Rheingans, E. Bischoff, T. Waldenmaier, G. Yeli, T.L. Martin, P.A.J. Bagot, M.P. Moody, E.J. Mittemeijer. Microstructural development of Fe-1 at.%Cr-1 at.%Mo alloy upon nitriding; crystal structure and composition of ternary nitrides , to be submitted (2015).

[27] T. Steiner, S.R. Meka, E. Bischoff, T. Waldenmaier, E.J. Mittemeijer. Nitriding of ternary Fe-Cr-Mo alloys; role of the Cr/Mo-ratio , to be submitted (2015).

[28] H. Atmani, O. Thoumire. Microstructure characterization of fluidized bed nitrided Fe-Si and Fe-Si-Al foils, Bulletin of Materials Science 25 (2002) 219-225.

[29] W. Roberts, P. Grieveson, K.H. Jack. Precipitation of Silicon Nitrides and Manganese-silicon nitrides in steel, J Iron Steel Inst (London) 210 (1972) 931-937.

[30] B. Schwarz, S.R. Meka, R.E. Schacherl, E. Bischoff, E.J. Mittemeijer. Nitriding of iron-based ternary Fe-V-Si alloy: The precipitation process of separate nitrides, Acta Materialia 76 (2014) 394-403.

[31] B. Schwarz, P.J. Rossi, L. Straßberger, F. Jörg, S.R. Meka, E. Bischoff, R.E. Schacherl, E.J. Mittemeijer. Coherency strain and precipitation kinetics: crystalline and amorphous nitride formation in ternary Fe-Ti/Cr/V-Si alloys, Philosophical Magazine 94 (2014) 3098- 3119.

[32] K.S. Jung, S.R. Meka, R.E. Schacherl, E. Bischoff, E.J. Mittemeijer. Nitride Formation and Excess Nitrogen Uptake After Nitriding Ferritic Fe-Ti-Cr Alloys, Metallurgical and Materials Transactions A 43A (2012) 934-944.

[33] A.R. Clauss, E. Bischoff, S.S. Hosmani, R.E. Schacherl, E.J. Mittemeijer. Crystal Structure and Morphology of Mixed Cr(1-x) Al (x) N Nitride Precipitates: Gaseous Nitriding of a Fe-1.5 Wt Pct Cr-1.5 Wt Pct Al Alloy, Metallurgical and Materials Transactions A 40A (2009) 1923-1934.

[34] M.H. Biglari, C.M. Brakman, E.J. Mittemeijer, S. Vanderzwaag. The Kinetics of the Internal Nitriding of Fe-2 at Pct Al-Alloy, Metallurgical and Materials Transactions A 26 (1995) 765-776.

[35] M.H. Biglari, C.M. Brakman, E.J. Mittemeijer. Crystal-Structure and Morphology of Aln Precipitating on Nitriding of an Fe-2 at Percent Al-Alloy, Philos Mag A 72 (1995) 1281-1299.

[36] H. Selg, E. Bischoff, S.R. Meka, R.E. Schacherl, T. Waldenmaier, E.J. Mittemeijer. Molybdenum-Nitride Precipitation in Recrystallized and Cold-Rolled Fe-1 at. pct Mo Alloy, Metallurgical and Materials Transactions A 44A (2013) 4059-4070.

[37] M.A.J. Somers, R.M. Lankreijer, E.J. Mittemeijer. Excess Nitrogen in the Ferrite Matrix of Nitrided Binary Iron-Based Alloys, Philosophical Magazine A 59 (1989) 353-378.

[38] N.E. Vives Diaz, R.E. Schacherl, L.F. Zagonel, E.J. Mittemeijer. Influence of the microstructure on the residual stresses of nitrided iron-chromium alloys, Acta Materialia 56 (2008) 1196-1208.

[39] J.D. Eshelby. Distortion of a Crystal by Point Imperfections, Journal of Applied Physics 25 (1954) 255-261.

[40] J.W. Christian. The Theory of Transformations in Metals and Alloys, Second Edition (2002) p. 200-208.

[41] I.C. Noyan, J.B. Cohen. Residual Stress measurement by Diffraction and Interpretation, Springer-Verlag, New York, 1987.

[42] D.R. Gaskell. Introduction to the Thermodynamics of Materials. Fifth ed., Taylor & Francis, New York, 2003.

[43] E.J. Mittemeijer, J.T. Slycke. Chemical Potentials and Activities of Nitrogen and Carbon Imposed by Gaseous Nitriding and Carburising Atmospheres, Surface Engineering 12 (1996) 152-162.

[44] J. Stein, R.E. Schacherl, M.S. Jung, S. Meka, B. Rheingans, E.J. Mittemeijer. Solubility of nitrogen in ferrite; the Fe-N phase diagram, International Journal of Materials Research 104 (2013) 1053-1065.

[45] E.J. Mittemeijer, M.A.J. Somers. Thermodynamics, Kinetics, and Process Control of Nitriding, Surface Engineering 13 (1997) 483-497.

[46] J.C.M. Li, R.A. Oriani, L.S. Darken. Thermodynamics of Stressed Solids, Z Phys Chem Neue Fol 49 (1966) 271- 290.

[47] H.A. Wriedt, R.A. Oriani. Effect of tensile and compressive elastic stress on equilibrium hydrogen solubility in a solid, Acta Metallurgica 18 (1970) 753-760.

[48] P.M. Hekker, H.C.F. Rozendaal, E.J. Mittemeijer. Excess nitrogen and discontinuous precipitation in nitrided iron-chromium alloys, Journal of Materials Science 20 (1985) 718-729.

[49] C. Michaelsen. On the Structure and Homogeneity of Solid-Solutions - the Limits of Conventional X-Ray-Diffraction, Philos Mag A 72 (1995) 813-828.

[50] E.J. Mittemeijer, A. van Gent. Unusual Lattice-Parameters in Two-Phase Systems - the Case of Aged Nitrogen-Ferrite, Scripta Metall Mater 18 (1984) 825-828.

[51] E.J. Mittemeijer, P. van Mourik, T.H. de Keijser. Unusual Lattice-Parameters in Two-Phase Systems after Annealing, Philos Mag A 43 (1981) 1157-1164.

Chapter 2

Low temperature nitriding of ferritic Fe-Cr-Al alloys

Maryam Akhlaghi, Sai Ramudu Meka, Ewald Bischoff, Eric Jan Mittemeijer

Abstract

The effect of the initial microstructure (recrystallized or cold-rolled) on the nitride-precipitation process upon gaseous nitriding of ternary, ferritic, Fe-Cr-Al alloy was investigated at 450°C. In the recrystallized specimens, precipitation of metastable ternary, cubic, NaCl-type mixed $Cr_{1-x}Al_xN$ took place, whereas in the cold-rolled specimens precipitation of firstly binary cubic NaCl-type CrN and secondly binary cubic NaCl-type AlN occurs. The difference in nitriding response for the different initial microstructures could be ascribed to the potential preference for nucleation of CrN precipitates on dislocations.

2.1. Introduction

Gaseous nitriding is one of the most widely employed thermochemical surface treatments to improve the mechanical (wear and fatigue) and chemical (corrosion) properties of ferritic steel components. Gaseous nitriding is carried out in a NH_3/H_2 gas mixture. The atomic nitrogen from dissociating NH_3 at the surface gets incorporated into the surface of the specimen [1, 2]. The inwardly diffusing nitrogen reacts with alloying elements in steel having affinity for nitrogen (as Cr and Al) and forms alloying element nitrides. Understanding the collective interaction of multiple alloying elements with nitrogen is important for understanding the nitriding behavior of steels [3, 4].

The nitriding response of binary Fe-based alloys has been investigated extensively; (Fe-Cr [5, 6] [7]), Fe-Al [8], Fe-V [9], Fe- Ti [10] and Fe-Si [11]. Only a few works have been devoted to a fundamental investigation of the nitride-precipitation process taking place in ternary iron-based alloys. It was shown that, in contrast with the development of stable binary nitrides, metastable ternary, "mixed" nitrides could develop [12, 13]: cubic NaCl-type $Cr_{1-x}Al_xN$ and $Cr_{1-x}Ti_xN$ in Fe-Cr-Al and Fe-Cr-Ti alloys, respectively.

It is not generally recognized that characteristics of the unnitrided microstructure can decisively influence the nitride-precipitation process. Thus, investigations on recrystallized and cold-rolled specimens of binary Fe-Al [14] and Fe-Mo [15] alloys have revealed that the crystal-lattice defects in cold-rolled specimens can lead to different nitride modifications and enhance the precipitation kinetics.

Against the above background, the present project aims to investigate the role of defects on the nitriding behaviour of iron-based ternary Fe-Cr-Al alloys. To this end nitriding experiments were performed on both cold-rolled and recrystallized specimens of Fe-4.3at.%Cr-8.1at.%Al alloy. Low temperature nitriding at 450°C was carried out in order to minimize the possible occurrence of recrystallization of the cold-rolled specimens during nitriding.

2.2. Experimental

2.2.1. Specimen preparation and nitriding

Melts of Fe-4.3at.%Cr-8.1at.%Al alloy were prepared by melting appropriate amounts of pure Fe (99.98 wt.%), pure Cr (99.999 wt.%) and pure Al (99.999 wt.%) in an Al_2O_3 crucible under a protective argon gas (99.999 vol.%) atmosphere. Subsequently, the melt was cast in a cylindrical (diameter of 10 mm and a length of 100 mm) copper mould. The results of chemical analysis of the produced cast alloy are presented in Table **2-1**. The cast rods were cold-rolled to sheets of 1 mm thickness. From these sheets specimens were cut with lateral dimensions of 1x1.5cm2. After grinding and polishing (finishing with 1 μm diamond suspension) of the specimen surface, some of the

specimens were directly nitrided in their deformed state. The other specimens were, before nitriding, annealed at 850°C for 2 h under H2 atmosphere to obtain a recrystallized grain structure.

Table 2-1. Chemical analysis of Fe-Cr-Al alloy cast. Metal contents were determined by inductively coupled plasma – optical emission spectroscopy; the contents of light element impurities were determined by carrier gas hot extraction (O, N) and a combustion method (C).

Element	Cr		Al		O	N	C
	wt.%	at%	wt.%	at%	wt.%	wt.%	wt.%
Content	4.17 ± 0.05	4.28 ± 0.05	4.12 ± 0.05	8.14 ± 0.10	0.006 ± 0.002	<0.001	0.002

The specimens to be nitrided were suspended with a quartz fiber in a vertical quartz tube furnace where nitriding occurred in an ammonia/hydrogen gas flux (purity: H_2: 99.999 vol. %; NH_3: > 99.998 vol. %). The fluxes of both gases (45 ml/min NH_3 and 455 ml/min H_2) were adjusted with mass flow controllers to achieve a nitriding potential of $r_N = 0.104\ atm^{-1/2}$. Nitriding experiments were performed at 450°C for 72 h and 144 h. The employed nitriding potential is below the critical nitriding potential necessary for (γ´) iron-nitride formation upon nitriding pure iron at 450°C [1].

2.2.2. Microstructural characterization

For metallographic investigation of the nitrided zone, a piece of the nitrided specimen was cut from the specimen/foil, normal to the specimen/foil surface, and embedded in Struers PolyFast. The cross-sections were then ground and polished (final polishing using 1µm diamond suspension). The specimens were etched with 4% Nital for about 15 s at room temperature. For light microscopy a Zeiss Axiophot microscope equipped with a digital camera (Olympus ColorView IIIu) was used.

Hardness-depth profiles across the nitrided zone were measured using a Vickers Microhardness tester (Leica VMHT Mot) applying a load of 10 g and a dwell time of 10 s.

To determine the elemental concentrations (Al, Cr, N and Fe) of the nitrided zone, electron probe microanalysis (EPMA) was performed on the cross-section of nitrided specimens. For these measurements, a Cameca SX100 microprobe (acceleration voltage U = 10 kV, current I = 100 nA, spot size about 1 µm) was used. To obtain the element contents at each measurement point, the intensities of the characteristic X-ray emission peaks were measured and divided by the corresponding intensities obtained from standard samples of pure Fe, Cr, Al and γ´-Fe_4N (for N). Elemental concentrations were calculated from the intensity ratios applying the Φ(ρz) approach [16].

For phase analysis X-ray diffractograms were recorded (in a diffraction-angle (2θ) range of 30°-105°, applying a step size of 0.02° in 2θ with a counting time of 300 s per step) from the surface of specimens before and after nitriding using a PanAlytical X'Pert diffractometer with Bragg-Brentano

configuration, applying Co-Kα radiation and a graphite monochromator in the diffracted beam. During the measurements the specimens were rotated around their surface normal to improve the crystallite statistics. In order to identify the different phases from the peaks in the diffraction pattern the ICDD data base was used [17].

Electron transparent foils for TEM investigations were prepared from material taken at 60 µm from the surface for both cold-rolled and recrystallized specimens nitrided for 144 h at 450 °C. To this end self-supporting discs (Ø 3 mm) were stamped with a mechanical punch from sheets produced by removing material mechanically from both surfaces of the nitrided specimens. These discs were ground, dimpled and subsequently, Ar-ion milled (4 kV, 5 mA, angle of ion incidence: 8 °, time: 4.5 h; liquid nitrogen cooling stage). TEM analysis was performed using a Philips CM 200 transmission electron microscope operating at 200 kV. Bright field (BF) and dark field (DF) images and corresponding selected area diffraction patterns (SADPs) were recorded using a CCD camera from Gatan.

2.3. Results

2.3.1. Morphology of nitrided region

Light optical macrographs recorded from the cross-sections of recrystallized and cold-rolled specimens nitrided for 72 h and 144 h are shown in Figure **2-1** evidently the diffusion zone of the cold-rolled specimens is more strongly etched than that of the recrystallized specimens where only the grain boundaries in the nitrided zone are strongly etched. Upon prolonged nitriding of the cold-rolled specimen, two distinctly and differently etched regions can be distinguished within the nitrided zone: a surface adjacent, strongly etched zone (marked as region 1 in Figure **2-1**(d)) followed by a less strongly etched region (marked as region 2 in Figure **2-1**(d)), whereas no such distinction in etching response is observed for the recrystallized specimen (see Figure **2-1**(c)). This occurrence of two differently etched zones in the nitrided region of the cold-rolled specimens is attributed to different nitride-precipitation processes (see section .23.2).

X-ray diffraction patterns recorded from the surface of nitrided recrystallized and cold-rolled specimens reveal a nitriding induced extreme broadening of the ferrite-matrix peaks (see Figure **2-2**); no reflections of alloying element nitrides could be detected. The pronounced ferrite-peak broadening is attributed to the microstrains introduced into the ferrite matrix by the development of misfitting (semi-coherent) nitride precipitates. In addition to this peak broadening, distinct peak shift occurs as well to lower diffraction angles (see result for 72 h in Figure **2-2**). This effect is a direct consequence of the matrix dilatation caused upon elastic accommodation of the precipitates/matrix misfit [18] and/or the development of residual compressive macrostress parallel to the surface in the surface adjacent, nitrided region. Upon prolonged nitriding, the relaxation of misfit strains results in a backshift of the ferrite peaks towards the location expected for unstrained ferrite.

TEM BF and DF images and the corresponding SADPs of foils of the recrystallized and cold-rolled specimens (taken at 60 µm from the surface) are shown in Figure **2-3**. Nanosized alloying-element nitride platelets have developed along {100} habit planes of the ferrite matrix. In the SADPs, in addition to intense diffraction spots of the ferrite matrix, less intense diffraction spots are present which can be indexed according to cubic NaCl-type structured precipitates having a lattice parameter close to 21/2 times the lattice parameter of ferrite. Further the locations of the diffraction spots of these precipitates with respect to the ferrite-matrix spots are according to a Baker-Nutting orientation relationship (OR) between precipitates and matrix. The lattice parameters of cubic NaCl-type CrN (4.14 Å) and AlN (4.04 Å) [ICDD 2002] are close to each other and both nitrides are known to maintain a Baker-Nutting OR with the matrix.

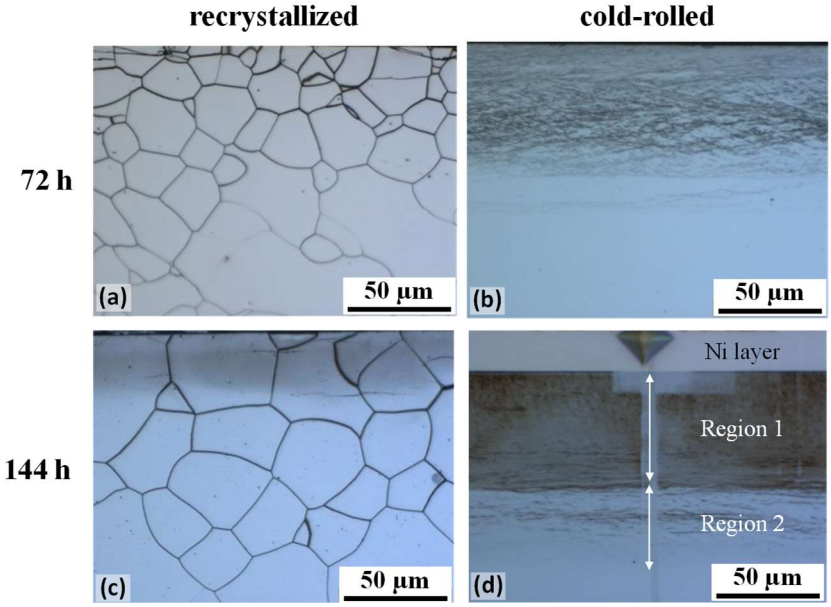

Figure 2-1. Light optical micrographs of recrystallized and cold-rolled specimens. Carbon contamination trace of EPMA scan can be seen in image d (below the arrows).

Therefore, it is difficult to identify these nitrides separately from the diffraction spots in the measured SADPs. Further noticing the apparent absence of hexagonal wurtzite-type AlN in both cold-rolled and recrystallized specimens, it is suggested that the developed precipitates are either both cubic NaCl-type CrN and AlN or a ternary, metastable "mixed", cubic, NaCl-type $Cr_{1-x}Al_xN$ [13, 19].

2.3.2. Simultaneous vs. successive precipitation of nitrides

Hardness-depth profiles measured on the cross-sections of the recrystallized and the cold-rolled specimens nitrided for different times are shown in Figure **2-4**. After nitriding for 72 h, a gradual decrease of hardness as a function of depth occurred for the recrystallized specimen, whereas a much stronger case/core transition is apparent for the corresponding, cold-rolled specimen (cf. Figure **2-4** (a) and (b)).

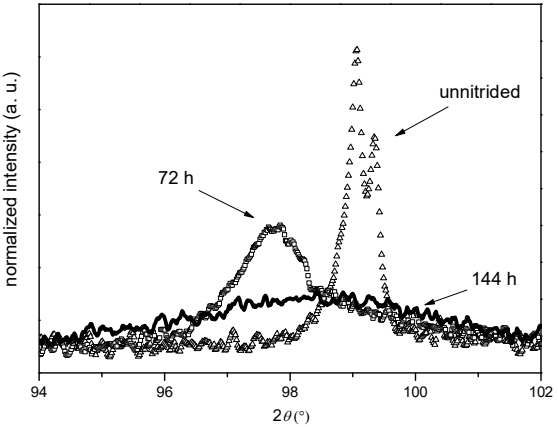

Figure 2-2. X-ray diffractograms (Co-Kα radiation), around the location of the 211 ferrite-matrix reflection, recorded from the surface of the recrystallized specimens before and after nitriding.

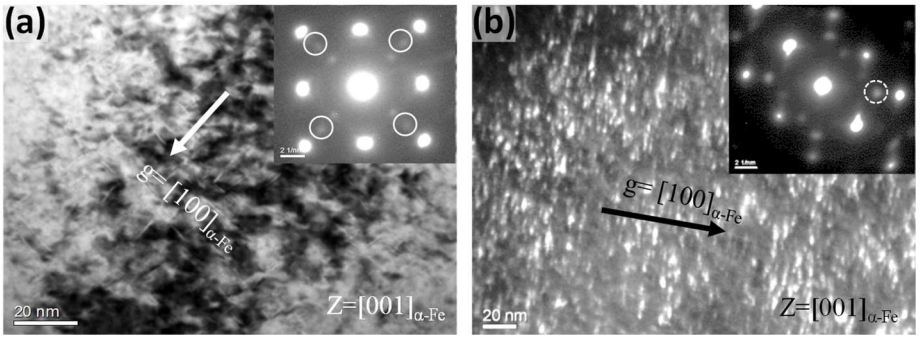

Figure 2-3. (a) BF image and corresponding SADP (zone axis [001]α-Fe) obtained from the recrystallized specimen nitrided for 144 h (b) DF image obtained using 002 spot of Me-nitride (shown with dashed circle in the corresponding [001]α-Fe zone axis SADP) from the cold-rolled specimen nitrided for 144 h. The extra diffraction spots in both SADPs, indicated with white circles in the SADP of (a) (as inset), correspond to the 002 -type spots of rock-salt structure type nitride precipitates with Baker-Nutting OR with the ferrite matrix.

Upon prolonged nitriding (144 h), a significant further increase of the hardness in the surface region occurred; 1100 HV and 1700 HV after 72h of nitriding for recrystallized and cold-rolled specimens, respectively; about 2100 HV after 144h of nitriding for both cold-rolled and recrystallized specimens. After prolonged nitriding (144 h) of the cold-rolled specimens two nitrided regions occur in the nitrided zone according to the hardness-depth profiles: a zone of high constant hardness adjacent to the surface, followed by a region of much lesser hardness exhibiting a gradual decrease of hardness with depth (see Figure **2-4**(b); regions marked as region 1 and region 2). A similar phenomenon does not occur for the long time (144 h) nitrided recrystallized specimen (see Figure **2-4**(a)). These observations are compatible with the differently etched nitrided regions observed in LM images of the recrystallized and cold-rolled specimens (cf. Figure **2-1**(c) and (d)).

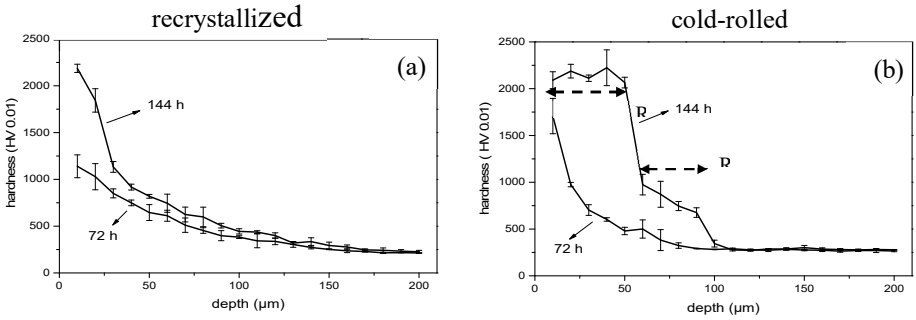

Figure 2-4. Hardness-depth profiles measured on cross-section of nitrided recrystallized and cold-rolled specimens.

The nitrogen concentration-depth profiles, as measured by EPMA (cf. section .22.2) on the cross-sections of the recrystallized and cold-rolled specimens nitrided for 144 h, are shown in

Figure **2-5**. In the case of both the cold-rolled and the recrystallized specimens, the surface nitrogen content is above that expected for the precipitation of all alloying element as stoichiometric nitride (either as separate, binary nitrides AlN and CrN or as the ternary, mixed nitride $Cr_{1-x}Al_xN$) and the saturation of ferrite matrix with dissolved nitrogen. The additional nitrogen uptake above the expected level (indicated with double arrow in

Figure **2-5**(a)) is called “excess nitrogen” (for details about excess nitrogen, see [20]). In the deeper region of the nitrided zone of the recrystallized specimen, relatively large N contents occur at the grain boundaries. This observation, together with the TEM evidence provided in Figure **2-6**, indicates the development of cubic rock-salt type nitride precipitates preferably at grain boundaries.

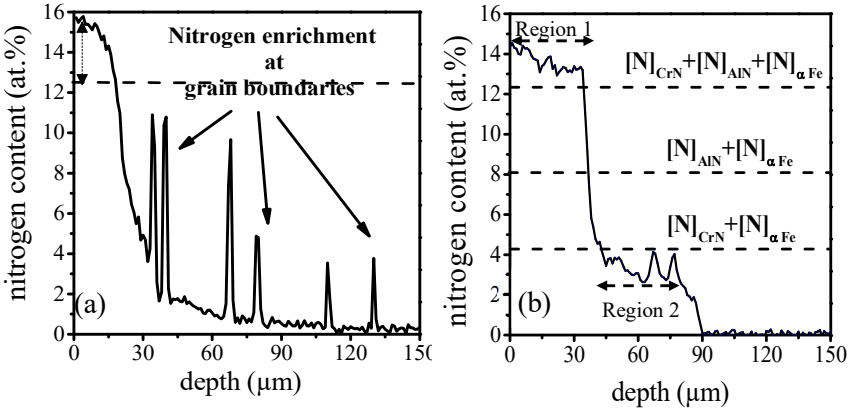

Figure 2-5. Nitrogen concentration-depth profiles (EPMA) for a) recrystallized and b) cold-rolled specimens nitrided for 144 h. Dashed horizontal lines represent the nitrogen levels expected for different possible scenarios of nitride development. The nitrogen taken up above the dashed line of highest level (indicated with double arrow in (a)) is called excess nitrogen.

As compared to the recrystallized specimen, a clear plateau region in the surface adjacent area occurs for the nitrogen-depth profile of the cold-rolled nitrided specimen (see

Figure **2-5**(b)). This parallels a similar feature observed in the measured hardness-depth profile of the same specimen (region 1 in Figure **2-4**(b)), and is compatible with region 1 in the LM image of Figure **2-1**(d). The near surface plateau corresponds with a nitrogen content in any case compatible with the precipitation of all alloying element as nitride (CrN + AlN or mixed $Cr_{1-x}Al_xN$) (see above for uptake of excess nitrogen). The nitrogen level of the second plateau at larger depths corresponds with a nitrogen content which is about the expected nitrogen content when only all Cr has precipitated as CrN.

2.4. Discussion

In the present Fe-Cr-Al alloy, in both cold-rolled and recrystallized specimens, upon nitriding cubic NaCl-type nitride platelets develop satisfying a Baker-Nutting OR with the ferrite matrix. The saturation levels of nitrogen taken up by both the cold-rolled and the recrystallized specimens suggest the precipitation of all Cr and all Al as nitrides of a stoichiometry given by MeN.

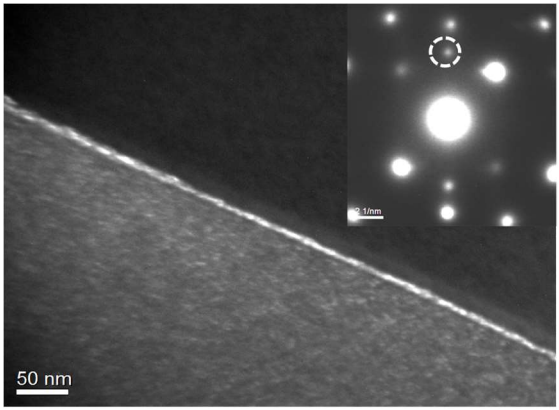

Figure 2-6. DF image and corresponding SADP recorded from the grain boundary area of a recrystallized specimen nitrided for 144 h. The dark field image has been obtained using the 002 spot of cubic NaCl-type MeN nitride (shown in white circle). The grain boundary appears bright indicating the presence of MeN.

The absence of the stable hexagonal wurtzite-type modification of AlN even in the nitrided recrystallized Fe-Cr-Al alloy is attributed to the easier nucleation of cubic rock-salt type, mixed ternary $Cr_{1-x}Al_xN$ as compared to the difficult nucleation of, in particular, the stable binary hexagonal AlN: incorporation of Al into CrN decreases the misfit-strain energy more than that the formation of metastable mixed-nitride increases the chemical Gibbs energy [13].

In the cold-rolled specimen, a clear plateau in nitrogen content adjacent to the unnitrided case (region 2 in

Figure **2-5**(b)) suggests by its level the development of separate binary CrN in the early stages of nitriding. The absence of such a plateau for the recrystallized specimen (

Figure **2-5**(a)) suggests that the defects (dislocations) may be the agents inducing this nitride precipitation of the binary CrN nitride in the cold-rolled specimens. The following explanation is offered for this phenomenon.

Thermodynamic calculations for the homogeneous precipitation of cubic NaCl-type CrN in the ferrite matrix and for the heterogeneous nucleation of cubic NaCl-type CrN on dislocations of the ferrite matrix were carried out, analogous to those performed in [14] for AlN precipitation (Figure **2-7**). It follows that no nucleation barrier exists for the precipitation of cubic NaCl-type CrN on dislocations (Figure **2-7**(b)). As a consequence, direct precipitation of CrN on the present dislocations is possible. As follows from the results, shown in Figure **2-7**(b), a similar remark can also be made for the precipitation on dislocations, without nucleation barrier, for cubic NaCl-type AlN. However, as also follows from a comparison of the ΔG curves for CrN and AlN in Figure **2-7**(b), the larger gain in energy per mole N is obtained if CrN precipitation occurs.

This reflects the metastable nature of cubic AlN as compared to the stable nature of hexagonal AlN. Hence, precipitation of (the thermodynamically stable cubic, NaCl type) CrN on dislocations is favoured over the precipitation of AlN on dislocations. Thus, the nitride precipitation in the cold-rolled specimen starts with precipitation of all Cr as CrN leading to "region 2" in Figure **2-4**(b) and

Figure **2-5**(b). Only after all Cr has precipitated as nitride, the solubility of nitrogen in the ferrite matrix increases and the developing supersaturation will lead to separate precipitation of cubic rock-salt type AlN on unoccupied dislocation lines.

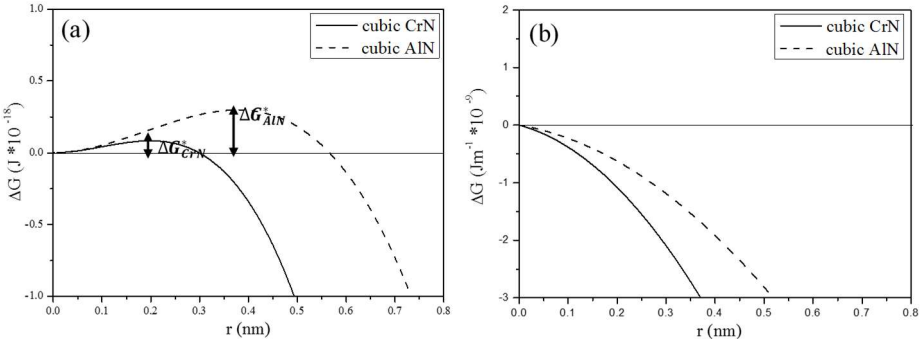

Figure 2-7. The total Gibbs energy as a function of nitride-particle radius for a) homogenous precipitation of spherical coherent cubic AlN and CrN particles in the recrystallized specimen at 500°C, ΔG per particle. ΔG* is activation energy for thermally activated nucleation of CrN and AlN nuclei. b) heterogeneous precipitation of cylindrical coherent cubic AlN and CrN precipitate on dislocations in the cold-rolled specimen at 500°C, ΔG per particle and per unit length of dislocation.

2.5. Conclusions

Upon low temperature nitriding of cold-rolled Fe-4.3at.%Cr-8.1at.%Al specimens, the nitride-precipitation process sets in with the precipitation of binary CrN nitride, whereas metastable, mixed ternary $Cr_{1-x}Al_xN$ nitride develops in recrystallized specimens.

The difference in nitriding response of the cold-rolled and the recrystallized specimens can be ascribed to the huge dislocation density in the cold-rolled specimens: these dislocations act as favorable sites for the nucleation of CrN without nucleation-energy barrier. A similar precipitation of cubic NaCl-type AlN on dislocation is less favored as a consequence of the metastable nature of this AlN modification.

In the absence of dislocations, in the recrystallized specimens, the incorporation of Al in cubic CrN leading to the mixed cubic $Cr_{1-x}Al_xN$ modification is favoured over separate precipitation of cubic CrN and hexagonal AlN, as this reduces the misfit energy considerably.

References

[1] E.J. Mittemeijer, M.A.J. Somers. Thermodynamics, Kinetics, and Process Control of Nitriding, Surface Engineering 13 (1997) 483-497.

[2] E.J. Mittemeijer. Fundamentals of Nitriding and Nitrocarburizing. in: Dossett J, Totten GE, (Eds.). ASM Handbook, vol. 4A. Steel Heat Treating Fundamentals and Processes, 2013. pp. 619-646.

[3] B. Mortimer, P. Grieveson, K.H. Jack. Precipitation of Nitrides in Ferritic Iron Alloys Containing Chromium, Scandinavian Journal of Metallurgy 1 (1972) 203-209.

[4] E.J. Mittemeijer. Nitriding Response of Chromium-Alloyed Steels, Jom-Us 37 (1985) 16-20.

[5] R.E. Schacherl, P.C.J. Graat, E.J. Mittemeijer. Gaseous nitriding of iron-chromium alloys, Zeitschrift Fur Metallkunde 93 (2002) 468-477.

[6] M. Sennour, P.H. Jouneau, C. Esnouf. TEM and EBSD investigation of continuous and discontinuous precipitation of CrN in nitrided pure Fe-Cr alloys, Journal of Materials Science 39 (2004) 4521-4531.

[7] G. Miyamoto, A. Yonemoto, Y. Tanaka, T. Furuhara, T. Maki. Microstructure in a plasma-nitrided Fe-18 mass% Cr alloy, Acta Mater 54 (2006) 4771-4779.

[8] M.H. Biglari, C.M. Brakman, E.J. Mittemeijer. Crystal-Structure and Morphology of AlN Precipitating on Nitriding of an Fe-2 at Percent Al-Alloy, Philosophical Magazine A 72 (1995) 1281-1299.

[9] S.S. Hosmani, R.E. Schacherl, E.J. Mittemeijer. Nitriding behavior of Fe-4wt%V and Fe-2wt%V alloys, Acta Mater 53 (2005) 2069-2079.

[10] D.H. Jack. Structure of Nitrided Iron-Titanium Alloys, Acta Metall Mater 24 (1976) 137-146.

[11] S.R. Meka, K.S. Jung, E. Bischoff, E.J. Mittemeijer. Unusual precipitation of amorphous silicon nitride upon nitriding Fe-2at.%Si alloy, Philos Mag 92 (2012) 1435-1455.

[12] K.S. Jung, S.R. Meka, R.E. Schacherl, E. Bischoff, E.J. Mittemeijer. Nitride Formation and Excess Nitrogen Uptake After Nitriding Ferritic Fe-Ti-Cr Alloys, Metallurgical and Materials Transactions A 43A (2012) 934-944.

[13] A.R. Clauss, E. Bischoff, S.S. Hosmani, R.E. Schacherl, E.J. Mittemeijer. Crystal Structure and Morphology of Mixed Cr(1-x) Al (x) N Nitride Precipitates: Gaseous Nitriding of a Fe-1.5 Wt Pct Cr-1.5 Wt Pct Al Alloy, Metallurgical and Materials Transactions A 40A (2009) 1923-1934.

[14] M.H. Biglari, C.M. Brakman, E.J. Mittemeijer, S. Vanderzwaag. The Kinetics of the Internal Nitriding of Fe-2 at Pct Al-Alloy, Metallurgical and Materials Transactions A 26 (1995) 765-776.

[15] H. Selg, E. Bischoff, S.R. Meka, R.E. Schacherl, T. Waldenmaier, E.J. Mittemeijer. Molybdenum-Nitride Precipitation in Recrystallized and Cold-Rolled Fe-1 at. pct Mo Alloy, Metallurgical and Materials Transactions A 44A (2013) 4059-4070.

[16] J.L. Pouchou, F. Pichoir. A New Model for Quantitative X-Ray-Microanalysis .2. Application to in-Depth Analysis of Heterogeneous Samples, Recherche Aerospatiale (1984) 349-367.

[17] I.J.-I.C.f.D. Data. PCPDFWIN, 2002.

[18] E.J. Mittemeijer, P. Vanmourik, T.H. Dekeijser. Unusual Lattice-Parameters in 2-Phase Systems after Annealing, Philosophical Magazine A 43 (1981) 1157-1164.

[19] K.S. Jung, R.E. Schacherl, E. Bischoff, E.J. Mittemeijer. Normal and excess nitrogen uptake by iron-based Fe-Cr-Al alloys: the role of the Cr/Al atomic ratio, Philos Mag 91 (2011) 2382-2403.

[20] M.A.J. Somers, R.M. Lankreijer, E.J. Mittemeijer. Excess Nitrogen in the Ferrite Matrix of Nitrided Binary Iron-Based Alloys, Philosophical Magazine A 59 (1989) 353-378.

Chapter 3

Lattice-parameter change induced by accommodation of precipitate/matrix misfit; misfitting nitrides in ferrite

M. Akhlaghi, T. Steiner, S.R. Meka, A. Leineweber and E.J. Mittemeijer

Abstract

Upon nitriding of iron-based alloys, development of misfitting coherent nitride precipitates in a ferrite matrix induces an overall expansion of the ferrite lattice. This lattice expansion was quantitatively determined by X-ray diffraction from the change of the lattice parameter of ferrite of homogenously nitrided Fe-Cr and Fe-V alloys. Adopting the experimentally verified (by X-ray diffraction and transmission electron microscopy) notion that the misfitting precipitates *diffract coherently with the matrix*, the extent of this hydrostatic lattice-strain component could be calculated, in general, as function of the precipitate/matrix misfit, the volume fraction of precipitates and the elastic properties of the matrix and precipitates. The experimentally observed and the predicted dependencies of lattice dilatation agree very well for both nitrided Fe-Cr and Fe-V alloys. This is the first time that this type of lattice expansion was experimentally identified and quantitatively explained.

3.1. Introduction

Solid-state phase transformations involving volume misfit between parent and product phases can induce unusual, non-equilibrium phenomena, such as, the establishment of metastable phases (e.g. cubic AlN in a ferrite matrix [1, 2]), non-monotonous variation of transformation rate (e.g. during austenite-ferrite and austenite-martensite transformations [3-5]), unusual morphologies (as octapod shaped, amorphous silicon-nitride particles in a ferrite matrix [6]). These effects are often attributed to the complex interplay of the chemical Gibbs energy change driving the transformation and the deformation energy associated with volume misfit accommodation [7, 8]. Precise understanding of the effects of misfit-strain energies on the thermodynamics and kinetics of phase transformations and on the resulting microstructure is essential to optimize the properties of engineering components [9].

The elastic strain fields surrounding individual (tiny) precipitates have been exposed by transmission electron microscope (TEM) diffraction-contrast images [10-12] which allow (local) determination of the sign and (approximate) magnitude of the occurring misfit. The lattice distortions associated with misfit-strain fields induce diffuse scattering in X-ray diffraction (XRD) experiments [13], which can be used to reveal characteristics of the strain fields around (very) small precipitates [14]. The presence of misfitting inclusions of larger dimensions induces (X-ray) diffraction-line broadening, characteristic for the presence of *micro*strains [13, 15, 16]. However, it is not generally recognized that the (average, overall) lattice-parameter values of misfitting systems are different from their (misfit) strain-free values, thereby exposing the presence of a (hydrostatic) *macro*strain. Thus, straightforward determination of the lattice parameter (e.g. from the peak position in (X-ray) diffractograms) provides important information not only on the course of a precipitation process by compositional change of the parent matrix, but also on the extent of the developing misfit-strain fields. The last feature plays a cardinal role in the present work.

The state of stress invoked by misfitting inclusions in a matrix has been dealt with largely theoretically in the literature [17-20]. Experimental verification of such theoretical predictions is relatively rare: adopting a theory for point imperfections in a solid matrix, the effect of misfitting precipitates on the lattice distortions of the matrix, and in one case also of the precipitates, was investigated for the case of *incoherent* precipitate/matrix interfaces [21-23]. Since this early work, no further development and application of this approach appears to have taken place.

Against the above background, the present work is devoted to prediction and experimental verification of lattice distortions introduced upon the development of misfitting second-phase particles in a solid matrix, with (largely) *coherent* precipitate/matrix interfaces, employing X-ray diffraction. To this end, systems composed of misfitting nitride particles in a ferrite matrix, as developing during internal nitridation of iron-based alloy substrates (Fe-Cr and Fe-V alloys), have been chosen as model systems. The tiny CrN and VN precipitates are (largely) coherent with the ferrite matrix [24-27] and yet exhibit pronounced volume misfit with the matrix. The coherency of the precipitate/matrix interface gives rise to peculiar diffraction effects involving coherent diffraction of the assembly precipitate plus matrix (so no precipitate reflections occur) and asymmetrically

broadened diffraction-line profiles. It will be shown that the effect of misfit strain is sensitively expressed in lattice-parameter changes and that good agreement between theoretically predicted and experimentally measured data can be achieved.

3.2. Elastic strain field in a misfitting system: lattice-parameter changes

A continuum theory for the fully elastic accommodation of the misfit of a point imperfection in a matrix has been presented by Eshelby [28, 29]. The theory was developed to (also) predict the slope of the dependence of the lattice parameter of a crystalline solid solution on solute content (cf. Vegard´s law [30]). However, for this application the theory failed, as electronic interaction on the atomic scale can be dominant over elastic straining effects [18]. Therefore, the theory is more likely applicable to the case of precipitation of misfitting second-phase particles. On this basis, cases of particle-matrix misfit strain for elastically anisotropic matrices could be dealt with leading to the prediction of precipitate-particle shape [17, 31-33].

In the following subsections, formulae are presented that describe the changes of the relative volume/lattice-parameters of the matrix (section .32.1), the misfitting particles (inclusions; section .32.2) and of the assembly, i.e. matrix plus misfitting particles (inclusions; section .32.3)[1].

3.2.1. Change of the lattice parameter of the matrix

Insertion of the undeformed inclusions *B* in the holes of the matrix *A* leaves the whole assembly in a state of self-stress. Considering i) a *finite* matrix *A* containing, in the strain-free condition, holes of radius r_A^0 and ii) particles *B,* of strain-free radius r_B^0, the relative volume increase of the matrix *A* due to the insertion of the misfitting inclusions *B* into the holes of the matrix *A* can be written as [18]:

$$\frac{\Delta V_A}{V_A} = \frac{16}{3}\pi\frac{\mu_A}{K_A}C_6\varepsilon(r_A^\circ)^3 n \tag{3-1}$$

with

$$C_6 = \frac{3K_B}{3K_B + 4\mu_A} \tag{3-2}$$

where *n* is number of inclusions *B* per unit volume and *K* and μ represent the bulk modulus and the shear modulus, respectively. The linear misfit parameter, ε, can be calculated from $\left(r_B^\circ - r_A^\circ\right)/r_A^\circ = \left(\sqrt[3]{v_B^0} - \sqrt[3]{v_A^0}\right)\Big/\sqrt[3]{v_A^0}$, where v_B^0 and v_A^0 are the molar volumes of the strain-free precipitate particle and the matrix, respectively. The volume fraction of inclusion y_B can be taken as $y_B = 4\pi(r_B^\circ)^3 n/3$.

[1] In the derivations of the following formulae, in order to calculate the image force term for a *finite* matrix and a *finite* assembly, it is assumed that the volume fraction of misfitting particles is small: only the matrix elastic constants are used to calculate the image force term for matrix and assembly. Further, the matrix and the misfitting particles are taken to be elastically isotropic.

For the case of a matrix of cubic crystal structure with a (strain-free) lattice parameter a_A, $\Delta V_A/V_A$ can be approximated by $3\Delta a_A/a_A$, and Eq. (1) can be rewritten as [21]:

$$\Delta a_A = \frac{4\mu_A C_6}{3K_A}\frac{\varepsilon}{(1+\varepsilon)^3} y_B a_A \tag{3-3}$$

It is important to note that the matrix is of finite dimensions. In an *infinite* matrix, the volume change of the matrix due to the introduction of misfitting inclusions is zero (the matrix only experiences shear strains); then, the volume change of the assembly is fully confined to the precipitates. The matrix dilatation that is predicted for a matrix of *finite* size is a consequence of the image forces required to achieve a stress-free surface of the finite assembly.

3.2.2. Change of the lattice parameter of the misfitting phase

A misfitting inclusion with a radius larger or smaller than that of the hole in the matrix will experience hydrostatic compression or tension, respectively. For the case of a *finite* assembly of matrix *A* plus misfitting inclusions *B*, the fractional volume change of the inclusions can be written as [23]:

$$\frac{\Delta V_B}{V_B} = -3\varepsilon(1-C_6) + \frac{16}{3}\pi\frac{\mu_A}{K_B}C_6\varepsilon(r_A^\circ)^3 n \tag{3-4}$$

For the case of precipitates of cubic crystal structure with a (strain-free) lattice parameter a_B, $\Delta V_B/V_B$ can be approximated by $3\Delta a_B/a_B$, and it follows for the change of the lattice parameter, Δa_B, of the misfitting second phase:

$$\Delta a_B = \left[-\varepsilon(1-C_6) + \frac{4\mu_A C_6}{3K_B}\frac{\varepsilon}{(1+\varepsilon)^3} y_B\right] a_B \tag{3-5}$$

The total relative volume change of the inclusions results from the *sum* of the fractional volume change of the inclusions in an *infinite* assembly (first term in Eqs. (3-4) and (3-5)) and the fractional volume change of the inclusions due to the image forces acting (also) on the inclusions in a *finite* assembly (second term in Eqs. (3-4) and (3-5)).

3.2.3. Change of the lattice parameter of the assembly (matrix plus misfitting phase)

The relative volume change of the whole, finite assembly comprising the finite matrix and the misfitting inclusions can be given as [18]:

$$\frac{\Delta V}{V} = 4\pi C_6\varepsilon(r_A^\circ)^3 + \frac{16}{3}\pi\frac{\mu_A}{K_A}C_6\varepsilon(r_A^\circ)^3 n = 4\pi\frac{C_6}{C'_6}\varepsilon(r_A^\circ)^3 n \tag{3-6}$$

with

$$C'_6 = \frac{3K_A}{3K_A + 4\mu_A} \tag{3-7}$$

For an aggregate of cubic crystal structure and a (strain-free) lattice parameter a, thus approximating $\Delta V/V$ by $3\Delta a/a$, the resulting change of the lattice parameter, Δa, of the aggregate for a volume fraction y_B precipitate particles B is given by:

$$\Delta a = \frac{C_6}{C'_6}\frac{\varepsilon}{(1+\varepsilon)^3} y_B a \tag{3-8}$$

The total relative volume change of the assembly, analogous to the case of the relative volume change of only the inclusions, results from the *sum* of the fractional volume change of the inclusions in an *infinite* assembly (first term in Eq. (3-6) (this volume change is confined to the inclusions; cf. section .32.1)) and the fractional volume change of the assembly due to the image forces required to achieve a stress-free surface of the *finite* assembly (second term in Eq. (3-6)).

3.2.4. Coherent vs. incoherent diffraction of matrix and misfitting precipitates; consequences for interpretation of lattice-parameter changes

The coherent or incoherent nature of the diffraction by a second phase (here precipitate particles) with the diffraction by the matrix need not coincide with the occurrence of a coherent or incoherent nature of the interfaces between the second-phase particles and the matrix. Coherency/incoherency of diffraction depends on whether or not constructive interference of waves scattered by separate parts of the diffracting material (matrix and second phase) occurs. Incoherency of diffraction is a statistical phenomenon: parts of a specimen can be considered to scatter incoherently if the phase difference (given as reduced modulo 2π) between a wave scattered in one part and a wave scattered in another part takes any value between zero and 2π with equal probability [7, 35].

Thus, because of the variability of the phase jump at an *incoherent* boundary between a second-phase particle and the matrix, due to its irregular structure, it appears likely that in this case the second-phase particles and the matrix diffract independently, i.e. incoherently, and in the diffraction pattern separate diffraction peaks of the second-phase particles and the matrix occur [7, 35].

For *coherent* (and semi-coherent) interfaces, more complicated diffraction effects can be expected. If a misfit between the second-phase particles and the matrix exists, lattice distortions, due to elastic accommodation, occur in the matrix and the second-phase particles, especially close to the particle/matrix interfaces. The phase difference between waves scattered by the matrix and waves scattered by second-phase particle depends on both the position (difference) vector from one scatterer (in the matrix) to the other one (in the particle) and the value of the diffraction angle (i.e. the length of the diffraction vector). Then, given the imperfect (strained) but (semi-)coherent crystal structure of the entity matrix/second-phase particles, it depends on the length of the diffraction vector if coherent or incoherent diffraction occurs. The occurrence of coherent diffraction implies that each peak in the diffraction pattern represents diffraction of the whole assembly of matrix plus second-phase particles [7, 35].

Provided matrix and precipitate diffract independently, i.e. incoherent diffraction of matrix and of precipitates occurs, the changes of the lattice parameters of the matrix and of the precipitates can be determined from measurements of the positions of the (separate) X-ray diffraction peaks of the matrix and of the precipitates. In that case, Eqs. (3-3) and (3-5) predict the changes of the lattice parameters of the matrix and the precipitates, respectively. If a coherent nature of the precipitate/matrix interfaces prevails, then, dependent on the length of the diffraction vector and the extent of misfit-strain variation, coherent diffraction by precipitate phase and matrix can occur, in which case the change of the lattice parameter derived from the position of the diffraction peaks is predicted by Eq. (3-8).

3.3. Experimental

To exclude the presence of macroscopic stresses, usually present in heterogeneously nitrided specimens, thin foil specimens of Fe-Cr and powder specimens of Fe-V alloys, which both can be homogeneously nitrided, were employed in this study.

3.3.1. Specimen preparation

Fe-2.0 at.%Cr and Fe-4.5 at.%Cr alloys were prepared by melting appropriate amounts of pure Fe (99.98 wt.%) and pure Cr (99.999 wt.%) in an Al_2O_3 crucible in an inductive furnace under a protective argon atmosphere (99.999 vol.%). After casting, the alloys had a cylindrical shape with a diameter of 10 mm and a length of 100 mm.

Fe-V powders of various V contents were procured from Nanoval GmbH&Co.KG, which had produced the Fe-V alloy powders from pure Fe (99.8 wt.%) and pure V (99.6 wt.%) by spray atomization of the alloy melt according to the Nanoval-process [36] under a high-velocity Ar-stream. The mean particle diameter of the Fe-0.9 at.%V powder was $d_{50} = 17.2$ µm, of the Fe-3.5 at.%V powder $d_{50} = 19.8$ µm and of the Fe-1.8 at.%V powder $d_{50} = 9.9$ µm. Preliminary investigations with powders of different particle sizes of the same alloy had shown no influence of the particle size on the nitriding response.

The compositions of the cast Fe-Cr alloys and the spray-atomized Fe-V powders were determined by chemical analysis; the results have been gathered in Table **3-1**. The contents of Cr, V and metal impurities (negligible) were determined by inductive coupled plasma optical emission spectroscopy (ICP-OES); the O and N contents were determined by carrier gas hot extraction and the C and S contents were determined by a combustion method.

The cast Fe-Cr alloys were cold-rolled to sheets with a thickness of 1 mm. The obtained sheets were annealed for 2h at 700 °C to get a recrystallized grain structure and further cold-rolled to foils with a thickness of 0.2 mm. Rectangular pieces of approximate lateral dimensions 10 mm × 10 mm

were cut from the foil and ground to a thickness of less than 100 µm. Subsequently, the specimens were annealed at 700 °C for 2 h under flowing H_2 atmosphere to obtain a recrystallized grain structure. The average grain size measured from the optical macrographs recorded from the recrystallized specimens is 50-60 µm. Before nitriding, the thin foils were polished (last step: 1 µm diamond suspension) and cleaned with ethanol.

Table 3-1. Results of chemical analysis of the massive Fe-Cr alloys and the Fe-V alloy powders.

alloy	Cr, V		O	N	C	S
	(at.%)	(wt.%)	(wt.%)	(wt.%)	(wt.%)	(wt.%)
Fe-2.0 at.%Cr	2.03±0.02	1.90±0.02	0.008	<0.001	<0.002	<0.002
Fe-4.5 at.%Cr	4.54±0.05	4.24±0.01	0.018±0.001	<0.004	0.002±0.001	<0.001
Fe-0.9 at.%V	0.90±0.01	0.82±0.01	0.020±0.003	<0.002	0.003±0.001	<0.001
Fe-1.8 at.%V	1.79±0.02	1.64±0.02	0.014±0.003	<0.002	0.004±0.002	<0.001
Fe-3.6 at.%V	3.56±0.04	3.26±0.04	0.022±0.003	<0.002	0.003±0.001	<0.001

3.3.2. Nitriding and de-nitriding experiments

For nitriding, the Fe-Cr thin foils were suspended with a quartz fiber in a vertical quartz tube furnace and the Fe-V powders were deposited onto a quartz half-tube slider and inserted into a horizontal quartz tube furnace. The furnaces have a temperature accuracy of ±1 K. Nitriding was performed in an ammonia/hydrogen gas flux (purity: H_2: 99.999 vol. %, NH_3: >99.998 vol. %). The nitriding parameters used have been gathered in

Table **3-2**. All nitriding conditions have been chosen such that only a diffusion zone (ferrite with dissolved N and alloying element nitride particles) develops, i.e. other Fe-N phases such as iron-nitrides and Fe-N austenite do not develop. The applied nitriding conditions led to homogenously nitrided Fe-2.0at. % Cr thin foils, implying that, after through nitriding, the nitrogen level at all depths in the specimen increased identically as a function of time. This leaves the specimen free of macroscopic stresses, due to the absence of a concentration-depth gradient even before full N saturation (i.e. precipitation of all Cr as CrN and saturation of the remaining ferrite matrix with dissolved N) had been attained for the foil. The Fe-V powder specimens were nitrided until the saturation level of N uptake had been realized (i.e., all V had precipitated as VN and the remaining ferrite matrix was saturated with dissolved nitrogen). Subsequently, some of the nitrided Fe-Cr thin foils and some of the Fe-V powder specimens were de-nitrided in pure H_2 at 400 °C for 16 h and then slowly cooled to the room temperature. At the employed denitriding conditions both CrN and VN are stable and the less strongly bonded dissolved N diffuses out [37-39].

Table 3-2. Applied nitriding parameters for the different Fe-Cr foils and the different Fe-V powders. For all treatments fluxes of 43 ml/min NH_3 and 456.4 ml/min H_2 were applied, which corresponds with a nitriding potential [49] of $r_N = 0.1$ atm$^{-1/2}$

composition	nitriding temperature (°C)	nitriding time (h)
Fe-2.0 at.% Cr	450	72, 144, 216,…, 792
	500	16
Fe-4.5 at.% Cr	500	2.25
Fe-0.9 at.% V	500	4
Fe-1.8 at.% V	500	4
Fe-3.6 at.% V	500	4

3.3.3. Specimen characterization

3.3.3.1. Weight measurement

Fe-Cr thin foils were weighed before nitriding, after nitriding and after subsequent denitriding using a Mettler Toledo UMX2 microbalance with an accuracy of ±1 µg.

3.3.3.2. Electron probe microanalysis (EPMA)

EPMA was performed on the cross-sections of nitrided and de-nitrided Fe-4.5at.%Cr thin foils. For these measurements, a Cameca SX100 microprobe (acceleration voltage $U = 10$ kV, current $I =$ 100 nA, spot size about 1 µm) equipped with five wavelength-dispersive spectrometers was used. To obtain the element contents at each measurement point, the intensities of the characteristic X-ray emission peaks were measured and divided by the corresponding intensities obtained from standard samples of pure Fe, Cr and γ′-Fe_4N (for N-K_α). Elemental concentrations were calculated from the intensity ratios applying the $\Phi(\rho z)$ approach [40].

3.3.3.3. X-ray and synchrotron diffraction

XRD measurements were performed on the surface of unnitrided, nitrided and denitrided specimens (Fe-Cr thin foils and Fe-V powders) using a PANalytical X'Pert diffractometer with Bragg-Brentano configuration, equipped with a Co tube and a graphite monochromator in the diffracted beam to suppress the components other than $Co_{K\alpha}$ radiation. The diffraction-angle 2θ range of 30°-105° 2θ was scanned with a step size of 0.009° 2θ.

The XRD patterns thus recorded were evaluated using the TOPAS software (Version 4.2, Bruker AXS). Each diffraction profile in the diffractogram recorded with Co-Kα radiation is composed of an α_1 component and an α_2 component [41]. The structural broadening of each of the components was fitted by three pV-functions; one for the main reflection and two for the tail (which is also referred as diffuse, scattered intensity in the literature [14]) (for discussion, see section .34). The instrumental profile was obtained from a measured standard LaB_6 powder diffraction pattern. This instrumental broadening was incorporated into the fitting of the measured diffraction profiles by convolution with the pV-functions describing the specimen (structural) broadening. An example of the original measured data, the total fit and the corresponding fits of the α_1 and α_2 components is presented in Figure **3-1**. The 2θ-positions of the maximum intensities of the pV-profiles of the main peaks describing the specimen broadening only were then used for determination of the lattice parameters as described next.

In the case of the (de-)nitrided Fe-Cr thin foil a value of the lattice parameter and a value of the specimen displacement [42], were obtained by fitting to the 110, 200 and 211 ferrite-reflection positions determined as described above.

In the case of the (de-)nitrided Fe-V powder specimens, a powder specimen was mixed with Si-standard powder to determine, from the Si peak positions in the measured diffractograms and the known value of the Si lattice parameter [43], the instrumental zero-point 2θ offset and the specimen displacement. Then a value of the lattice parameter was obtained by fitting to the 110, 200, 211 and 220 ferrite-reflection positions determined as described above.

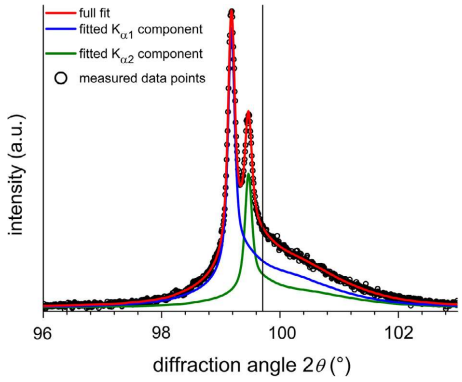

Figure 3-1. Comparison of measured 211 diffraction peak (Co-Kα radiation) of Fe-2.0 at.%Cr specimen, nitrided at 450°C for 720 h with a nitriding potential of 0.1 $atm^{-½}$, with the corresponding TOPAS fit and the corresponding $K\alpha_1$-component. The $K\alpha_1$-peak position for pure, unnitrided ferrite (α-Fe) has been indicated.

High-resolution powder diffraction data from the nitrided Fe-V powders were collected on the beamline ID31 of the European Synchrotron Radiation Facility (ESRF). A Si 111 reflection was used to select an X-ray energy of 41.3 keV. The size of the beam was adjusted using slits. The wavelength

was determined as 0.300715 ± 0.000005 Å from a silicon standard of known lattice parameter (NIST SRM640c). The nitrided Fe-V powder specimen was contained in a 1.0 mm borosilicate glass capillary, which was, during measurement, rotated around its length axis in order to improve orientation randomization of the diffracting crystallites. The diffracted beam was analyzed with a nine-crystal analyzer stage (nine Ge 111 crystals separated by 2° intervals) and detected with nine Na(Tl)I scintillation counters simultaneously. The recorded data were converted to a step scan for values of 2θ from 0.5 to 33.90° in steps of 0.002°. Evaluation was performed by a simultaneous fit of a pV-function to a main peak and a pV-function to its intensity tail employing the TOPAS software. No deconvolution of the instrumental and specimen profiles was performed for these data (no precise lattice-parameter values needed to be extracted from these data; see section .34). Thus, the respective 2θ positions, $2\theta_1$ for each main peak and $2\theta_2$ for each intensity tail, and the corresponding peak areas I_1 and I_2, were determined.

3.4. Results and Evaluation

Upon nitriding the Fe-Cr thin foil and Fe-V powder specimens, under the nitriding conditions described above, a homogenous N-distribution is achieved throughout the specimen. A considerable peak shift of the ferrite reflections towards lower diffraction angles occurs. This is shown exemplarily by the evolution of 211 ferrite diffraction-line profiles recorded for various Fe-Cr and Fe-V specimens in Figure **3-2**. The magnitude of peak shift increases with nitriding time for the Fe-2.0 at.%Cr specimen implying that an increased amount of CrN precipitation leads to an increased shift of the peak (Figure **3-2**(a)). The Fe-V powders nitrided until saturation (i.e. until precipitation of all V as VN) indicate that the higher the amount of V in the alloys, i.e. the higher the amount of VN precipitation, the larger is the shift of the ferrite reflection towards lower diffraction angles (Figure **3-2**(b)-(d)). The same is observed when comparing nitrided Fe-2.0 at.%Cr and Fe-4.5 at.%Cr alloys (not shown). Also, as shown in Figure **3-2**, an intensity tail towards higher diffraction angles is present for both the nitrided Fe-Cr and the nitrided Fe-V alloys. The N-saturated specimens (achieved after 792 h of nitriding for the Fe-2.0 at.%Cr alloy thin-foil specimens) were subsequently subjected to a denitriding treatment until no further N is lost from the specimen. After denitriding, a partial shift of the ferrite reflection (back) towards higher 2θ is observed.

From the synchrotron measurements, a more detailed evaluation of the intensity tail is possible because also higher order reflections are detectable (with significant intensity) within the accessible 2θ range, see Figure **3-3**. For each observed reflection, the refined positions $2\theta_1$ and $2\theta_2$ due to the main peak and the intensity tail (c.f. section 3.3.3.3), were converted into reciprocal lattice spacings, d^*, according to:

$$d^*_{1,2} = \frac{2\,sin\,\theta_{1,2}}{\lambda} \tag{3-9}$$

The distance between the main peak and intensity-tail positions in reciprocal space then follows from $\Delta d^* = d_2^* - d_1^*$. The value of Δd^* has been plotted as function of d_1^* in Figure **3-4**(a). The indeterminacy of the refined 2θ positions was used to assess the error in Δd^* by error propagation, which has been indicated in Figure **3-4**(a). The fraction of the intensity-tail area with respect to the total reflection area (ratio of integrated intensity of the intensity tail to the sum of the integrated intensities of main peak and intensity tail, $\left(\frac{I_2}{(I_1+I_2)}\right)$) is presented as function of d_1^* in Figure **3-4**(b).

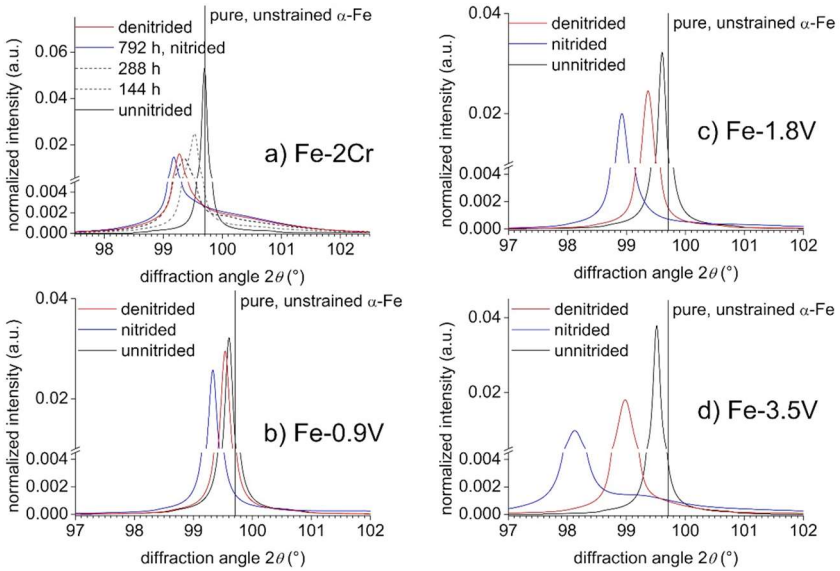

Figure 3-2. Evolution of the ferrite 211 reflection of thin-foil Fe-Cr alloy (thickness 85 μm) specimens (a) and Fe-V alloy powder specimens (b) – d)) upon nitriding and denitriding. The shown profiles result after subtracting from the measured profile the $K_{\alpha 2}$ component as well as removing the instrumental profile as described in section 3.3.3.3. a) Fe-2.0 at.%Cr thin foil with a thickness of approx. 85 μm nitrided at 450 °C with a nitriding potential of 0.1 $atm^{-½}$ in steps of 72 h to a total of 792 h (only some of the intermediate nitriding steps are shown here). The result after a denitriding treatment in flowing H_2 atmosphere at 400 °C for 16 h is shown as well. b-d) Fe-V powders of indicated compositions, nitrided for 4 h at 500 °C with a nitriding potential of 0.1 $atm^{-½}$. The results after a denitriding treatment at 400 °C for 16 h in flowing H_2 atmosphere are shown as well. The profiles reveal the shifts of the diffraction-line profile towards lower diffraction angle upon (prolonged) nitriding and a partial shift back upon denitriding.

If it would be assumed that main peak and intensity tail represent incoherent diffraction by two different phases, specific relationships for Δd^* vs. d_1^* are expected. For example, if two different bcc (as ferrite) phases would be present, the dependence of Δd^* on d_1^* would be linear: a straight line of positive slope passing through the origin in Fig. 4a. Clearly, this is not the case. The surroundings of the nitride platelet are affected by a strain field of tetragonal symmetry and it has been suggested that this tetragonally distorted ferrite could diffract independently from the undistorted ferrite [27].

However, also in this case, Δd^* would show an overall increase with d_1^*, which is not the case. Moreover, the relative intensity of the intensity tail $\left(\frac{I_2}{(I_1+I_2)}\right)$ would be more or less constant as function of d_1^*, if incoherent diffraction of two phases would occur, as the integrated intensity of a diffraction peak is proportional to the diffracting volume. Such constancy is not observed (Figure **3-4**(b)). It has been suggested in Ref. [13] (see also Ref. [16]) that strong strain fields surrounding defects (e.g. misfitting precipitates) in crystals can lead to scattered intensity adjacent to the main peaks (c.f. Ref. [14]), which can be well compatible with the present experimental results. It is concluded, that the reflection lines comprised of "main peak" and "intensity tail" represent diffraction by a single, distorted phase.

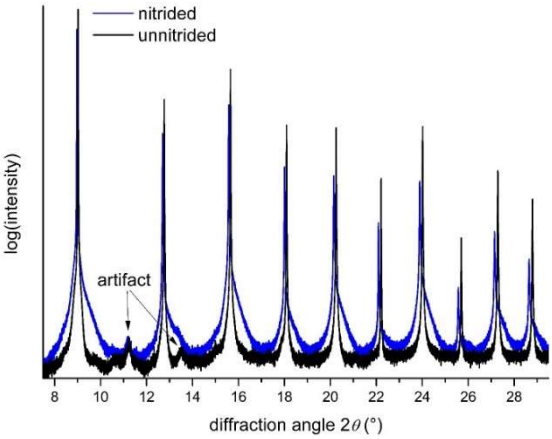

Figure 3-3. Diffractograms (synchrotron diffraction, λ=0.300715 Å, c.f. section 3.3.3.3) of Fe-1.8 at.%V powder specimens before nitriding and after nitriding at 500 °C for 4 h with a nitriding potential of 0.1 $atm^{-½}$. Upon nitriding a distinct shift of the diffraction-line profiles towards lower diffraction angles and the development of an intensity tail towards higher diffraction angles occur. The small reflections at approx. 11 and 13.5 ° 2θ are artifacts due to irregularities in the instrumental background.

3.5. Discussion

At first sight, the shift of the main, ferrite-matrix reflection to lower diffraction angles upon nitriding might be ascribed to isotropic expansion of the lattice. Substitutional solute (Cr, V) depletion of the matrix, by nitride precipitation, leads to a minor lattice-parameter *decrease* ($-0.0005\frac{\text{Å}}{at.\%}$ for Cr in ferrite and $-0.001\frac{\text{Å}}{at.\%}$ for V in ferrite in the compositional range for the alloys employed in this study [44]), as compared to the observed major lattice-parameter *increase* (e.g. approx. $+0.0109$ Å

for fully N-saturated Fe-2.0 at.%Cr alloy, cf. Table 3). Interstitial dissolution of nitrogen leads to lattice-parameter increase ($+0.0079\frac{\text{Å}}{at.\%}$ for dissolution of N in pure ferrite [45, 46]).

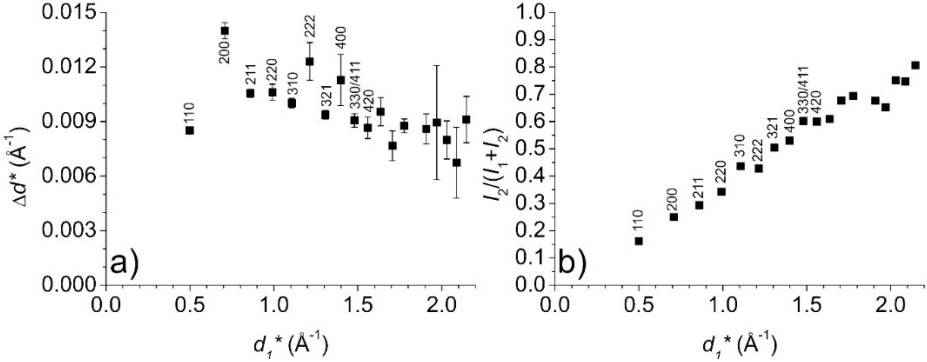

Figure 3-4. Evaluation of the synchrotron diffraction data of nitrided Fe-1.8 at.%V powder specimens (cf. Fig. 3). a) The distance in reciprocal space, Δd^*, between positions of the main reflection d_1^* and the intensity tail d_2^*, as a function of the length of the diffraction vector, d_1^*; b) The relative intensity of the tail, $I_2/(I_1+I_2)$, as a function of the length of the diffraction vector, d_1^*.

However, the amount of dissolved nitrogen (N not precipitated in the form of CrN or VN) is much too small to explain the observed effect (cf. Table **3-3**). Moreover, after removing all dissolved N by a denitriding treatment, the ferrite lattice remains in expanded state (cf. Figure **3-2**). It will be argued below, qualitatively and quantitatively, that the observed lattice-parameter increases, as compared to the condition before nitriding, can be ascribed to the elastic accommodation of the precipitate/matrix misfit based on the model described in section 3.2.

Previous TEM, HRTEM and XRD analyses of nitrided Fe-Cr and Fe-V alloys have shown that the tiny CrN and VN platelets in the nitrided alloys are largely coherent with the surrounding finite matrix [12, 24-27]: a largely elastic accommodation of the precipitates/matrix misfit is likely. Then, depending on whether coherent *diffraction* of the precipitates with the matrix occurs or not, the lattice-parameter change should be compared with the theoretical prediction according to either Eq. (3-8) (for coherent diffraction of the precipitates with the matrix) or Eq. (3-3) (for incoherent diffraction of the precipitates and the matrix); see section 3.2.4.

In order to realize a quantitative comparison of predicted and measured lattice-parameter change, the amount of precipitate and the amount of dissolved nitrogen should be known for each specimen. These values were determined by the following procedure utilizing denitriding experiments.

Table 3-3. N contents, volume fraction of nitride precipitates and strain-free lattice-parameters determined for Fe-Cr thin foils from nitriding and nitriding plus subsequent denitriding experiments. All thin foils contain 2 at.% Cr except the data presented in the last row which pertain to a specimen containing 4.5 at.%Cr. The volume fraction of CrN nitride was calculated using the N content after denitriding (denitriding was performed at 400°C for selected specimens). Data in the last three rows correspond to the complete precipitation of Cr as CrN. The amount of dissolved N shown in column 5 is the difference in the nitrogen content of the nitrided and denitrided specimens.

nitriding temperature (°C)	nitriding time (h)	N content after nitriding (at.%)	N content after denitriding (at.%)	dissolved N (at.%)	volume of CrN precipitates (vol.%) y_{CrN}	a_α after nitriding (Å)	a_α after denitriding (Å)
450	0	0	0		0	2.8664	
450	72	0.330†				2.8688	
450	144	0.696†				2.8701	
450	216	1.092†	0.798†	0.294		2.8724	2.8699
450	288	1.361†				2.8736	
450	360	1.615†				2.8752	
450	432	1.738†				2.8761	
450	504	1.777†				2.8765	
450	576	1.844†				2.8767	
450	648	1.899†				2.8769	
450	720	1.925†				2.8772	
450	792	1.949†	1.691†	0.258	2.366	2.8773	2.8752
500	16	2.260†	1.900†	0.360	2.821	2.8818	2.8767
500	2.25	4.620‡	4.2‡	0.42	6.022	2.8967	2.8891

† N-content determined by weight uptake of the specimen after treatment, ‡ N-content determined by EPMA

It has been demonstrated by previous nitriding/denitriding experiments on Fe-Cr [47] and Fe-V [38] alloys that the developing nitrides form with a stoichiometry of N to *Me* of 1:1, i.e. as CrN and VN nitrides. The atomic fraction of N in the homogenously nitrided and subsequently denitrided specimen, as determined by weighting before nitriding and after subsequent denitriding, x_N, corresponds to the fraction of alloying element *Me* precipitated as nitride *Me*N, x_{MeN} (i.e. $x_{MeN} = x_N$). The volume fraction of nitride precipitates, y_{MeN}, can then be determined from x_{MeN} according to:

$$y_{MeN} = \frac{x_{MeN} v_{MeN}}{x_{MeN} v_{MeN} + (1 - x_{MeN}) v_\alpha} \tag{3-10}$$

where v_{MeN} and v_{α} are the molar volumes of *Me*N and α-Fe (which can be calculated from the corresponding lattice-parameter data [34, 43]). The thus calculated volume fractions of nitride precipitates and the deduced amounts of dissolved nitrogen after nitriding for the nitrided Fe-Cr and Fe-V specimens have been gathered in Table **3-3** and Table **3-4**, respectively.

Table 3-4. N contents and lattice parameters determined for Fe-V powders from nitriding and nitriding plus subsequent denitriding experiments. The volume fraction of VN nitride was calculated using the N-content after denitriding, which is taken to correspond to the nominal V-content (in at.%) of the unnitrided alloy determined by chemical analysis. All V (of the respective alloy) is completely precipitated as VN in the specimens.

alloy	Nitriding temperature (°C)	N content after nitriding (at.%)	N content after denitriding (nominal V-content) (at.%)	volume of VN precipitates (vol.%) y_{VN}	a_{α} after nitriding (Å)	a_{α} after denitriding (Å)
Fe-0.9 at.%V	500	1.196	0.9	1.349	2.8744	2.8699
Fe-1.8 at.%V	500	2.539	1.8	2.686	2.8830	2.8736
Fe-3.4 at.%V	500	4.864	3.4	5.178	2.9004	2.8816

The amounts of dissolved nitrogen in both alloys for the fully nitrided (saturated) specimens are much larger than the equilibrium amount of nitrogen dissolved in pure unstrained ferrite (compare values indicated in Table **3-3** for Fe-Cr thin-foils and in Table 4 for Fe-V specimens with N contents obtained from the N-absorption function for pure ferrite (α-Fe) given in [49]: 0.033 at.%N at 450 °C with r_N=0.1 atm$^{-1/2}$ and 0.075 at.%N at 500°C with r_N=0.1 atm$^{-1/2}$). This occurrence of "excess nitrogen" is well known and can be ascribed to the (additional) uptake of nitrogen by adsorption of nitrogen at the precipitate-platelet faces and increased ferrite-lattice dilatation due to the hydrostatic stress component of the stress-field induced by the precipitate/matrix misfit [37, 38, 47, 48].

Now, for the denitrided specimens (systems of *Me*N precipitates in a pure ferrite matrix) the difference of their lattice parameter and that of a single-phase pure ferrite specimen (2.8664 Å [43]) has been plotted in Figure **3-5**(a), (b) as function of the amount of *Me*N precipitates for both alloys. In the same figures the predictions for this lattice-parameter difference according to Eq. (3-3) (precipitates diffract separately) and Eq. (3-8) (precipitates diffract coherently with the matrix) have been indicated as well (values for materials constants used in Eqs. (3-3) and (3-8) have been gathered in Table **3-5**). Evidently, the predicted lines for expansion of the whole assembly, precipitate plus matrix (i.e. Eq. (3-8)) agree very well with the experimental data for both alloy systems in the

denitrided state. The lattice-parameter shifts predicted for separate diffraction by precipitates and matrix are distinctly smaller than the experimental data for the denitrided state.

Table 3-5. Values of constants used in the model calculations of lattice dilatation

	Fe	**CrN**	**VN**
a_0 **[Å]**	2.8664 [42]	4.1400 [42]	4.1392 [42]
K [GPa]	166 [52]	360 [53]	300 [54]
μ **[GPa]**	82 [52]	(unnecessary)	(unnecessary)

Considering the simplicity of the applied model (section 3.2) and because of the uncertainty about the values of the elastic constants used in the model (the elastic constants for nitrides of nanoscopic size need not be equal to those of bulk material), the good agreement between the experimental lattice dilatation for the denitrided specimens and the model prediction according to Eq. (3-8) is remarkable: the model not only well accounts for the difference in alloy systems (different extent of precipitate/matrix misfit and different elastic properties of the precipitates (cf. Table **3-5**) but also well describes the dependency on the amount (volume fraction) of precipitates.

The minor discrepancy between measured and model-predicted lattice parameters for the Fe-V powders can be attributed to (i) the small amount of V being oxidized owing to the large surface-area per unit volume of the Fe-V powders as compared to the Fe-Cr foils (see also Ref. [38]) and/or (ii) a possible relaxation of part of the elastically accommodated misfit during coarsening of VN particles upon denitriding; the chemical driving force available for the precipitation of VN is larger than for CrN [50], which results in a relatively much smaller size of the VN particles, which consequently implies a larger driving force for the coarsening of the VN particles as compared to the CrN particles.

This result is the first time demonstrating that coherent diffraction of the precipitates with the matrix is associated with a distinct lattice-parameter shift of the *assembly* compatible with elasticity theory. The only case known to us of observed lattice-parameter shift in agreement with prediction on the basis of elastic accommodation of precipitates/matrix misfit pertains to precipitates and matrix diffracting independently (i.e. Eq. (3-3) instead of Eq. (3-8) holds): a system of Si precipitates in an Al matrix [21].

In the investigation of Ref. [21] the volume misfit of Si precipitates and Al matrix, with ε_V as linear misfit parameter, was completely relaxed after the completion of precipitation at elevated temperature (in flagrant contrast with the present system). Then cooling of the specimens from annealing temperature T_A to room temperature T_{RT} resulted in a thermal misfit with linear misfit parameter $\varepsilon_T = \Delta\alpha \times (T_A - T_{RT})$ due to the difference in thermal expansion coefficients of matrix and second-phase particles, $\Delta\alpha$. This thermal-misfit effect gave rise to the change of lattice parameter of the Al matrix, measured and predicted (according to Eq. (3)) in Ref. [21]. Such thermal misfit is in

principle also present in the current system of second-phase nitride particles in the ferrite matrix (for which Eq. (3-8) applies), but the magnitude of thermal misfit ε_T is negligible as compared to the volume misfit ε_V due to the precipitate formation: for nitrided Fe-Cr alloys, $\varepsilon_V = 0.1464$ and $\varepsilon_T = 0.0044$ for cooling from 400 °C to 25 °C, for nitrided Fe-V alloys, $\varepsilon_V = 0.1461$ and $\varepsilon_T = 0.0022$ for cooling from 400 °C to 25 °C, (employing thermal expansion coefficients from [51, 52])).

As a last note, it is remarked that for both cases (i.e. applicability of either Eq. (3-3) or Eq. (3-8)) it is essential to apply elasticity theory for a finite matrix; predictions for an infinitely large matrix do not apply at all.

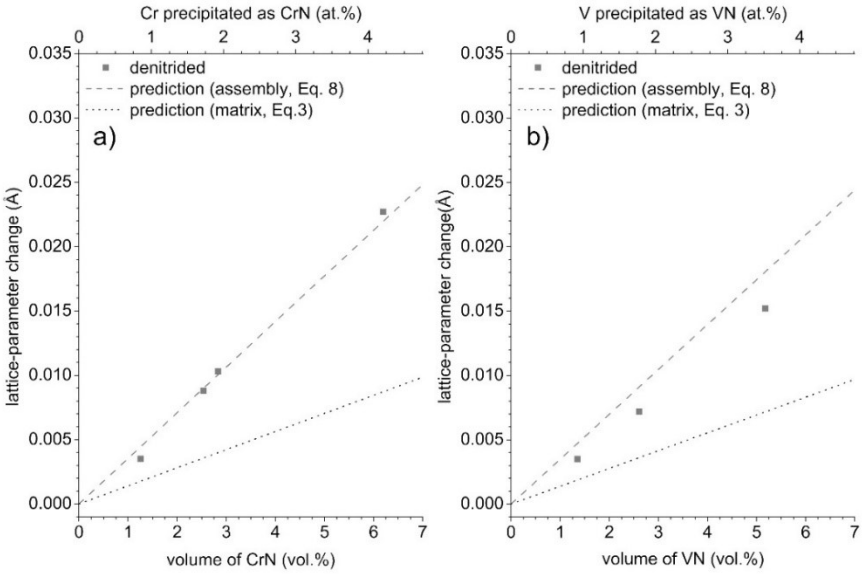

Figure 3-5. Comparison of model predicted and experimental data for the difference of the lattice parameter of denitrided a) Fe-Cr and b) Fe-V specimens and the lattice parameter of pure, single-phase ferrite as function of the amount of precipitated nitride phase. Model predictions for the lattice expansion corresponding to coherent diffraction of the whole assembly (nitride precipitates and ferrite matrix), i.e. Eq. (3-8), and corresponding to separate (incoherent) diffraction (of nitride precipitates and ferrite matrix), i.e. Eq. (3-3), have been indicated by the dashed lines.

3.6. Conclusions

Coherent diffraction by an assembly composed of precipitates and matrix leads, for the case of elastic accommodation of the precipitate-matrix misfit, to lattice-parameter changes, which can be

well predicted adopting a theory originally developed by Eshelby for point imperfections for the case of *finite* size of the assembly.

The, according to the above, theoretically predicted dependences of lattice-parameter change on both degree of misfit and amount of precipitates, well agree with the experimental observations for nitrided Fe-Cr and Fe-V alloys, which exhibit a microstructure consisting of tiny, coherent nitride platelets in a severely distorted ferritic matrix.

The reflections recorded from the nitrided Fe-Cr and Fe-V alloys exhibit intensity tails at the high diffraction-angle side, which represent the highly tetragonally distorted regions surrounding the precipitates; the specimens diffract as a single phase.

Acknowledgements

We thank Mr. P. Kress for assistance with the nitriding experiments and Mrs. S. Haug for assistance with the EPMA experiments (both with the Max Planck Institute for Intelligent Systems). We also thank the European Synchrotron Radiation Facility (ESRF) for provision of synchrotron radiation facilities and Dr. Caroline Curfs (ESRF) and Dr. Silke Kurz (Max Planck Institute for Intelligent Systems) for assistance during use of beamline ID31.

References

[1] M.H. Biglari, C.M. Brakman, E.J. Mittemeijer, Crystal-Structure and Morphology of AlN Precipitating on Nitriding of an Fe-2 at Percent Al-Alloy, Philos. Mag. A 72 (1995) 1281-1299.

[2] M. Sennour, C. Esnouf, Contribution of Advanced Microscopy Techniques to Nanoprecipitates Characterization: Case of AIN Precipitation in Low-Carbon Steel, Acta Mater. 51 (2003) 943-957.

[3] Y.C. Liu, F. Sommer, E.J. Mittemeijer, Abnormal Austenite-Ferrite Transformation Behaviour in Substitutional Fe-Based Alloys, Acta Mater. 51 (2003) 507-519.

[4] S. Loewy, B. Rheingans, S.R. Meka, E.J. Mittemeijer, Unusual Martensite-Formation Kinetics in Steels: Observation of Discontinuous Transformation Rates, Acta Mater. 64 (2014) 93-99.

[5] M. Villa, K. Pantleon, M.A.J. Somers, Evolution of Compressive Strains in Retained Austenite during Sub-Zero Celsius Martensite Formation and Tempering, Acta Mater. 65 (2014) 383-392.

[6] S.R. Meka, E. Bischoff, B. Rheingans, E.J. Mittemeijer, Octapod-Shaped, Nanosized, Amorphous Precipitates in a Crystalline Ferrite Matrix, Phil. Mag. Lett. 93 (2013) 238-245.

[7] E.J. Mittemeijer. Fundamentals of Materials Science, Springer, Berlin, 2010.

[8] S.J. Song, F. Liu, Z.H. Zhang, Analysis of Elastic-Plastic Accommodation due to Volume Misfit upon Solid-State Phase Transformation, Acta Mater. 64 (2014) 266-281.

[9] R. Abbaschian, L. Abbaschian, R.E. Reed-Hill, Physical Metallurgy Principles. fourth ed., Course Technology, Stamford, 2010.

[10] M.F. Ashby, L.M. Brown, On Diffraction Contrast from Inclusions, Philos. Mag. 8 (1963) 1649-1676.

[11] M.F. Ashby, L.M. Brown, Diffraction Contrast from Spherically Symmetrical Coherency Strains, Philos. Mag. 8 (1963) 1083-1103.

[12] T.C. Bor, A.T.W. Kempen, F.D. Tichelaar, E.J. Mittemeijer, E. van der Giessen, Diffraction-Contrast Analysis of Misfit Strains around Inclusions in a Matrix: VN Particles in α-Fe, Philos. Mag. A 82 (2002) 971-1001.

[13] S.C. Moss, M.A.c. Krivoglaz, Theory of X-ray and Thermal-Neutron Scattering by Real Crystals, Plenum Press, New York, 1969.

[14] R. Kuzel, B. He, C. Houska, Characterization of Severe Matrix Distortions during Phase Separation from the Redistribution of Diffracted Intensities, J. Mater. Sci. 32 (1997) 2451-2467.

[15] E.J. Mittemeijer, U. Welzel, Modern Diffraction Methods, Wiley-VCH, Weinheim, 2013.

[16] A.J. Guinier, X-ray Diffraction in Crystals, Imperfect Crystals, and Amorphous Bodies, Freeman, first ed., California, 1963.

[17] A.G. Khachaturyan, The Theory of Structural Transformations in Solids, Wiley, New York, 1983.

[18] J.W. Christian, The Theory of Transformations in Metals and Alloys, second ed., Pergamon Press, Oxford, 1975.

[19] M.R. Ahmadi, E. Povoden-Karadeniz, B. Sonderegger, K.I. Oksuz, A. Falahati, E. Kozeschnik, A model for coherency strengthening of large precipitates, Scr. Mater. 47 (2014) 84-85.

[20] P.H. Leo, J.S. Lowengrub, Q. Nie, On an Elastically Induced Splitting Instability, Acta Mater. 49 (2001) 2761-2772.

[21] E.J. Mittemeijer, P. van Mourik, T.H. de Keijser, Unusual Lattice-Parameters in 2-Phase Systems after Annealing, Philos. Mag. A 43 (1981) 1157-1164.

[22] P. van Mourik, E.J. Mittemeijer, T.H. de Keijser, On Precipitation in Rapidly Solidified Aluminium-Silicon Alloys, J. Mater. Sci. 18 (1983) 2706-2720.

[23] P. van Mourik, T.H. de Keijser, E.J. Mittemeijer, Misfit Strains and Excess Vacancies in Liquid-Quenched and Solid-Quenched AlSi Alloys on Aging, In: P. W. Lee, R. S. Carbonara (Eds.), Rapidly Solidified Materials: Proceedings of an International Conference , San Diego, 1985, pp. 341-350.

[24] M. Sennour, P.H. Jouneau, C. Esnouf, TEM and EBSD Investigation of Continuous and Discontinuous Precipitation of CrN in Nitrided pure Fe-Cr alloys, J. Mater. Sci. 39 (2004) 4521-4531.

[25] B. Mortimer, P. Grieveson, K.H. Jack, Precipitation of Nitrides in Ferritic Iron Alloys Containing Chromium, Scand. J. Metall. 1 (1972) 203-209.

[26] M. Gouné, T. Belmonte, A. Redjaimia, P. Weisbecker, J.M. Fiorani, H. Michel, Thermodynamic and structural studies on nitrided Fe-1.62%Mn and Fe-0.56%V alloys, Mat. Sci. Eng. A 351 (2003) 23-30.

[27] N.E. Vives Díaz, S.S. Hosmani, R.E. Schacherl, E.J. Mittemeijer, Nitride Precipitation and Coarsening in Fe–2.23at.% V alloys: XRD and (HR)TEM Study of Coherent and Incoherent Diffraction Effects Caused by Misfitting Nitride Precipitates in a Ferrite Matrix, Acta Mater. 56 (2008) 4137-4149.

[28] J.D. Eshelby, Distortion of a Crystal by Point Imperfections, J. Appl. Phys. 25 (1954) 255-261.

[29] J.D. Eshelby, The Continuum Theory of Lattice Defects, Solid State Phys. 3 (1956) 79-144.

[30] L. Vegard, The Constitution of the Mixed Crystals and the Filling of Space of the Atoms, Z. Phys. 5 (1921) 17-26.

[31] J.W. Morris, The Khachaturyan Theory of Elastic Inclusions: Recollections and Results, Philos. Mag. 90 (2010) 3-35.

[32] M. Fahrmann, P. Fratzl, O. Paris, E. Fahrmann, W.C. Johnson, Influence of Coherency Stress on Microstructural Evolution in Model Ni-Al-Mo Alloys, Acta Metall. Mater. 43 (1995) 1007-1022.

[33] W.C. Johnson, J.W. Cahn, Elastically Induced Shape Bifurcations of Inclusions, Acta Metall. 32 (1984) 1925-1933.

[34] W.B. Pearson, A Handbook of Lattice Spacings and Structures of Metals and Alloys, vol. 4. Pergamon, London, 1958.

[35] J.G.M. van Berkum, R. Delhez, T.H. de Keijser, E.J. Mittemeijer, Diffraction-line Broadening due to Strain Fields in Materials; Fundamental Aspects and Methods of Analysis, Acta Crystallogr. A 52 (1996) 730-747.

[36] M. Stobik, Nanoval Metal Powder - Market Requirements and Powder Characteristics, Adv. Eng. Mater. 2 (2000) 547-548.

[37] M.A.J. Somers, R.M. Lankreijer, E.J. Mittemeijer, Excess Nitrogen in the Ferrite Matrix of Nitrided Binary Iron-Based Alloys, Philos. Mag. A 59 (1989) 353-378.

[38] S.S. Hosmani, R.E. Schacherl, E.J. Mittemeijer, Nitrogen Uptake by an Fe-V alloy: Quantitative Analysis of Excess Nitrogen, Acta Mater. 54 (2006) 2783-2792.

[39] R. Schacherl, P. Graat, E. Mittemeijer, The Nitriding Kinetics of Iron-Chromium Alloys; The Role of Excess Nitrogen: Experiments and Modelling, Metall. and Mater. Trans. A 35 (2004) 3387-3398.

[40] J.L. Pouchou, F. Pichoir, A New Model for Quantitative X-Ray-Microanalysis .2. Application to in-Depth Analysis of Heterogeneous Samples, Rech. Aerospatiale (1984) 349-367.

[41] R. Delhez, E.J. Mittemeijer, An Improved Alpha-2 Elimination, J. Appl. Crystallogr. 8 (1975) 609-611.

[42] A.J.C. Wilson, Elements of X-ray Crystallography, Addison-Wesley, Reading, Massachusetts, 1970.

[43] ICDD Data Base, PCPDFWIN, 2002.

[44] A. Sutton, W. Hume-Rothery, The Lattice Spacings of Solid Solutions of Titanium, Vanadium, Chromium, Manganese, Cobalt and Nickel in α-iron, Philos. Mag. 46 (1955) 1295-1309.

[45] H.A. Wriedt, L. Zwell, Lattice Dilation of Alpha-Iron by Nitrogen, T. Metall. Soc. Aime. 224 (1962) 1242-1246.

[46] E.J. Mittemeijer, A.B.P. Vogels, P.J. van der Schaaf, Aging at Room-Temperature of Nitrided Alpha-Iron, Scripta Metall. Mater. 14 (1980) 411-416.

[47] S.S. Hosmani, R.E. Schacherl, E.J. Mittemeijer, Nitrogen Absorption by Fe-1.04at.%Cr Alloy: Uptake of Excess Nitrogen, J. Mater. Sci. 43 (2008) 2618-2624.

[48] H.H. Podgurski, F.N. Davis, Thermochemistry and Nature of Nitrogen Absorption in Nitrogenated Fe-Ti Alloys, Acta Metall. 29 (1981) 1-9.

[49] J. Stein, R.E. Schacherl, M.S. Jung, S. Meka, B. Rheingans, E.J. Mittemeijer, Solubility of Nitrogen in Ferrite; the Fe-N Phase Diagram, Int. J. Mater. Res. 104 (2013) 1053-1065.

[50] E.J. Mittemeijer, Fundamentals of Nitriding and Nitrocarburizing, in: J. Dossett, G.E. Totten (Eds.), ASM Handbook, vol. 4A. Steel Heat Treating Fundamentals and Processes, ASM International, Materials Park, 2013, pp. 619-646.

[51] Z. Basinski, W. Hume-Rothery, A. Sutton, F. Sutton, The Lattice Expansion of Iron, in: Mathematical, Physical and Engineering Sciences 229: Proceedings of the Royal Society A , 1955, pp. 459-467.

[52] G.V. Samsonov, Plenum Press Handbooks of High-Temperature Materials: No.2 Properties index, Plenum Press, New York, 1964.

[53] H. Wawra, Kröner-Limits of Elastic Moduli of Materials of Technical Importance. Part II: Elastic Moduli of Elements as Function of Temperature (in German), Z. Metallkde. 69 (1978) 518-523.

[54] J. Grossman, A. Mizel, M. Côté, M. Cohen, S. Louie, Transition Metals and Their Carbides and Nitrides: Trends in Electronic and Structural Properties, Phys. Rev. B 60 (1999) 6343-6347.

[55] D. Dzivenko, A. Zerr, N. Guignot, M. Mezouar, R. Riedel, Compressibility of Cubic Vanadium Mononitride, EPL Europhys. Lett. 92 (2010) 66001.

Chapter 4

Diffraction-line shifts and broadenings in continuously and discontinuously coarsening precipitate-matrix systems; coarsening of initially coherent nitride precipitates in a ferrite matrix

T. Steiner, M. Akhlaghi, S.R. Meka, and E.J. Mittemeijer

Abstract

The initial precipitation of misfitting particles can be accompanied by elastic accommodation of the precipitate/matrix misfit leading to considerable matrix lattice dilatation/contraction and variable lattice microstrain. In this stage, the entire assembly of matrix and precipitate particles, as a whole, can diffract coherently. Upon aging of the system, relaxation of the accommodated misfit can occur by continuous and/or discontinuous coarsening of the precipitates. These processes are associated with distinctly different, characteristic diffraction phenomena, also involving a transition from coherent to incoherent diffraction of precipitates and matrix. For the case of, initially fully coherent, alloying element nitrides in a homogeneously nitrided ferrite matrix, these effects have been identified and analyzed, thus allowing tracing of misfit-relaxation processes.

4.1. Introduction

Diffraction processes are sensitive to the imperfections of the crystalline solid state and thus diffraction methods are applied extensively for the study of the microstructure of materials [1-5]. In particular, X-ray diffraction (XRD) has been employed to characterize the (micro-) structural changes in a material upon precipitation of second phases, e.g. Refs. [6-10].

The precipitation of finely distributed misfitting nitride platelets in a ferrite matrix leads to hydrostatic expansion of the ferrite-matrix lattice [11, 12]. This lattice expansion was quantified with a model based on elastic accommodation of the misfit. The model was validated recently by comparison of its predictions for the lattice-parameter changes with the lattice-parameter changes as measured by XRD performed on homogeneously nitrided Fe-Cr and Fe-V alloys [12].

The lattice-parameter change discussed in the above paragraph pertains to the mean, long-range strain in the precipitate-matrix system. In the vicinity of the precipitate/matrix interfaces pronounced, local misfit-strain variations can occur [13]: microstrains giving rise to specific diffraction-line-broadening effects [1].

It is important to distinguish the case i) of precipitate particles coherent with the matrix and the case ii) of precipitate particles incoherent with the matrix. In both cases, elastic misfit accommodation of the precipitate-matrix misfit is possible depending on the origin and magnitude of the misfit (e.g. intrinsic lattice misfit vs. extrinsic thermal misfit). This leads to the following consequences for the (X-ray) diffraction experiment: in the first case i), particles and matrix can diffract coherently, and in the second case ii) particles and matrix likely diffract incoherently (c.f. discussion in Ref. [14]).

The first described situation (case i)) pertains to the particle-matrix systems considered here: the tiny nitride particles developing in iron-based alloys upon nitriding are coherent with the matrix and can diffract coherently with the matrix. Therefore, the dilatations of matrix and precipitates contribute to the diffraction-line shifts [12, 14]. The microstructure of tiny, coherent precipitates in a matrix is usually referred to as *continuously precipitated* (CP) (see, e.g., Ref. [15, 16]), and the same term is used in the following to refer to the corresponding diffraction patterns.

The elastic expansion of the assembly as well as the large precipitate/matrix interfacial area associated with the nanosized platelets represent a state of elevated energy [17]. As is well known, coarsening of the microstructure, involving reduction of the interface area and loss of coherency, is a means of nature to reduce the energy of the system [18]. The enhancement of strain energy by growth of the precipitates is (partly) relaxed by the introduction of misfit dislocations, i.e. plastic misfit accommodation occurs [19, 20] (see also HR-TEM micrographs of the interfaces of aged nitrides in the Fe-V system in [21] and the formation of dislocation loops encircling the growing precipitate particles [22, 23]). As a result, remaining lattice strain is significant only in the immediate vicinity of the precipitate/matrix interface, i.e. the long-range strain has vanished. The above process of

coarsening will be referred to as *continuous coarsening* (CC) as it occurs gradually throughout the entire microstructure.

Coarsening of the initial tiny, coherent precipitates in a matrix can also be realized by *discontinuous coarsening* (DC), i.e. a cellular transformation starting at a mobile interface/grain boundary, also involving relaxation of the precipitation-induced misfit strains [18, 24-26]. As a result, a lamellar microstructure develops composed of alternate lamellae of precipitate and matrix with an incoherent interface [16, 21, 27]. Next to (ongoing) continuous coarsening, such discontinuous coarsening has been observed in a number of nitrided iron-based alloys: Fe-Cr [27-30], Fe-V [31], Fe-Mo [32] and Fe-Cr-Mo[2] [33].

For the study of diffraction effects corresponding with CC and DC, in this work nitrided Fe-Cr alloys were chosen as a model system for two reasons. Firstly, the finely distributed nitride precipitates present in the initial CP microstructure diffract coherently with the ferrite matrix, which leads to large peak shifts in XRD patterns. Secondly, upon aging (i.e. continued annealing at the nitriding temperature) Fe-Cr alloys with a Cr content below 2 at.% show only minimal DC, whereas alloys with higher Cr content fully transform according to DC [27-30]. Thus, by varying the Cr-content, the diffraction consequences of CC and DC can be revealed and analyzed.

Nitriding processes usually result in a *heterogeneous* microstructure: a nitrided surface adjacent region (case) with the unnitrided matrix (core) underneath [15]. Consequently a state of residual stress, exhibiting strong and varying stress-depth gradients [34], prevails in the nitrided specimen. Residual stresses contribute to diffraction-line shift and broadening. This explains why diffraction-line shifts and broadenings due to CC and DC in the nitrided, surface-adjacent part of such specimens cannot be identified from XRD measurements performed on such specimens.
To remedy this problem, in the present study, *homogeneously* nitrided thin foils have been employed: no stress-depth and no composition-depth profiles occur in these specimens, so that diffraction-line shifts and broadenings due to CC and DC can be exposed separately for the first time.

4.2. Experimental Procedures

4.2.1. Specimen preparation

Fe-2.0 at.%Cr and Fe-4.5 at.%Cr alloys were prepared by melting, in an Al_2O_3 crucible, pure Fe (99.98 wt.%) and pure Cr (99.999 wt.%) in an inductive furnace under a protective argon atmosphere (99.999 vol.%). The casts have a cylindrical shape with a diameter of 10 mm and a length of 100 mm.

[2] Note that in both Fe-Mo and Fe-Cr-Mo alloys actually a discontinuous *precipitation* (DP) reaction, from the cubic CP-nitride to the hexagonal DP-nitride, occurs. Still, as in the case of a DC reaction, the DP reaction is associated with (full) misfit-strain relaxation in the DP regions, leading to the same effects in the XRD patterns as for a DC reaction.

The composition of the cast Fe-Cr alloys was determined by chemical analysis; the results have been gathered in Table 1 in [12].

The cast Fe-Cr alloys were cold-rolled to sheets with a thickness of 1 mm. The obtained sheets were annealed for 2 h at 700 °C in flowing H_2 atmosphere to get a recrystallized grain structure and further cold-rolled to foils with a thickness of 0.2 mm. Rectangular pieces of lateral dimensions of approx. 10 mm × 10 mm were cut from the foil and were ground to a thickness of less than 100 µm. Subsequently, the specimens were annealed at 700 °C for 2 h under H_2 atmosphere to obtain a recrystallized grain structure. Before nitriding, the thin foils were polished (last step: 1 µm diamond suspension) and cleaned with ethanol.

4.2.2. Nitriding experiments

For nitriding, the Fe-Cr thin foils were suspended with a quartz fiber in a vertical quartz tube furnace. The furnace has a temperature accuracy of ±1 K. Nitriding was performed in an ammonia/hydrogen gas flux (purity: H_2: 99.999 vol. %, NH_3: >99.998 vol. %), with the flow rates adjusted to obtain a nitriding potential of 0.1 $atm^{-½}$ [15]. Fe- 2.0 at.% Cr thin foils were saturated with nitrogen by nitriding for 1 h at 580°C and further nitrided at this temperature, which in this saturated stage implies aging of the nitrided microstructure[3], for increasing time steps up to a total of 385 h. Similarly, the Fe- 4.5 at.% Cr thin foils were saturated with nitrogen by nitriding for 135 min at 500 °C and further nitrided/aged at this temperature for different times up to a total of 300 min. After this treatment, the alloy was further aged under the same conditions for another 72 h (78 h total). The nitriding conditions had been chosen such that only a diffusion zone (ferrite with dissolved N and alloying element nitride particles) develops, i.e. other Fe-N phases such as iron-nitrides and Fe-N austenite do not develop [35]. After the nitriding and aging treatment, the specimens were lifted into the cold zone of the furnace to allow slow cooling of the specimens to room temperature.

4.2.3. Specimen characterization

4.2.3.1. Weight measurement

In order to determine the amount of N lost or taken up by the specimens, thin foils were weighed before nitriding and after each nitriding/aging step using a Mettler Toledo UMX2 microbalance with an accuracy of ±1 µg.

[3] During this effective aging treatment, the nitriding conditions were maintained in order to avoid the possible dissolution of nitrides and the escape of nitrogen from the specimens.

4.2.3.2. Light microscopy (LM)

For metallographic investigations, cross-sections of nitrided specimens were prepared by cutting pieces from the specimen with a diamond wire saw. Each cross-section was ground and polished (final polishing step: 1 µm diamond suspension) and etched with 1 % Nital (1 vol.% HNO_3 in ethanol) at room temperature for about 10 s for Fe-2.0 at.%Cr thin foils and 30 s for Fe-4.5 at.%Cr thin foils. LM micrographs were taken using a Zeiss Axiophot microscope equipped with a digital camera (Olympus ColorView IIIu).

4.2.3.3. X-ray diffraction (XRD) analysis

XRD patterns were recorded from the surface of unnitrided, and nitrided/aged Fe-Cr thin foils using a PANalytical X'Pert diffractometer in Bragg-Brentano configuration equipped with a Co tube and a graphite monochromator in the diffracted beam to select Co-Kα radiation. The diffraction-angle range of 30°-110° 2θ was scanned with a step size of 0.009° 2θ. The XRD patterns thus recorded were evaluated using the TOPAS software (Version 4.2, Bruker AXS). Each diffractogram recorded with Co-Kα radiation is composed of both Co-$K\alpha_1$ and Co-$K\alpha_2$ components [36]. In the case of the Fe-2.0 at.% Cr specimen, the structural broadening of each of the components was fitted by three pseudo-Voigt (pV) functions (for details see section 4.3.1). For the Fe-4.5 at.%Cr alloy for nitriding/aging times up to 150 min, the structural broadening of each component was also fitted by three pV-functions. For longer nitriding/aging times of this alloy, fitting was performed with only two pV-functions for each component (for details see section 4.3.2). The instrumental profile was obtained from a measured standard LaB_6 powder diffraction pattern. This instrumental broadening was incorporated into the fitting of the measured diffraction profiles by convolution with the pV-functions describing the specimen (structural) broadening. The lattice-spacing/lattice-parameter data given in this paper pertain to the diffraction profiles without instrumental broadening.

4.2.3.4. Transmission electron microscopy (TEM) analysis

Electron transparent foils for TEM investigations were prepared by cutting a small piece from the nitrided Fe-2.0 at.%Cr foils with a diamond wire saw followed by fixing it onto a copper ring and final thinning of the fixed thin foil by Ar-ion milling (3 kV, 8° ion angle of incidence, approx. 2 h, liq.-N2 cooling). A Philips CM 200 TEM operating at an acceleration voltage of 200 kV was used.

4.3. Results

4.3.1. Fe-2.0 at.%Cr alloy

A comparison of the fitted and measured 211 diffraction profile of nitrided and aged Fe-2.0 at.%Cr alloy (36 h at 580 °C) is provided by Figure **4-1** The specimen is in an intermediate stage of aging, such that contributions of CP-ferrite (at lower diffraction angles) and of the emerging CC-ferrite (at higher diffraction angles) are clearly present in the profile (for a detailed discussion see section 4.4.2). The results obtained by evaluation of other ferrite reflections of the Fe-2.0 at.%Cr specimen are in agreement with those obtained by evaluation of the 211 reflection. Due to the larger peak separation at higher diffraction angles, only the results of the 211 reflection are presented. Fitting of the structural broadening in the diffraction patterns with a single (symmetric or asymmetric) pV-function is not possible; three (symmetric) pV-functions are required for each $Co_{K\alpha}$-component of the radiation. For the aged specimens these functions can be assigned to the main peak of CP ferrite, its tail towards higher diffraction angles (cf. Ref. [12]), and the peak of CC ferrite. The contribution of the first two functions decreases and the contribution of the third function increases with increasing aging time. Up to an aging time of 247 h, the position of the main, CP peak can be reliably determined with the described fitting procedure as it is manifested as either a separate peak or a clear shoulder (see error bars in Figure **4-3**).

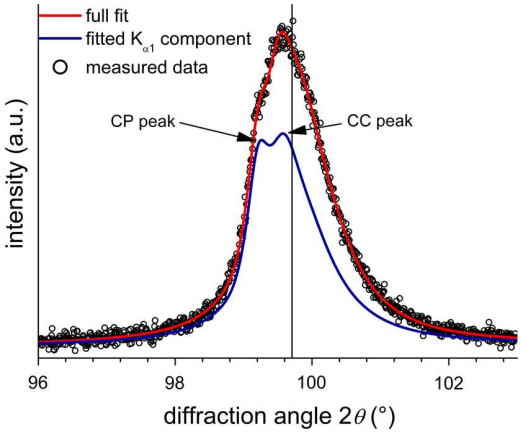

Figure 4-1. Comparison of the measured 211 diffraction profile (Co-Kα radiation) of an Fe-2.0 at.%Cr specimen, nitrided at 580°C for 36 h with a nitriding potential of 0.1 $atm^{-½}$, with the corresponding $K_{\alpha 1}$+$K_{\alpha 2}$ fit, and the fitted $K_{\alpha 1}$-component (see section 4.2.3.3). The $K_{\alpha 1}$-peak position for pure, unstrained ferrite (α-Fe) has been indicated by a vertical line. The specimen is in an intermediate state of aging; both a CP and a CC peak are present in the diffractogram, as indicated by arrows (cf. evolution of ferrite peaks in Figure 4-2).

The evolution of the ferrite reflections, exemplarily presented for the 211 reflection, upon further nitriding (i.e. aging, cf. above discussion and section 4.2.2) at 580 °C reveals two processes (see Figure **4-2**): i) the main CP peak shifts (back) towards higher diffraction angles (see also Figure **4-3**) and its integrated intensity decreases with increasing treatment time until it has fully vanished at the finally observed stage after 385 h, and ii) a separate peak showing considerable broadening (as compared to the main CP peak) develops centered at approximately the position of pure, unstrained

α-Fe (Figure **4-2**). This second peak subsequently increases in integrated intensity and begins to sharpen upon continued nitriding (=aging).

The maximum initial shift of the ferrite (XRD) reflections towards lower diffraction angles (Figure 4-2), and correspondingly the largest ferrite-matrix lattice expansion (Figure 4-3), i.e. just after full saturation of the Fe-2.0 at.%Cr specimen with N (i.e. precipitation of all Cr as CrN, c.f. Figure **4-5** in [12]) was observed after 1 h of nitriding at 580 °C with a nitriding potential of 0.1 $atm^{-½}$ (see also discussion in section 4.4.1). This implies that nitriding times longer than 1 h can be considered as aging times.

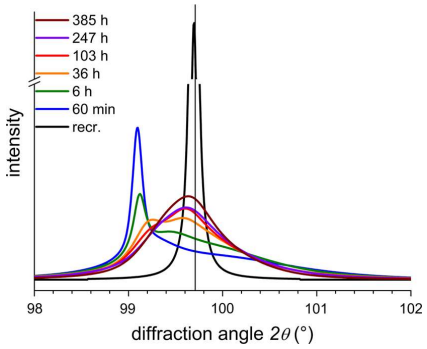

Figure 4-2. Evolution of the $CoK_{\alpha 1}$-211 ferrite–matrix reflection, recorded from the surfaces of Fe-2.0 at.%Cr thin foils homogeneously nitrided at 580 °C with a nitriding potential of 0.1 $atm^{-½}$, for the nitriding/aging times indicated in the figure. The $K\alpha_1$-peak position for pure, unstrained ferrite (α-Fe) has been indicated by a vertical line. The profiles were normalized with respect to their integrated intensity.

The light optical micrograph taken from the cross section of the specimen after the final stage of nitriding/aging is shown in Figure **4-4**. No indication of an extended DC reaction (which would lead to more pronounced etching contrast) is observed; only very few regions close to a grain boundary may have transformed according to DC. It is concluded that the above described changes in the XRD pattern pertain to the CC process.

TEM analysis was performed on the specimen after 1 h of nitriding at 580 °C, i.e shortly after all Cr has precipitated as CrN, as validated by no further weight gain of the specimen. At this stage, the maximum peak shift of the ferrite reflection towards lower diffraction angles has occurred (see Figure **4-3**). In this initial state, i.e. before distinct coarsening, extremely fine, coherent precipitates (platelets of approx. 5 nm diameter and less than 1 nm thickness) are present (see bright- and dark-field micrographs in Figure **4-5**(a)). After pronounced aging, i.e. after 385 h of nitriding/aging at 580 °C, when only a relatively broad peak remains in the XRD pattern at the position of pure, unstrained α-Fe, the precipitates have grown considerably in diameter (to approx. 50 nm, see Figure **4-5**(b)) and have lost their coherency with the matrix (note the disappearance of the intensity streak through the

200-type reflections (as observed for the nitrided state; Figure **4-5**(a)) and the appearance of distinct CrN spots in the selected area diffraction pattern (SADP) (Figure **4-5**(b)).

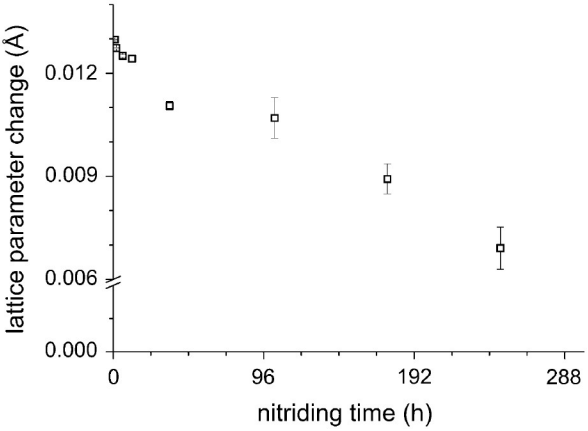

Figure 4-3. Evolution of the lattice-parameter change, as compared to the lattice-parameter of pure, unstrained α-Fe, determined from the 211 ferrite, CP main peak position (after 103 h the peak is present as a shoulder, cf. Fig. 2) of Fe-2.0 at.%Cr alloy, nitrided/aged at 580 °C with a nitriding potential of 0.1 $atm^{-½}$, as function of nitriding/aging time. After a total of 247 h of aging, the shoulder due to the main, CP peak becomes indistinguishable/vanishes in the measured diffraction profiles (see text in section 4.3.1).

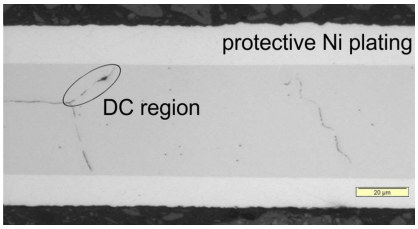

Figure 4-4. Light optical micrograph taken from the cross-section of a Fe-2.0 at.%Cr thin foil after nitriding for 385 h at 580 °C with a nitriding potential of 0.1 $atm^{-½}$. Only minor DC regions occur along the grain boundaries.

4.3.2. Fe-4.5 at.%Cr alloy

A comparison of the fitted and measured diffraction patterns of nitrided and aged Fe-4.5 at.% Cr alloy is provided by Figure **4-6**. The specimen is in an initial stage of aging, such that contributions of CP ferrite (at lower diffraction angles) and DC ferrite (at higher diffraction angles) are clearly

present in the profile (for a detailed discussion see section 4.4.3). The results obtained by evaluation of other ferrite reflections of the Fe-4.5 at.%Cr specimen are in agreement with those obtained by evaluation of the 211 reflection. Due to the larger peak separation at higher diffraction angles (and to allow for direct comparison with results shown for the Fe-2.0 at.%Cr alloy in Figure **4-2**), only the results of the 211 reflection are presented. Up to an aging time of 150 min., the structural broadening of each $Co_{K\alpha}$-component was fitted with three pV-functions, as for the Fe-2.0 at.%Cr alloy: for the aged specimens these functions can be assigned to the main peak of CP ferrite, its tail towards higher diffraction angles (cf. Ref. [12]), and the peak of DC ferrite. For longer aging times, two pV-functions for the structural broadening of each component sufficed for a successful fitting: the influence of the tail of the CP microstructure had vanished. The occurrence of a distinct diffraction peak of the DC ferrite, more outspoken than the CC ferrite peak in case of the Fe-2.0 at.%Cr alloy (compare Figure **4-2** and Figure **4-7**), allows for (much) better determination of all peak parameters and thus quantitative peak data are presented for both the CP main peak and the DC peak in the following.

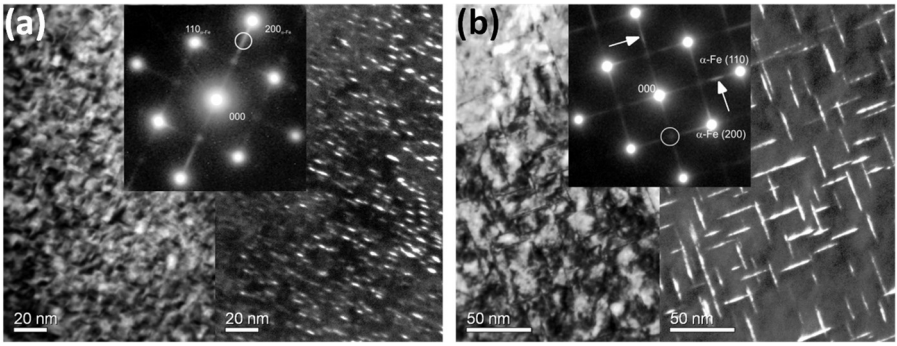

Figure 4-5. a) TEM bright field micrograph (left) with $[001]_{\alpha\text{-Fe}}$ zone axis, SADP (inset), and dark field micrograph (right) of a Fe-2.0 at.%Cr specimen homogeneously nitrided at 580 °C for 1 h with a nitriding potential of 0.1 $atm^{-½}$. The bright and dark field micrographs show the formation of platelets along $<100>_{\alpha\text{-Fe}}$ directions. The SADP (inset) is compatible with nitride platelets of NaCl-type crystal structure exhibiting a Baker-Nutting orientation-relationship with the ferrite matrix [48]. The aperture for the DF image shown at the right-hand side of a) has been indicated by a white circle in the SADP and was positioned on the streak through the $200_{\alpha\text{-Fe}}$ spot originating from one variant of the CrN precipitate platelets. b) TEM bright field micrograph (left) with $[001]_{\alpha\text{-Fe}}$ zone axis, SADP (inset), and dark field micrograph (right) of Fe-2.0 at.%Cr specimen nitrided at 580 °C for 385 h (i.e. *aged*) with a nitriding potential of 0.1 $atm^{-½}$. The aperture for the DF image has been indicated by a white circle in the SADP and was positioned on the intersection of the streaks originating from two variants of the CrN precipitates. The white arrows in the SADP indicate the position of intensity maxima along the streak which correspond to the 200_{CrN}-type spots.

The maximum initial shift of the ferrite main-peak (Figure **4-7**), and correspondingly the largest ferrite matrix-lattice expansion (Figure **4-8**), occurs (just) after full saturation of the Fe-4.5 at.%Cr

specimen with N, i.e. after nitriding for 135 min at 500°C with a nitriding potential of 0.1 $atm^{-½}$ (see also discussion in section 4.4.1).

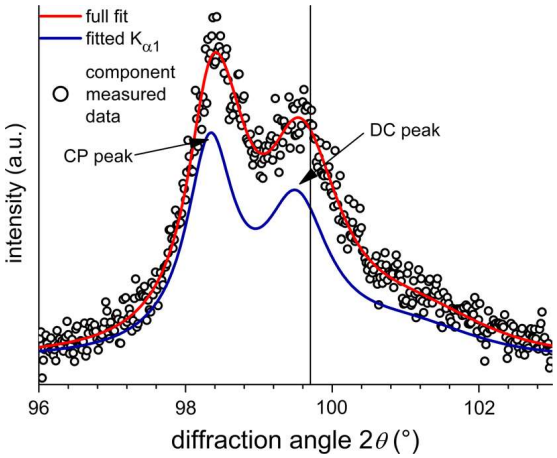

Figure 4-6. Comparison of the measured 211 diffraction profile (Co-Kα radiation) of an Fe-4.5 at.%Cr specimen, nitrided at 500°C for 135 min with a nitriding potential of 0.1 $atm^{-½}$, with the corresponding $K_{\alpha 1}$+$K_{\alpha 2}$ fit, and the fitted $K_{\alpha 1}$-component (see section 4.2.3.3). The $K\alpha_1$-peak position for pure, unstrained ferrite (α-Fe) has been indicated by a vertical line. The specimen is in an initial state of aging; both a CP and a DC peak are present in the diffractogram, as indicated by arrows (cf. evolution of ferrite peaks in Fig. 7). The larger noise in the measured data points as compared to the Fe-2.0 at.% Cr specimen (Fig. 1) is a result of the more textured nature of the Fe-4.5 at.%Cr specimen implying a lower intensity of the 211 ferrite reflection.

The evolution of the 211 ferrite reflection upon further nitriding (i.e. aging) is shown as a function of nitriding time (i.e. aging) in Figure **4-7**. Two processes are discerned: i) the CP-main peak shifts (back) towards higher diffraction angles (see also Figure **4-8**) and its integrated intensity decreases with increasing treatment time until it has vanished at the finally observed stage after 300 min (see Figure **4-9**), and ii) the second peak at higher diffraction angle, centered at approximately the position of pure, unstrained α-Fe, increases in integrated intensity with increasing treatment time. Unlike the second peak present in the diffraction patterns of the nitrided and aged Fe-2.0 at.%Cr thin foils (Figure **4-2**) that is considerably broadened as compared to the main CP-peak, the second peak developing in the diffraction patterns of nitrided Fe-4.5 at.%Cr thin foils is relatively sharp (similar to the main CP-peak), from its initial appearance in the early stages of nitriding/coarsening, and shows only little change in broadening upon continued treatment.

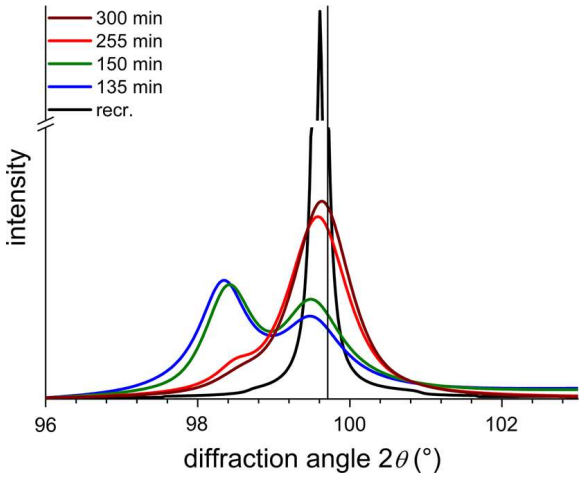

Figure 4-7. Evolution of the $CoK_{\alpha 1}$-211 ferrite-matrix reflection, recorded from the surfaces of Fe-4.5 at.%Cr thin foils homogeneously nitrided at 500 °C with a nitriding potential of 0.1 $atm^{-½}$ for the nitriding times indicated in the figure. The $K\alpha_1$-peak position for pure, unstrained ferrite (α-Fe) has been indicated by a vertical line. The profiles were normalized with respect to their integrated intensity.

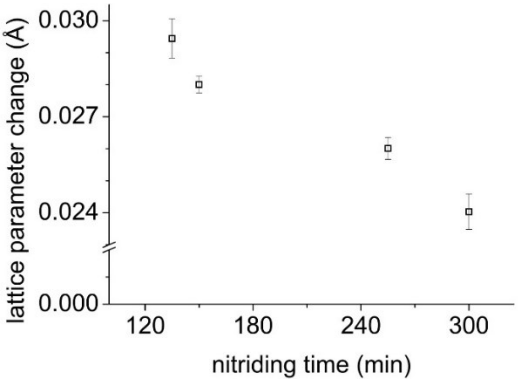

Figure 4-8. Evolution of the lattice-parameter change as compared to the lattice-parameter of pure, unstrained α-Fe, determined from the 211 ferrite peak position of the CP main peak (later times present as a shoulder, cf. Fig. 7) of Fe-4.5 at.%Cr alloy, nitrided/aged at 500 °C with a nitriding potential of 0.1 $atm^{-½}$ as function of nitriding/aging time.

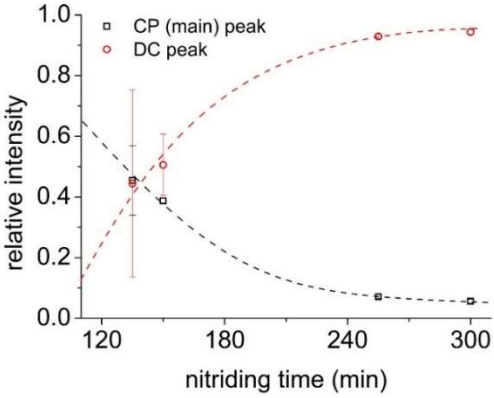

Figure 4-9. Evolution of the relative intensities of the CP main peak and the DC peak determined from the 211 ferrite reflections of Fe-4.5 at.%Cr alloy, nitrided/aged at 500 °C with a nitriding potential of 0.1 $atm^{-½}$, as function of nitriding/aging time. Lines are drawn to guide the eye.

Corresponding light optical micrographs taken from cross sections prepared from the Fe-4.5 at.%Cr specimen after each nitriding step (Figure **4-10**) demonstrate the development of DC regions throughout the microstructure (note that already after 135 min., due to the large driving force for DC in this alloy, already a partial DC has occurred); the DC continues until the whole specimen has transformed to DC (see the microstructure as observed after 225 min in Figure **4-10**). It is concluded that the above described changes in the XRD patters pertain to the DC process. After prolonged aging for another 72 h at 500°C with a nitriding potential of 0.1 $atm^{-½}$ to a total nitriding/aging time of 78 h, separate CrN reflections could be identified in the XRD pattern (see Figure **4-11**).

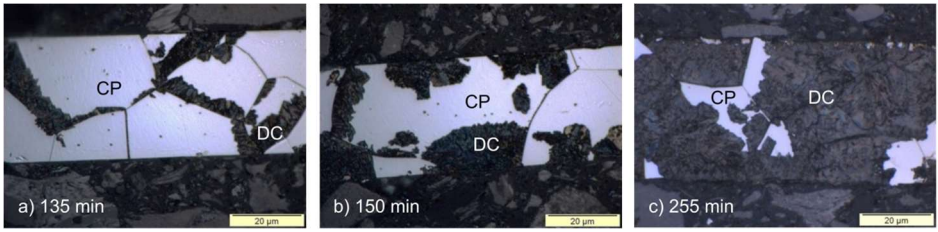

Figure 4-10. Light optical micrographs taken from the cross-sections of a Fe-4.5 at.%Cr thin foil specimens after nitriding at 580 °C with a nitriding potential of 0.1 $atm^{-½}$ for the indicated nitriding (aging) times. The coarse lamellar DC microstructure is more prone to etchant attack, due to a large amount of incoherent interfaces, and thus shows a more pronounced etching contrast as compared to CP regions. Development of the DC regions within the diffracting volume of the specimen after nitriding for longer times is compatible with the gradual rise of a new ferrite reflection from the DC region and gradual disappearance of the ferrite reflection from the CP region (see Figure **4-7**).

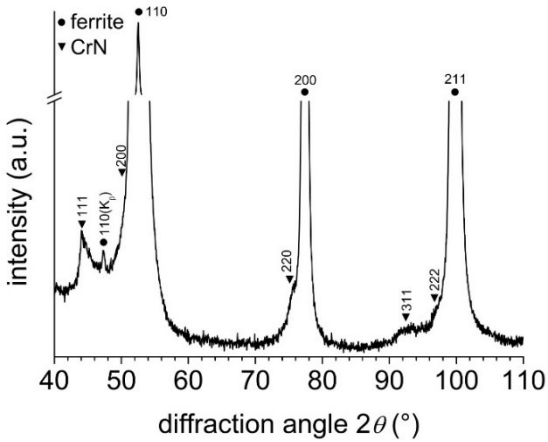

Figure 4-11. Diffractogram (CoK_α radiation) recorded from the surface of an Fe-4.5 at.%Cr thin foil homogeneously nitrided at 500 °C with a nitriding potential of 0.1 $atm^{-½}$ for 78 h. The separate (see text in section 4.4.3) reflections of the ferrite matrix and the CrN precipitates have been indicated.

4.4. Discussion

4.4.1. Initial state

Before nitriding, the Fe-2.0 at.%Cr and Fe-4.5 at.%Cr alloys are single phase solid solutions of Cr in α-Fe. The substitutionally dissolved Cr atoms, that are slightly larger than the Fe atoms, induce an expansion of the ferrite lattice and thus a larger lattice parameter as compared to pure, unstrained α-Fe [37]; cf. the diffraction-peak positions of the Fe-Cr solid solution specimens (indicated as recr.) and of the pure α-Fe specimens (vertical line) (Figure **4-2** and Figure **4-7**).

Upon nitriding of the Fe-2.0 at.%Cr and Fe-4.5 at.%Cr specimens the volume misfit between the ferrite matrix and the initially developing finely distributed, coherent nitride precipitates is accommodated fully elastically. In this condition, the ferrite matrix and the coherent nitride precipitates *diffract coherently* [12, 14, 18]; i.e. the observed ferrite reflections represent coherent diffraction by the whole assembly. The magnitude of the misfit-induced expansion of the assembly, and thus of the corresponding peak shift of the ferrite reflections towards lower diffraction angles, as compared to the unnitrided condition, depends on the volume fraction of precipitates, the precipitate/matrix (volume) misfit and the elastic properties of matrix and precipitates. Adopting the procedure given in Ref. [12], the thus predicted 211 lattice-plane spacing changes, Δd_{CrN}, for the specimens of the current study in this initial state (i.e. directly after homogeneous nitrogen saturation of the specimens; this is the state of the Fe-2.0 at.%Cr thin foil after 60 min of nitriding at 580 °C

(Figure **4-2**) and of the CP microstructure in the Fe-4.5 at.%Cr thin foil after 135 min of nitriding at 500 °C (Figure **4-7**) can be compared with the 211 lattice-plane spacing changes determined from the measured peak positions in Table **4-1**.

Table 4-1. Measured and predicted change of the lattice spacing of the {211} lattice planes of the ferrite matrix in fully nitrided Fe-2.0 at.%Cr (580 °C, 1 h, 0.1 atm$^{-½}$) and fully nitrided Fe-4.5 at.%Cr (500 °C, 135 min, 0.1 atm$^{-½}$) alloys: Δd_{CrN} is the calculated {211} lattice-plane spacing change of the ferrite matrix due to CrN precipitation [12], $\Delta d_{\text{dissolved N}}$ corresponds to the calculated {211} lattice-plane spacing change of the ferrite matrix due to an equilibrium amount of dissolved N in ferrite under the present nitriding conditions [46, 47] and $\Delta d_{\text{measured}}$ corresponds to the measured lattice-plane spacing change of the {211} lattice planes of the ferrite matrix.

Alloy	Δd_{CrN} [Å]	$\Delta d_{\text{dissolved N}}$ [Å]	$\Delta d_{\text{total}} = \Delta d_{CrN} + \Delta d_{\text{dissolved N}}$ [Å]	$\Delta d_{\text{measured}}$ [Å]
Fe-2.0 at.%Cr	0.0047	0.0009	0.0056	0.0053
Fe-4.5 at.%Cr	0.0105	0.0003	0.0108	0.0120

A full comparison of measured and predicted lattice-parameter changes (diffraction-peak shifts) requires recognizing the following contributions to the lattice-parameter change:

i): The ferrite lattice contracts by the depletion of Cr from the solid solution during CrN precipitation: the {211} lattice-plane spacing changes Δd_{CrN} in Table **4-1** (due to elastic misfit accommodation; see above) have been given relative to pure α-Fe.

The following (minor) contributions occur, but have not been quantified:

ii): As the current specimens were not denitrided, an additional dilatation due to (equilibrium and excess) N dissolved in the ferrite matrix (for details about excess N see e.g. Ref. [11]) can occur for the specimens (as observed after cooling to room temperature). In Table **4-1**, the effect on the {211} lattice-plane spacing by dissolution of the equilibrium amount of N in ferrite ($\Delta d_{\text{dissolved N}}$) has been given. For the Fe-2.0 at.%Cr specimen, the measured peak shift ($\Delta d_{\text{measured}}$) is a little smaller than would be expected taking into account the dilatation both by CrN precipitation and by dissolution of the equilibrium amount of N in ferrite (Δd_{total}). This suggests that due to the relatively high nitriding temperature of 580 °C, already after 1 h of nitriding some relaxation has occurred (i.e. the precipitation-induced misfit is only partially elastically accommodated). On the other hand, the Fe-4.5 at.%Cr specimen was nitrided at the relatively low temperature of 500 °C, and thus, less relaxation is expected. Indeed, the measured peak shift ($\Delta d_{\text{measured}}$) for this specimen is (even) larger than would be expected taking into account the dilatation both by CrN precipitation and by dissolution of the equilibrium amount of N in ferrite (Δd_{total}). This additional peak shift is likely due to the presence of excess N as indicated in [11].

iii): Precipitation of α"-$Fe_{16}N_2$ from dissolved N will occur from N-supersaturated ferrite at room temperature (see e.g. Ref. [38-40]). This additional precipitation process at room temperature will also lead to additional line shifts and broadening changes [41-43]. However, the misfit between ferrite and

α"-$Fe_{16}N_2$ is considerably smaller ($\varepsilon_V = 0.0300$ (lattice parameters of α"-$Fe_{16}N_2$ from Ref. [39])) than the misfit between ferrite and CrN ($\varepsilon_V = 0.1464$ [12]) and thus its influence on the measured lattice-parameter change is minimal.

iv): An additional misfit between CrN and ferrite results from the differences in thermal expansion coefficient of CrN precipitates and ferrite matrix ($\varepsilon_T = 0.0065$ for cooling from 580 °C to 25 °C). Also this contribution to the lattice-parameter change can be neglected compared to the magnitude of the elastically accommodated volume misfit present after full initial precipitation of CrN in the alloys (see above).

In addition to the observed peak shifts due to elastic precipitate/matrix misfit accommodation, the asymmetric tail of the main reflection (towards higher diffraction angles) represents the severely distorted nature of the regions in the vicinity of the precipitates [12, 44, 45].

4.4.2. Continuous Coarsening

The nitride precipitates in the Fe-2.0 at.%Cr alloy upon annealing show considerable growth in length from the initially, fully coherent state to the incoherent state, as evidenced by TEM (cf. Figure **4-5**(a) and (b)). The coarsening process is accompanied by a loss of elastic accommodation of the precipitate/matrix (volume) misfit and thereby the overall, long-range, elastic lattice expansion decreases (Figure **4-3**). This is accompanied by a "back"-shifting of the CP ferrite main peak towards the unstrained position as revealed in Figure **4-2**. Cr stays depleted from the ferrite matrix and thus does not contribute further to the peak shift as a function of aging time. Other (subordinate) causes of peak shift as a function of aging time are the following (cf. discussion in section 4.4.1):

i): During relaxation of the precipitate/matrix volume misfit and the coarsening of the nitride platelets (reduction in interfacial area) the amount of excess N in the alloy decreases (desorption) and thus its (already minor) contribution to the peak shift decreases with increasing annealing time.

ii): The thus decreased amount of dissolved N with increased annealing time can lead to a decreased development of α"-$Fe_{16}N_2$ precipitates at room temperature. Also this (already minor) contribution to the peak shift decreases with increasing annealing time.

iii): The minor contribution of the thermal misfit does not change. Its corresponding peak shift thus remains minimal (see section 4.4.1).

In an end stage of coarsening and apart from the immediate vicinity of the precipitates, the misfit will be (nearly) fully relaxed and thus the ferrite matrix shows a lattice spacing close to that of pure ferrite. Therefore, the emerging CC-peak develops at the approximate position of pure α-Fe. However, the heterogeneity of the relaxation process and its locally varying degree of completion involve the presence of a pronounced amount of microstrain and thus the occurrence of an appreciable amount of diffraction-line broadening as exhibited by the CC-peak. Obviously, upon increasing (aging) time, the strain variation decreases leading to a sharpening of the corresponding reflection (Figure **4-2**).

The developing incoherency of the precipitate/matrix interface randomizes the phase relation of X-rays scattered by the matrix and those by the precipitates and thus incoherent diffraction of matrix and precipitates now occurs [14, 18]. Indeed, the TEM SADP in Figure **4-5**(b) now reveals separate diffraction spots from matrix and precipitates. In the XRD patterns, individual precipitate reflections cannot be observed due to the low volume fraction.

4.4.3. Discontinuous Coarsening

If the alloy contains sufficient alloying element and if the misfit and the amount of precipitate/matrix interfacial area is high enough, then *discontinuous coarsening* is favored over the (usual) continuous coarsening. Indeed DC governs the coarsening process in the nitrided Fe-4.5 at.%Cr alloy (see Figure **4-10**). The overall DC reaction in the nitrided Fe-4.5 at.%Cr specimen can be expressed as (see Refs. [24, 26, 27]):

$$(\alpha' + \beta')_{\text{fine CP}} \rightarrow (\alpha + \beta)_{\text{coarse DC lamellae}}$$

where, α' denotes the strained, N-supersaturated ferrite matrix, β' the strained, coherent CrN precipitates, α the relaxed ferrite lamellae without supersaturation and β the relaxed, coarse incoherent CrN precipitate lamellae. The energy difference of the continuously precipitated and discontinuously coarsened states, i.e. the driving force for DC, for the present specimens is comprised of three contributions [27]; reduction of the interfacial area (reduction of interfacial energy), the loss of ferrite matrix (nitrogen) supersaturation (i.e. loss of excess N; reduction in chemical energy), and the relaxation of the long-range strain-fields due to the coherent to incoherent transition (release of strain energy).

Actually, in specimens where DC can occur, both continuous and discontinuous coarsening take place simultaneously but with different reaction rates [21, 28-30]: The DC reaction can be rate controlled by diffusion of the atoms along the mobile grain boundary that sweeps through the specimen and in the wake of which the cellular microstructure develops, whereas the CC reaction is governed by volume diffusion processes, necessary for the growth and dissolution of precipitates. Consequently, the rate of the DC reaction is (much) higher than that of the CC reaction. Indeed, whereas an end stage of CC at 580 °C is reached after hundreds of hours, a final state of DC at 500 °C is reached after hundreds of minutes (cf. Figure **4-2** and Figure **4-7**). Therefore, in addition to the development of relatively slowly relaxing and thus only partly relaxed regions surrounding the continuously coarsened precipitates, in advance of the reaction front of the DC reaction, fully relaxed matrix regions (ferrite lamellae) occur behind the DC reaction front. Thus, in a specimen that undergoes DC, in principle two types of ferrite regions contribute to the second diffraction peak at higher diffraction angle (cf. section 4.3.2): i) the continuously coarsened regions (decreasing in volume upon continued aging) corresponding with a broad peak (cf. section 4.4.2), and ii) the fully stress-relieved ferrite in the discontinuously coarsened part (increasing in volume upon aging) corresponding with a sharp peak. At an end stage of aging (i.e. after 300 min of aging at 500 °C) the contribution of continuously coarsened regions has become minimal (cf. Figure **4-10**). Then, the

emerging second peak is dominated by the discontinuously coarsened ferrite and is therefore sharp. Also, due to the presence of a clear boundary (see Refs. [29, 30]) between the ferrite in the continuously coarsened region and the ferrite in the discontinuously coarsened regions, both will always diffract *incoherently*. For the DC microstructure, i.e. with incoherently diffracting precipitates of relatively large dimensions, separate precipitate reflections of CrN and (DC-) ferrite matrix occur (see Figure **4-11**).

4.5. Conclusions

The interpretation of the behavior of the (X-ray) diffraction peaks recorded from ferrite in nitrided Fe-Me alloys (Me forms misfitting, coherent precipitates of MeN in early stages of nitriding), from the initial, fully continuously precipitated state to the continuously or discontinuously coarsened state, can be summarized as follows (see also schematic in Figure **4-12**):

In the initial, just fully nitrided state, the ferrite reflections have shifted towards lower diffraction angles as a result of the *elastic* accommodation of the precipitate-matrix misfit. The assembly of matrix and precipitate particles diffracts coherently. The magnitude of the CP-peak shift can be quantitatively predicted from the amount of precipitates and the degree of misfit. Additionally, the severely distorted regions surrounding the precipitates lead to a tail of the peaks towards higher diffraction angles.

Upon aging, coarsening of the initially coherent precipitates can occur in two distinctly different ways: continuous coarsening and discontinuous coarsening. Both processes can occur simultaneously. The higher the alloying element/precipitate content, the larger the contribution of the discontinuous coarsening.

Upon continuous coarsening the average precipitate-particle size increases under gradual loss of the coherency with the matrix, involving the development of a heterogeneous state of strain relaxation in the matrix: the CP-matrix diffraction maximum gradually shifts (back) towards higher diffraction angles due to the loss of the long-range matrix dilatation; the CC-reflection is strongly broadened due to the spatially varying state of relaxation/remaining lattice strain of the individual precipitates. As the volume fraction of the fully relaxed regions increases upon prolonged aging, the broadening of the CC-reflection decreases and its relative intensity increases upon approaching the fully coarsened state, when precipitates and matrix diffract incoherently.

Upon discontinuous coarsening, the matrix at the reaction front abruptly changes from misfit strained to fully relaxed, involving that already at the start of coarsening a sharp ferrite peak emerges at the position of pure unstrained ferrite. Upon increasing aging time, the relative intensity of this reflection increases, while that of the initially continuously precipitated and relatively very slowly continuously coarsening matrix decreases. Due to the comparatively large volume fraction of precipitates in alloys undergoing DC and the incoherent diffraction of matrix and precipitate lamellae of the relaxed DC microstructure, separate reflections of nitrides and ferrite can be detected.

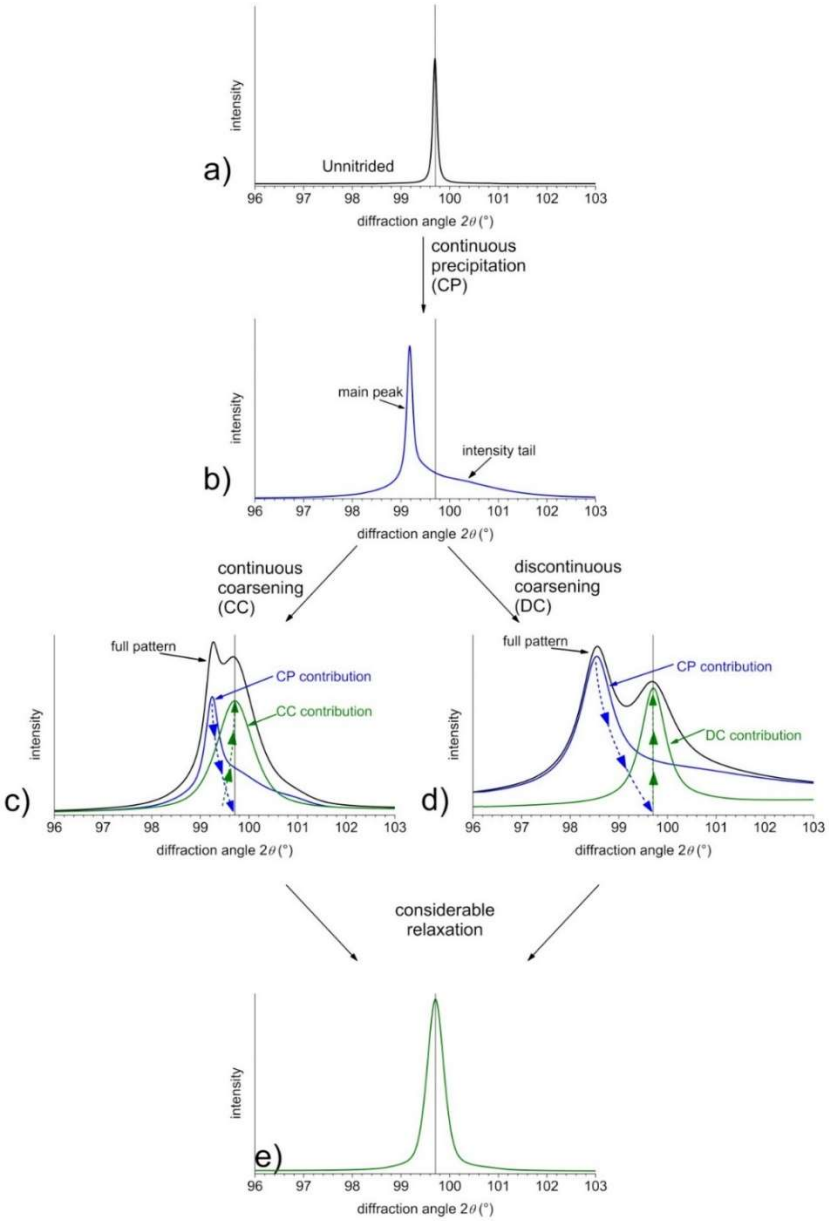
a)
Unnitrided
intensity
96 97 98 99 100 101 102 103
diffraction angle 2θ (°)
continuous precipitation (CP)
b)
main peak
intensity tail
intensity
96 97 98 99 100 101 102 103
diffraction angle 2θ (°)
continuous coarsening (CC)
discontinuous coarsening (DC)
c)
full pattern
CP contribution
CC contribution
intensity
96 97 98 99 100 101 102 103
diffraction angle 2θ (°)
d)
full pattern
CP contribution
DC contribution
intensity
96 97 98 99 100 101 102 103
diffraction angle 2θ (°)
considerable relaxation
e)
intensity
96 97 98 99 100 101 102 103
diffraction angle 2θ (°)

Figure 4-12. Schematic presentation showing the evolution of the X-ray diffractogram of Fe-Me alloys upon nitriding and subsequent continuous and discontinuous coarsening, see section 4.5 for details. In all the diffractograms, the position of the pure α-Fe peak has been indicated with a vertical line. Arrows in c) and d) indicate the evolution of position and intensity of component peaks, together constituting the total diffraction profile, as a function of aging time.

Acknowledgements

The authors would like to thank Dr. E. Bischoff for the TEM investigations, Mr. W.-D. Lang for preparation of the TEM specimens and Mr. P. Kress for assistance with the nitriding experiments (all with Max Planck Institute for Intelligent Systems) and Prof. A. Leineweber (now with TU Bergakademie Freiberg) for valuable discussion.

References

[1] E.J. Mittemeijer, U. Welzel. Modern diffraction methods, Wiley-VCH, Weinheim, 2013.

[2] A.J. Guinier. X-ray diffraction in crystals, imperfect crystals, and amorphous bodies, Freeman, San Francisco etc., 1963.

[3] D.J. Dyson, Institute of Materials Minerals and Mining. X-ray and electron diffraction studies in materials science, Maney, London, 2004.

[4] R.W. Cahn. Concise encyclopedia of materials characterization. 2nd ed., Elsevier, Amsterdam, 2005.

[5] M. Ladd, R. Palmer. Structure determination by x-ray crystallography analysis by x-rays and neutrons celebrating the centenary of x-ray crystallography. 5th ed., Springer Science+Business Media, New York, 2013.

[6] V. Daniel, H. Lipson. An X-ray study of the dissociation of an alloy of copper, iron nickel, Proc R Soc Lon Ser-A 181 (1943) 0368-0378.

[7] L. Zwell, A.W. Danko. Applications of X-Ray-Diffraction Methods to Quantitative Chemical-Analysis, Appl Spectrosc Rev 9 (1975) 167-221.

[8] H.M. Ledbetter, M.W. Austin. Internal Strain (Stress) in an Sic-Al Particle-Reinforced Composite - an X-Ray-Diffraction Study, Mater Sci Eng 89 (1987) 53-61.

[9] J. Luo, K. Tao, H. Yin, Y. Du. Studies on quantitative x-ray diffraction characterization of phase depth profiles, Rev Sci Instrum 67 (1996) 2859-2862.

[10] J. Epp, H. Surm, O. Kessler, T. Hirsch. In situ X-ray phase analysis and computer simulation of carbide dissolution of ball bearing steel at different austenitizing temperatures, Acta Mater 55 (2007) 5959-5967.

[11] M.A.J. Somers, R.M. Lankreijer, E.J. Mittemeijer. Excess nitrogen in the ferrite matrix of nitrided binary iron-based alloys, Philosophical Magazine A 59 (1989) 353-378.

[12] M. Akhlaghi, T. Steiner, S.R. Meka, A. Leineweber, E.J. Mittemeijer. Lattice-Parameter Change Induced by Accomodation of Precipitates/Matrix Misfit; Misfitting Nitrides in Ferrite, Acta Mater 98 (2015) 254-262.

[13] W. Tirry, D. Schryvers. Quantitative determination of strain fields around Ni4Ti3 precipitates in NiTi, Acta Mater 53 (2005) 1041-1049.

[14] J.G.M. van Berkum, R. Delhez, T.H. de Keijser, E.J. Mittemeijer. Diffraction-line broadening due to strain fields in materials; Fundamental aspects and methods of analysis, Acta Crystallogr A 52 (1996) 730-747.

[15] E.J. Mittemeijer. Fundamentals of Nitriding and Nitrocarburizing. ASM Handbook, Volume 4A, Steel Heat Treating Fundamentals and Processes, vol. 4: ASM International, 2013. p.619-646.

[16] M. Sennour, C. Jacq, C. Esnouf. Mechanical and microstructural investigations of nitrided Fe-Cr layers, J Mater Sci 39 (2004) 4533-4541.

[17] S.S. Quek, Y. Xiang, D.J. Srolovitz. Loss of interface coherency around a misfitting spherical inclusion, Acta Mater 59 (2011) 5398-5410.

[18] E.J. Mittemeijer. Fundamentals of materials science, Springer, Berlin, 2010.

[19] D.A. Porter, K.E. Easterling. Phase Transformations in Metals and Alloys, Van Nostrand Reinhold, London, 1982.

[20] J.W. Christian. The Theory of Transformations in Metals and Alloys, Pergamon Press, Oxford, 2002.

[21] N.E. Vives Díaz, S.S. Hosmani, R.E. Schacherl, E.J. Mittemeijer. Nitride precipitation and coarsening in Fe–2.23at.% V alloys: XRD and (HR)TEM study of coherent and incoherent diffraction effects caused by misfitting nitride precipitates in a ferrite matrix, Acta Mater 56 (2008) 4137-4149.

[22] S.R. Meka, E. Bischoff, B. Rheingans, E.J. Mittemeijer. Octapod-shaped, nanosized, amorphous precipitates in a crystalline ferrite matrix, Phil Mag Lett 93 (2013) 238-245.

[23] P.A. Geslin, B. Appolaire, A. Finel. Investigation of coherency loss by prismatic punching with a nonlinear elastic model, Acta Mater 71 (2014) 80-88.

[24] D.B. Williams, E.P. Butler. Grain boundary discontinuous precipitation reactions, International Materials Reviews 26 (1981) 153-183.

[25] F. Findik. Discontinuous (cellular) precipitation, J Mater Sci Lett 17 (1998) 79-83.

[26] I. Manna, S.K. Pabi, W. Gust. Discontinuous reactions in solids, International Materials Reviews 46 (2001) 53-91.

[27] P.M. Hekker, H.C.F. Rozendaal, E.J. Mittemeijer. Excess nitrogen and discontinuous precipitation in nitrided iron-chromium alloys, J Mater Sci 20 (1985) 718-729.

[28] R.E. Schacherl, P. Graat, E.J. Mittemeijer. Gaseous nitriding of iron-chromium alloys, Zeitschrift für Metallkunde 93 (2002) 468.

[29] G. Miyamoto, A. Yonemoto, Y. Tanaka, T. Furuhara, T. Maki. Microstructure in a plasma-nitrided Fe–18 mass% Cr alloy, Acta Mater 54 (2006) 4771-4779.

[30] M. Sennour, P. Jouneau, C. Esnouf. TEM and EBSD investigation of continuous and discontinuous precipitation of CrN in nitrided pure Fe-Cr alloys, J Mater Sci 9 (2004) 4521-4531.

[31] S.S. Hosmani, R.E. Schacherl, E.J. Mittemeijer. Nitriding behavior of Fe–4wt%V and Fe–2wt%V alloys, Acta Mater 53 (2005) 2069-2079.

[32] H. Selg, E. Bischoff, S.R. Meka, R.E. Schacherl, T. Waldenmaier, E.J. Mittemeijer. Molybdenum-Nitride Precipitation in Recrystallized and Cold-Rolled Fe-1 at. pct Mo Alloy, Metall Mater Trans A 44A (2013) 4059-4070.

[33] T. Steiner, S.R. Meka, B. Rheingans, E. Bischoff, T. Waldenmaier, G. Yeli, T.L. Martin, P.A.J. Bagot, M.P. Moody, E.J. Mittemeijer. Microstructural development of Fe-1 at.%Cr-1 at.%Mo alloy upon nitriding; crystal structure and composition of ternary nitrides, [in preparation] (2015).

[34] S.J.B. Kurz, S.R. Meka, N. Schell, W. Ecker, J. Keckes, E.J. Mittemeijer. Residual stress and microstructure depth gradients in nitrided iron-based alloys revealed by dynamical cross-sectional transmission X-ray microdiffraction, Acta Mater 87 (2015) 100-110.

[35] E. Lehrer. Über das Eisen-Wasserstoff-Ammoniak-Gleichgewicht, Zeitschrift für Elektrochemie und angewandte physikalische Chemie 36 (1930) 383-392.

[36] R. Delhez, E.J. Mittemeijer. An Improved Alpha-2 Elimination, J Appl Crystallogr 8 (1975) 609-611.

[37] A.L. Sutton, W. Hume-Rothery. The Lattice Spacings of Solid Solutions of Titanium, Vanadium, Chromium, Manganese, Cobalt and Nickel in Alpha-Iron, Philos Mag 46 (1955) 1295-1309.

[38] L.J. Dijkstra. Precipitation Phenomena in the Solid Solutions of Nitrogen and Carbon in Alpha-Iron Below the Eutectoid Temperature, T Am I Min Met Eng 185 (1949) 252-260.

[39] K.H. Jack. Results of Further X-Ray Structural Investigations of the Iron Carbon and Iron Nitrogen Systems and of Related Interstitial Alloys, Acta Crystallogr 3 (1950) 392-394.

[40] E.J. Mittemeijer, A.B.P. Vogels, P.J. Van der Schaaf. Aging at Room-Temperature of Nitrided Alpha-Iron, Scripta Metall Mater 14 (1980) 411-416.

[41] E.J. Mittemeijer. Lattice Distortions in Nitrided Iron and Steel, Haerterei-Technische Mitteilungen 36 (1981) 57-67.

[42] P. Ferguson, K.H. Jack. Quenched-Aging and Strain-Aging of Nitrogen-Ferrite Proc. Heat Treatment `81. Londen: The Metals Society, 1983. p.158-163.

[43] E.J. Mittemeijer, A. Van Gent. Unusual Lattice-Parameters in 2-Phase Systems - the Case of Aged Nitrogen-Ferrite, Scripta Metall Mater 18 (1984) 825-828.

[44] R. Kuzel, B. He, C. Houska. Characterization of severe matrix distortions during phase separation from the redistribution of diffracted intensities, J Mater Sci 32 (1997) 2451-2467.

[45] D. Rickerby, S. Henderson, A. Hendry, K.H. Jack. Overview no. 51 Structure and thermochemistry of nitrided iron-titanium alloys, Acta Metall Mater 34 (1986) 1687-1699.

[46] J. Stein, R.E. Schacherl, M.S. Jung, S. Meka, B. Rheingans, E.J. Mittemeijer. Solubility of nitrogen in ferrite; the Fe-N phase diagram, Int J Mater Res 104 (2013) 1053-1065.

[47] H.A. Wriedt, L. Zwell. Lattice Dilation of Alpha-Iron by Nitrogen, T Metall Soc Aime 224 (1962) 1242-&.

[48] R.G. Baker, J. Nutting. The tempering of a Cr-Mo-V-W and a Mo-V steel, Iron and Steel Institute Special Report 64 (1959) 1-22.

Chapter 5

Misfit Induced Changes of Lattice Parameters in Two-Phase Systems: Coherent/Incoherent Precipitates in a Matrix

Maryam Akhlaghi, Tobias Steiner, Sai Ramudu Meka and Eric Jan Mittemeijer

Abstract

Elastic accommodation of precipitation induced or thermally induced misfit leads to lattice-parameter changes in crystalline multi-phase systems. Formulae for calculation of such misfit induced lattice-parameter changes are presented for the aggregate (matrix + second phase particles) and for the individual matrix phase and the individual second phase, recognizing the occurrence of either coherent diffraction or incoherent diffraction by matrix and second phase particles. An overview and (re)interpretation on the above basis is presented of published lattice-parameter data, obtained by X-ray diffraction analyses of aggregates of matrix plus second phase particles. The experimental data are shown to be in good to very good agreement with predictions according to the current treatment.

5.1. Introduction

5.1.1. micro-and macrostrains; coherent and incoherent diffraction

The complex interplay of the chemical Gibbs energy change driving solid state phase-transformations and the deformation energy associated with the elastic/plastic accommodation of the misfit of parent and product phases, hinders the prediction of the course and the kinetics of phase transformations [1-3]. Accordingly, unusual, non-equilibrium phenomena can occur: occurrence of metastable phases, non-monotonous variation of transformation rate, and unusual morphologies [4-9]. Therefore, it is essential to acquire fundamental understanding of the effects of developing misfit-strain energies on the thermodynamics and kinetics of phase transformations. Only thus the resulting microstructure and /properties of engineering components can be optimized [10-12].

The elastic strain field in the matrix surrounding very small (smaller than 1 nm) misfitting particles/point defects can be exposed by high resolution transmission electron microscopy and by X-ray diffraction (diffuse scattering; static Debye-Waller factor [13]). Larger sized misfitting particles can be associated with more extended misfit-strain fields, which evoke contrast in diffraction-contrast images recorded by transmission electron microscopy [14] and broadening of diffraction lines [15, 16]; see in particular chapter 4 of [17].

Application of continuum, elasticity theory to describe the elastic accommodation of the misfit of the (parent) matrix and the (product) second-phase particles [18-20] allows calculation of microstrains, say variance of the local strain $\langle e^2 \rangle$ [15, 16, 21], and of the average (hydrostatic) macrostrain $\langle e \rangle$ [22]. The microstrain expresses itself by (profound) diffraction-line broadening. The hydrostatic macroscopic strain causes (distinct) change of the (average) lattice constant of a phase. Countless observations of diffraction-line broadening due to microstrain have been reported; in fact analysis of diffraction-line broadening has become a standard method of microstructural characterization [17]. However, and perhaps amazingly, only very few experimental works have been devoted to change of the (average) macroscopic lattice parameter by misfit strain [23-28]. This can be due to a relatively small volume misfit in the investigated systems and/or a high rate of relaxation of the misfit in comparison to the rate of transformation and/or a too low rate of acquisition of diffraction patterns. Against the above background, this manuscript presents a review of misfit induced (average, macroscopic) lattice-parameter changes, as predicted and as observed. In this context in particular the distinction of cases of coherent and incoherent diffraction by second-phase/matrix assemblies is emphasized.

The coherent or incoherent nature of the diffraction by a second phase (as precipitate particles) with the diffraction by the matrix need not coincide with the occurrence of a coherent or incoherent nature of the interfaces between the second phase particles and the matrix. Coherency/incoherency of diffraction depends on whether or not constructive interference of waves scattered by separate parts

of the diffracting material (matrix and second phase) occurs. For a detailed discussion on the origin of coherent and incoherent diffraction of a second phase particle and the matrix the reader is referred to [2, 16]. The effect of lattice-parameter variation/ the distribution of lattice spacings in a diffracting material on the occurrence of coherent or incoherent diffraction (and intermediates thereof) is considered most generally in [29].

Provided matrix and second phase particles diffract independently, i.e. incoherent diffraction of matrix and of second phase particles occurs, the changes of the lattice parameters of the matrix and of the second phase particles can be determined from measurements of the positions of the (separate) X-ray diffraction peaks of the matrix and of the second phase. If a coherent nature of the second phase particles/matrix interfaces prevails, then, depending on the length of the diffraction vector and the extent of misfit-strain variation, coherent diffraction by second phase particles and matrix can occur.

5.2. Lattice-parameter changes due to elastically accommodated misfit

A continuum theory for the fully elastic accommodation of the misfit of a point imperfection in a matrix has been presented by Eshelby [18, 19]. The theory was developed in particular to predict the dependence of the lattice parameter of a crystalline solid solution on solute/point defect content (cf. Vegard ´s law [30]). However, for this application the theory failed, as electronic interaction on the atomic/point- defect scale can be dominant over elastic straining effects [31]. The theory is more likely applicable to the case of precipitation of misfitting entities of larger dimensions, as second phase particles (i.e. a block of atoms), which is more likely to exhibit elastic characteristics as for bulk materials. The source of misfit can be precipitation/structure-change induced or thermally induced (e.g. by cooling) specific volume differences (section. 5.2.4).

In the following subsections, formulae are presented that describe the changes of the relative volume/lattice-parameters of the matrix, of the misfitting particles and of the assembly, i.e. matrix plus misfitting particles.

5.2.1. Change of the lattice parameter of the matrix

Insertion of misfitting inclusions *B* into holes of a matrix *A* leaves the whole assembly in a state of self-stress. Considering i) a *finite* matrix *A* containing, in the strain-free condition, holes of radius r_A^0 and ii) particles *B,* of strain-free radius r_B^0, the relative volume increase of the matrix *A* due to the insertion of the misfitting inclusions *B* into the holes of the matrix *A* can be written as [31]:

$$\frac{\Delta V_A}{V_A} = \frac{16}{3}\pi \frac{\mu_A}{K_A} C_6 \varepsilon (r_A^\circ)^3 n \tag{5-1}$$

with $$C_6 = \frac{3K_B}{3K_B + 4\mu_A} \tag{5-2}$$

where n is number of inclusions B per unit volume, ε represents the linear misfit parameter (explained in section 5.2.4) and K and μ represent the bulk modulus and the shear modulus, respectively. The volume fraction of inclusions y_B can be taken as $y_B = 4\pi(r_B^\circ)^3 n/3$. For the case of a matrix of cubic crystal structure with a (strain-free) lattice parameter a_A, $\Delta V_A/V_A$ can be approximated by $3\Delta a_A/a_A$, and Eq. 5-1 can be rewritten as [23]:

$$\Delta a_A = \frac{4\mu_A C_6}{3K_A} \frac{\varepsilon}{(1+\varepsilon)^3} y_B a_A \tag{5-3}$$

It is important to note that the matrix is of finite dimensions. In an *infinite* matrix, the volume change of the matrix due to the introduction of misfitting inclusions is zero (the matrix only experiences shear strains); then, the volume change of the assembly is fully confined to the second phase particles. The matrix dilatation that is predicted for a matrix of *finite* size is a consequence of the image forces required to achieve a stress-free surface of the finite assembly [31].

5.2.2. Change of the lattice parameter of the misfitting phase

A misfitting inclusion with a radius larger or smaller than that of the hole in the matrix, upon insertion into the hole, will experience hydrostatic compression or tension, respectively. For the case of a *finite* assembly of matrix A plus misfitting inclusions B, the fractional volume change of the inclusions can be written as [32]:

$$\frac{\Delta V_B}{V_B} = -3\varepsilon(1 - C_6) + \frac{16}{3}\pi \frac{\mu_A}{K_B} C_6 \varepsilon (r_A^\circ)^3 n \tag{5-4}$$

For the case of second phase particles of cubic crystal structure with a (strain-free) lattice parameter a_B, $\Delta V_B/V_B$ can be approximated by $3\Delta a_B/a_B$, and it follows for the change of the lattice parameter, Δa_B, of the misfitting second phase:

$$\Delta a_B = \left[-\varepsilon(1 - C_6) + \frac{4\mu_A C_6}{3K_B} \frac{\varepsilon}{(1+\varepsilon)^3} y_B\right] a_B \tag{5-5}$$

The total relative volume change of the inclusions results from the sum of the fractional volume change of the inclusions in an *infinite* assembly (first term in Eqs. (5-4) and (5-5)) and the fractional volume change of the inclusions due to the image forces acting (also) on the inclusions in a *finite* assembly (second term in Eqs. (5-4) and (5-5)).

5.2.3. Change of the lattice parameter of the assembly (matrix plus misfitting phase)

The relative volume change of the whole, *finite* assembly comprising the finite matrix and the misfitting inclusions can be given as [31]:

$$\frac{\Delta V}{V} = 4\pi C_6 \varepsilon (r_{\mathrm{A}}^{\circ})^3 n + \frac{16}{3}\pi \frac{\mu_{\mathrm{A}}}{K_{\mathrm{A}}} C_6 \varepsilon (r_{\mathrm{A}}^{\circ})^3 n = 4\pi \frac{C_6}{C_6^{'}} \varepsilon (r_{\mathrm{A}}^{\circ})^3 n \tag{5-6}$$

with

$$C_6^{'} = \frac{3K_{\mathrm{A}}}{3K_{\mathrm{A}} + 4\mu_{\mathrm{A}}} \tag{5-7}$$

For an aggregate of cubic crystal structure and a (strain-free) lattice parameter of the matrix, a, thus approximating $\Delta V/V$ by $3\Delta a/a$, the resulting change of the lattice parameter, Δa, of the aggregate for a volume fraction y_{B} of inclusions *B* is given by:

$$\Delta a = \frac{C_6}{C_6^{'}} \frac{\varepsilon}{(1+\varepsilon)^3} y_{\mathrm{B}} a \tag{5-8}$$

The total relative volume change of the assembly, analogous to the case of the relative volume change of only the inclusions, results from the sum of the fractional volume change of the inclusions in an *infinite* assembly (first term in Eq. (5-6) (this volume change is confined to the inclusions; cf. section 5.2.1)) and the fractional volume change of the assembly due to the image forces required to achieve a stress-free surface of the *finite* assembly (second term in Eq. (5-6)).

5.2.4. The misfit parameter

The linear misfit parameter appearing in the above equations can be given an explicit, analytical expression in the following cases:

i) Thermal misfit: This misfit originates from a change in the temperature of the two (or multi) phase composite (matrix + second phase particles) due to the difference in linear thermal expansion coefficients of matrix (α_{A}) and the second phase precipitate (α_{B}). This type of misfit can be described by the linear thermal misfit parameter, ϵ_T:

$$\epsilon_T = (\alpha_{\mathrm{A}} - \alpha_{\mathrm{B}})(T_h - T_r) \tag{5-9}$$

where T_{h} and T_{r} stand for elevated heat-treatment temperature and the considered, low (e.g. room) temperature, where measurements are made, respectively.

ii) Precipitation-induced misfit: This misfit originates from the different specific volumes of (solute and solvent) atoms in the second phase (precipitate) and the (solute and solvent) atoms in the matrix. This type of misfit can be described by the linear volume misfit parameter, ϵ_V :

$$\epsilon_V = \frac{\sqrt[3]{v_B^0} - \sqrt[3]{v_A^0}}{\sqrt[3]{v_A^0}} \tag{5-10}$$

where v_{B}^0 and v_{A}^0 are the volumes of the strain-free precipitate particle and the volume occupied by the atoms of the precipitate particle as previously incorporated in the matrix, respectively.

5.3. Observations and discussion

At elevated (aging/annealing) temperature (T_h), development of a misfitting, second phase can occur from a supersaturated matrix. The volume misfit (ϵ_V) of the two phases can initially be accommodated elastically under preservation of a coherent interface. Upon prolonged annealing, leading to an increasing size of the second phase particles, this misfit can no longer be accommodated fully elastically, and the interface can become (semi or) incoherent [9, 11, 33, 34].

Upon cooling from elevated temperature (T_h) to room temperature (T_r) (i.e. the temperature at which X-ray measurements are usually performed), irrespective of whether the precipitation-induced misfit at elevated temperature is accommodated elastically or plastically, thermal misfit arises which has to be accommodated either elastically [23] or plastically [35]. In many cases, upon fast cooling of the specimens, the thermal misfit accommodation occurs mainly elastically (even if an incoherent matrix/second phase particle occurs) and it can remain in that state for long time due to very slow rates of plastic relaxation processes at low (room) temperature.

As long as the (transformation or thermal) misfit is accommodated elastically, its effect on the expansion/contraction of the system consisting of matrix and misfitting second phase particle can be quantified considering the model description presented in section. 5.2. Thus, in the following three types of systems consisting of a matrix with misfitting second phase particles are dealt with (see Table 5-1), which differ in the origin of misfit (transformation induced or thermally induced) and in the type of diffraction (coherent or incoherent diffraction of matrix plus second phase particles). Values used for the physical constants and misfit parameters are presented in Table 5-2 and Table 5-3, respectively.

Table 5-1. Types of systems consisting of a matrix with misfitting second phase particles, categorized on the basis of the type of elastically accommodated misfit (column 2) and of the type of precipitate/matrix diffraction (column 3; cf. section 5.1). Equations to be used for the calculation of lattice-parameter changes of the assembly (Eq. (5-8)), the matrix (Eq. (5-3)) and the second phase particle (Eq. (5-5)) (column 4) and system examples (column 5).

type of system	type of elastically accommodated misfit	type of precipitate/ matrix diffraction	lattice-parameter change	case studies
1	transformation misfit	coherent	Eq. (5-8)	nitrided Fe-Me alloys (Akhlaghi *et al.*, 2015) Co clusters in decomposed Cu-Co alloy (Michaelsen, 1995)
2	transformation misfit	incoherent	Eqs. (5-3) and (5-5)	aged (at RT) Fe-N alloy (Mittemeijer & van Gent, 1984, Mittemeijer, 1981, Ferguson & Jack, 1983)
3	thermal misfit	incoherent	Eqs. (5-3) and (5-5)	aged AlSi alloy (Mittemeijer *et al.*, 1981, van Mourik *et al.*, 1985, van Mourik *et al.*, 1988, van Mourik *et al.*, 1983) nitrided and aged Fe-Cr alloys (Steiner *et al.*, 2015)

Table 5-2. Values of the physical constants used in the model calculations of lattice-parameter changes.

	lattice-constants [Å]	K [GPa]	μ [GPa]	α *10 $^{-6}$ [K^{-1}]
Fe	2.8664 (bcc) (ICDD, 2002)	166 (Wawra, 1978)	82 (Wawra, 1978)	12.1 (Smithells, 1976)
CrN	4.1400 (NaCl) (ICDD, 2002)	360 (Grossman *et al.*, 1999)	-	2.3 (Samsonov, 1964)
VN	4.1392 (NaCl) (ICDD, 2002)	300 (Dzivenko *et al.*, 2010)	-	8.1 (Samsonov, 1964)
Cu	3.6150 (fcc) (ICDD, 2002)	140 (Wang *et al.*, 2009)	48 (Smithells, 1976)	17 (Smithells, 1976)
Co	3.5442 (fcc) (Taylor & Floyd, 1950)	140 † (Wang *et al.*, 2009)	-	-
$Fe_{16}N_2$	5.7200 (bct) 6.2900 (ICDD, 2002)	166 † (Wawra, 1978)	-	-

Al	4.0494 (fcc) (ICDD, 2002)	75 (Smithells, 1976)	26 (Smithells, 1976)	23.5 (Smithells, 1976)
Si	5.4309 (diamond) (ICDD, 2002)	98 (Madelung *et al.*, 2001)		3 (Roberts, 1981)

Table 5-3. Values of the misfit parameters used in the model calculations of lattice parameter changes. Values of thermal misfits are underlined and the other values are corresponding to precipitation-induced misfit.

inclusion \ **matrix**	**Fe**	**Cu**	**Al**
CrN	0.1464 *0.004 (ΔT= 375 °C)* *0.005 (ΔT= 475 °C)*	-	-
VN	0.1461 *0.002 (ΔT= 375 °C)*	-	-
Co	-	-0.0173	-
$Fe_{16}N_2$	0.0299	-	-
Si	-	-	*0.003 (ΔT= 127°C)*

5.3.1. Coherent diffraction by the assembly matrix plus second phase particles; transformation misfit

5.3.1.1. Misfitting coherent alloying element nitrides in ferrite

Upon nitriding of ferritic Fe-Me (Me: Cr, V, Ti) alloys, tiny nitride precipitates (MeN) develop [36-40]. At least initially these nitrides possess coherent interfaces with the matrix. Matrix/nitride-particle misfit in this system, as considered at room temperature, originates from i) the specific volume misfit induced by nitride precipitation from a supersaturated matrix as a consequence of elastic accommodation of the misfit while the precipitate/matrix interface remains coherent and ii) the thermal misfit induced by cooling after nitriding. The specific volume misfit between MeN precipitates and the ferrite matrix can be calculated from Eq.(5-10), where v_B^0 and v_A^0 can now be taken as molar volumes of MeN precipitates and matrix, respectively. After *completed* precipitation, the molar volume of MeN precipitate can be calculated from the volume of the precipitate unit-cell divided by the number of metals atoms occupying one unit cell of the precipitate and the molar volume of matrix (in this case, containing only Fe atoms) can be calculated from the volume of matrix unit-cell divided by the number of iron atoms occupying

one unit cell of the matrix. In this case the thermal misfit (corresponding to the difference of the thermal expansion coefficients of the Fe-matrix and the developed nitrides) is negligible as compared to the precipitation induced misfit (i.e. $\varepsilon_V = 0.1464$ and $\varepsilon_T = 0.004$ for cooling from 400 °C to room temperature for nitrided Fe-Cr alloy and $\varepsilon_V = 0.1461$ and $\varepsilon_T = 0.002$ for cooling from 400 °C to 25 °C for nitrided Fe-V alloys [41, 42].

This system is an example of *coherent* diffraction by the entity matrix plus precipitates in the presence of *coherent* interfaces between the Fe matrix (of bcc crystal structure) and the MeN precipitates (of NaCl crystal structure). Hence, the overall expansion of the assembly (composed of MeN nitride precipitates and ferrite matrix), expressed in terms of the change in the lattice parameter deduced from the position of the "ferritic" peak maxima, can be calculated using Eq.(5-8), as a function of the volume fraction of alloying element nitrides. Experimental values for such changes of lattice parameter upon nitriding, of Fe-Cr and Fe-V alloys, were obtained by employing X-ray diffraction on homogenously nitrided (thus macroscopically strain-free) Fe-Me specimens [43][4]. The volume fraction of (CrN and VN) nitride precipitates was determined (by weight-change measurements) from the N content of denitrided thin foils (i.e. after removing from the specimen, by denitriding, the dissolved (excess) N and the excess N adsorbed at the nitride-platelet faces during nitriding [44, 45]). The volume fraction of precipitates was varied by varying the nitriding time (for times larger than the minimal time to achieve a homogenously nitrided specimen) and/or varying the amount of Me (Cr,V) in the alloy. Results are shown in Figure **5-1** (the single dots). The predictions on the basis of Eq. (5-8) (solid lines in Figure **5-1**) are in good agreement with the experimental data. Evidently, in this case Eq. (5-3) (implying incoherent diffraction of matrix and precipitates; dashed lines in Figure **5-1**) does not at all correctly predict the ferritic (X-ray) lattice-parameter changes observed for the nitrided Fe-Cr and Fe-V alloys.

5.3.1.2. Misfitting coherent cobalt precipitates in copper

A thin film of a metastable Cu(Co) solid solution can be prepared by co-deposition of Cu and Co by magnetron sputtering up to a maximum of 12 at.% Co. For Co contents larger than 12 at.%, clusters/tiny precipitates of Co occur in the alloy [46, 47].

The X-ray diffraction patterns recorded from such Cu-Co alloy films of different Co concentrations show the occurrence of a single fcc Cu(Co) phase up to 65 at.% Co. Only beyond this Co-concentration, additional hcp (Co) reflections can be observed (see Fig. 5 in [47]).

[4] Indeed no separate nitride reflections could be discerned; the strongly broadened ferritic peaks represent coherent diffraction by the distorted (by elastic misfit-strain accommodation) ferrite matrix and the nitride precipitates (for details see [43]).

Evidently, the Co inclusion/particles present in the Cu-Co alloy films with more than 12 at.% Co and up to 65 at.% Co diffract coherently with the matrix.

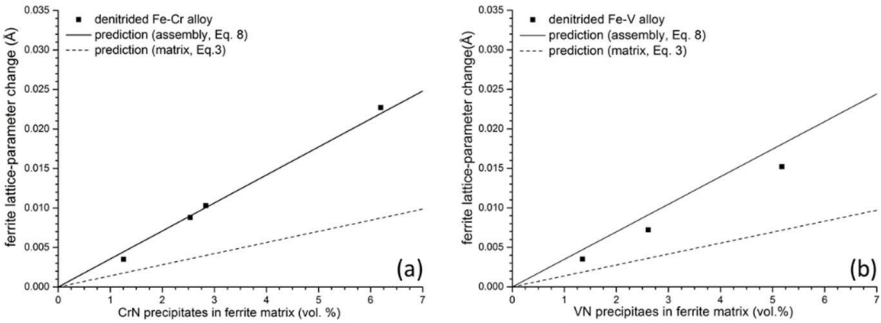

Figure 5-1. Experimental "ferrite" lattice-parameter change (dots; data from [43] as a function of vol.% of (a) CrN precipitates and (b) VN precipitates and the predictions on the basis of Eq. (5-8) (solid line) and Eq. (5-3) (dashed line). The error in the experimental lattice parameter values obtained after fitting the measured diffractograms is ± 0.0003 Å.

The experimentally obtained lattice parameter changes of the fcc Cu(Co) films as function of volume fraction of Co precipitates are shown as single dots in Figure **5-2** for Co concentrations between 12-65 at.%. The predictions of the lattice-parameter value changes of the aggregate Cu matrix (Cu-12 at.% Co solid-solution) and second phase, Co particles as function of the volume fraction of Co precipitates in the Cu (12 at.% Co) matrix according to Eq. (5-8) (coherent diffraction of matrix and inclusions) and Eq. (5-3) (incoherent diffraction of matrix and inclusions) are shown in Figure **5-2**. Evidently, the experimentally determined lattice-parameter values and the predictions on the basis of Eq. (5-8) (solid black line in Figure **5-2**) are in very good agreement, implying occurrence of coherent diffraction of matrix and precipitates. In this case predictions according to Eq. (5-3) (incoherent diffraction of matrix and precipitates; (dashed line in Figure **5-2**) are not at all in agreement with the experimental data.

In this case of very small transformation misfit (see Table **5-3**), it should be recognized that adoption of a Végard-like relationship for the dependence of the lattice parameter of the Cu(Co) solid solution on solute (Co) content would lead to a similar relationship as the one calculated for the coherently diffracting assembly (Eq. (5-8)) and shown in Figure **5-2**. However, only the physical background of the model leading to Eq. (5-8) is compatible with the occurrence of fcc Co precipitates in the Cu (12 at.% Co) matrix.

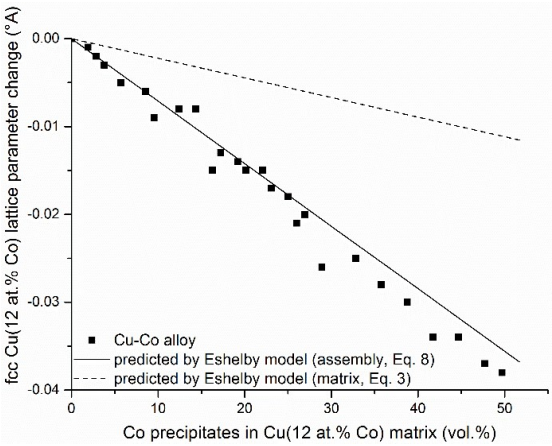

Figure 5-2. Experimental Cu-12 at.% Co lattice-parameter change (dots; data from [47]) as a function of vol. % of Co precipitates in Cu(12 at.% Co) matrix and the predictions on the basis of Eq. (5-8) (solid line) and Eq. (5-3) (dashed line). For the application of Eq. (5-8), it is assumed that Co in the Cu matrix has precipitated as fcc Co particles.

5.3.2. Incoherent diffraction of the matrix and second phase particles; transformation misfit

5.3.2.1. Misfitting incoherent nitrides in ferrite

Upon nitriding of pure α-Fe (ferrite) in an atmosphere of a certain nitriding potential, N dissolves in the ferrite matrix. The formation of this solid solution leads to an increase of the lattice parameter of the ferrite matrix. By quenching after nitriding the solid solution can be retained. The system then is metastable. During aging of the α-Fe matrix supersaturated with dissolved N at room temperature, formation of α′′-$Fe_{16}N_2$ precipitates occurs in association with depletion of N from the ferrite matrix. Experimentally, a decrease of the ferrite lattice parameter is observed at room temperature during development of the α′′precipitates [24, 48-50]. Upon prolonged aging, after completed precipitation of α′′, a constant lattice parameter value is established that is larger than the as expected for a pure α-Fe (the equilibrium solubility of N in α- Fe at room temperature is practically nil) (see Figure 4 in [49], Figure 1 in [48] and Figure 7 in [50].

The values of the constant lattice parameter of the ferrite matrix at this stage of prolonged aging at room temperature, i.e. after all N has precipitated, as recorded from specimens containing different amounts of nitrogen, are shown as a function of the volume fraction of developed α′′ precipitates in Figure **5-3**. Predictions for the change of the ferritic lattice parameter are also

shown in Figure **5-3**: (i) for the case of incoherent diffraction of matrix and precipitates (Eq.(5-3); dotted line in Figure **5-3**) and (ii) for the case of coherent diffraction of the assembly matrix plus precipitates (Eq.(5-8); full Figure **5-3**). The experimental results very well agree with the predictions according to Eq.(5-3): Evidently, in this case of prolonged ageing, the α-Fe matrix and the α′′-nitrides precipitates diffract incoherently. The separate α′′reflections are very weak[5], because of the small amounts of N (and thus α′′) in the specimens and cannot be observed by conventional laboratory XRD (as is the case here; synchrotron radiation would be required as shown by [51].

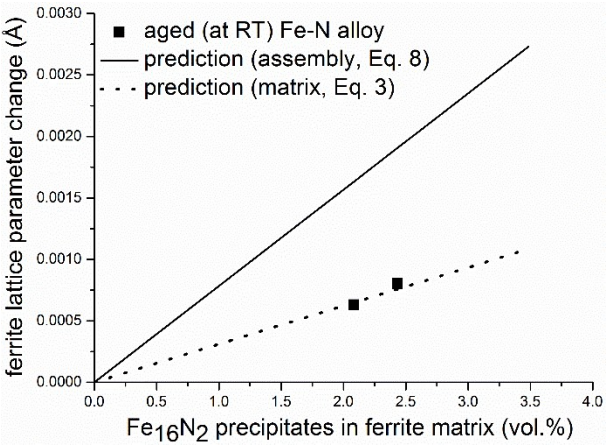

Figure 5-3. Experimental Fe-matrix lattice-parameter change (dots; data from [24. 50]) as a function of vol.% of α′′precipitates and the predictions on the basis of Eq. (5-8) (solid line) and Eq. (5-3) (dashed line).

As mentioned above, before completed precipitation of α′′, i.e. in the intermediate stages of aging, the lattice parameter of ferrite decreases continuously as the ferrite-lattice contraction by the depletion of N, dissolved on the interstitial (octahedral) sites of the ferrite matrix, is larger than the ferrite-lattice expansion due to the formation of misfitting α′′ precipitates diffracting either coherently or incoherently with the matrix. Thus, *during* precipitation of α′′, a (possibly occurring) change of the diffraction conditions from coherent to incoherent will only lead to a change in magnitude of the resulting lattice-parameter decrease. Corresponding calculations for the change of the ferritic-lattice parameter as a function of the fraction transformed (i.e. the precipitated fraction of N), for a fixed N-content of the specimen, are shown in Figure **5-4**: (i) for the case considering both the effect of the depletion of dissolved N from the solid-solution (Eq.

[5] The α′′ crystal structure can be conceived as a superstructure developing in nitrogen ferrite by ordering of N on the sublattice of octahedral interstices. The intensity of the α′′structure specific superstructure reflections is governed by the weak scattering power of the nitrogen atoms.

(1) in [48]) and incoherent diffraction of matrix and precipitate (Eq. (5-3); dashed line in Figure **5-4**), (ii) for the case considering both the effect of the depletion of dissolved N from the solid-solution (Eq. (1) in [48]) and coherent diffraction of assembly matrix plus precipitates (Eq.(5-8); full line in Figure **5-4**) and (iii) for the case considering only the effect of the depletion of dissolved N from the solid-solution (Eq. (1) in [48]); dotted line in Figure **5-4**). Evidently, ignorance of the effect of misfit strain on lattice-parameter change, results in a strongly erroneous (too small) precipitated fraction of N as derived from the decrease of lattice parameter.

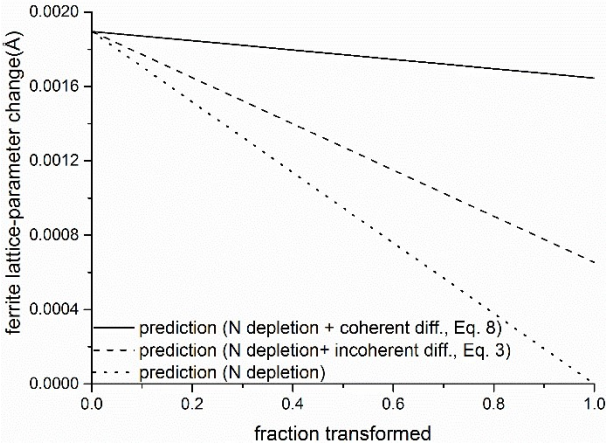

Figure 5-4. Lattice-parameter change of the nitrided ferrite matrix upon precipitation of α´´ as a function of the fraction N precipitated for a specimen of ferrite containing 0.24 at.% N. Calculations on the basis of Eq. (5-8) (solid line) and Eq. (5-3) (dashed line), with considering the effect of nitrogen depletion of the ferrite matrix. The change of the ferrite-lattice parameter due to only N depletion is also shown (dotted line; calculated using Eq. (1) in [48].

5.3.3. Incoherent diffraction of the matrix and second phase particles; thermal misfit

5.3.3.1. Misfitting incoherent silicon in aluminum

During high temperature annealing/aging of an Al matrix supersaturated with dissolved Si, precipitation of (incoherent) Si occurs. Initially, lattice *expansion* of the Al matrix happens due to partial elastic accommodation of the precipitate/matrix misfit (cf. Eq (5-3)) and depletion of Si from the solid solution (see Fig. 9 in [32]). This same process also results in lattice *contraction* for the Si precipitates (cf. Eq. (5-5); see Fig. 7 in [32]). Upon prolonged aging at high temperature, this precipitation induced misfit relaxes fully, i.e. is accommodated entirely plastically. Then a case of *incoherent* diffraction of matrix and precipitates in the presence of *incoherent* interfaces

between the Al matrix (with fcc crystal structure) and the Si precipitates (with diamond cubic crystal structure) is established.

Now, upon rapid cooling of such a relaxed two phase (*pure* Al matrix + incoherent Si-particles) specimen to room temperature, thermal misfit develops, owing to the difference of the thermal expansion coefficients of Al matrix and Si precipitates; this misfit ($\varepsilon_T = 0.003$ for cooling from 152 °C to room temperature) is accommodated elastically. The changes of the lattice parameters of the matrix and the precipitates were measured as a function of the volume fraction of developed precipitates (Si), utilizing the separate diffraction peaks from matrix and precipitates as recorded from fast cooled (to suppress any relaxation of the thermal misfit during cooling) two phase specimens of different Si contents. The thus experimentally obtained lattice-parameter change for the Al-matrix is shown as a function of the volume fraction of Si precipitates in Figure **5-5**(a) (dots). The prediction (now) on the basis of Eq. (5-3) (dashed line in Figure **5-5**(a)) is in good agreement with the experimental data. Evidently, in this case Eq.(5-8) (5-8) (implying coherent diffraction of matrix and precipitate; solid line in Figure **5-5**(a)) does not at all correctly predict the lattice-parameter change of the aluminum matrix. An only reasonable agreement occurs for the theoretical (Eq. (5-5)) and experimental values for the lattice-parameter change of the silicon precipitates (Figure **5-5**(b)); significant experimental errors are inherent to the determination of the minority-phase lattice parameter of the Si precipitates, in particular for the alloy of lowest Si content of 2.8 (vol.%) (cf. Figure **5-5**(b)).

5.3.3.2. Misfitting incoherent alloying element nitrides in ferrite

As described in section 5.3.1, upon nitriding Fe-Cr alloys misfitting CrN particles develop which initially have a coherent interface with the matrix leading to an overall lattice expansion as observed from the change of the "ferrite" lattice parameter (cf. Figure **5-1**). Upon aging (at the nitriding temperature), coarsening of the precipitates occurs (see Fig. 5 of [52]) in association with the development of incoherent matrix/precipitate interfaces: plastic accommodation of the precipitation induced misfit. Consequently, the system (now) exhibits incoherent diffraction of matrix and precipitates (i.e. matrix and coarsened precipitates now diffract separately: indeed both matrix and precipitate reflections are detected (see Fig. 11 of [52]).

Upon cooling of this relaxed two-phase composite (Fe matrix + incoherent CrN nitrides) to room temperature, thermal misfit develops, owing to the difference of the thermal expansion coefficients of Fe matrix and CrN nitrides; this misfit ($\varepsilon_T = 0.005$ for cooling from 500 °C to room temperature) gets accommodated elastically. The change of the lattice parameter of the *ferrite matrix* by elastic accommodation of this thermal misfit has been measured by X-ray diffraction and has been predicted on the basis of Eq. (5-3). A very good agreement occurs (Table **5-4**). The change of the lattice parameter of the *precipitates* has also been measured by X-ray diffraction and has been predicted on the basis of Eq. (5-5). As predicted, the experimental change of the lattice parameter of the precipitates has a sign opposite to that of the matrix (cf. Table **5-4**).

The quantitative agreement here is less good, which can be ascribed to uncertainty concerning the strain-free lattice parameter of CrN [53] and limited accuracy in the experimental determination of the lattice parameter of the minority phase.

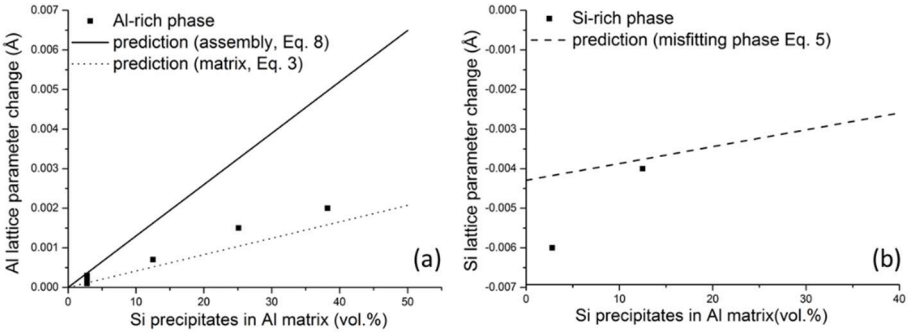

Figure 5-5. (a) Experimental Al-matrix lattice-parameter change (dots; data from Table 1 (experiments were performed between 425-448 K) in [23]) as a function of vol.% of Si precipitates and the predictions on the basis of Eq. (5-8) (solid line) and Eq. (5-3) (dashed line) (b) Experimental Si-precipitate lattice-parameter change (dots; data from Table 1 (experiments were performed at 425 K) in [32]) as a function of vol.% of Si precipitates and the prediction on the basis of Eq. (5-5) (dashed line).

Table 5-4. Change of the Fe-matrix lattice parameter and that of the CrN-precipitates for a homogenously nitrided (till saturation) Fe-4.5 at.% Cr specimen as measured after aging at 500 °C for 78 h, and as predicted on the basis of Eq. (5-3) and Eq. (5-5), respectively.

phase	Δa prediction [Å]	Δa experiment [Å]
α-Fe	+ 0.0005 (Eq. (5-3))	+ 0.0006 (Steiner *et al.*, 2015)
CrN	- 0.0045 (Eq. (5-5))	- 0.0020 (Steiner *et al.*, 2015)

5.4. Conclusions

Formulae have been presented for calculation of lattice-parameter changes induced in misfitting matrix/second phase-particles systems.

Diffraction analysis of such lattice-parameter changes requires distinction of (i) coherent diffraction by the matrix/second phase-particles aggregate and (ii) incoherent diffraction of matrix and second phase particles.

A number of examples presented for cases of precipitation induced specific volume misfit and cooling induced thermal misfit show good to very good agreement of theoretical predictions and experimental observations.
The discussed misfit induced lattice-parameter/volume-changes are often ignored in the diffraction (and also in the dilatometric) analysis of phase-transformation kinetics. This can lead to seriously flawed kinetic data.

References

[1] M.J. Starink, P. van Mourik, B.M. Korevaar. Misfit Accommodation in a Quenched and Aged Al-Cu Alloy with Silicon Particles Metallurgical Transactions A 24 (1993) 1723-1731.

[2] E.J. Mittemeijer. Fundamentals of materials science, Springer, Berlin, 2010.

[3] S.J. Song, F. Liu, Z.H. Zhang. Analysis of elastic-plastic accommodation due to volume misfit upon solid-state phase transformation, Acta Materialia 64 (2014) 266-281.

[4] M.H. Biglari, C.M. Brakman, E.J. Mittemeijer. Crystal-Structure and Morphology of Aln Precipitating on Nitriding of an Fe-2 at Percent Al-Alloy, Philosophical Magazine a-Physics of Condensed Matter Structure Defects and Mechanical Properties 72 (1995) 1281-1299.

[5] M. Sennour, C. Esnouf. Contribution of advanced microscopy techniques to nanoprecipitates characterization: case of AIN precipitation in low-carbon steel, Acta Materialia 51 (2003) 943-957.

[6] Y.C. Liu, F. Sommer, E.J. Mittemeijer. Abnormal austenite-ferrite transformation behaviour in substitutional Fe-based alloys, Acta Materialia 51 (2003) 507-519.

[7] S. Loewy, B. Rheingans, S.R. Meka, E.J. Mittemeijer. Unusual martensite-formation kinetics in steels: Observation of discontinuous transformation rates, Acta Materialia 64 (2014) 93-99.

[8] M. Villa, K. Pantleon, M.A.J. Somers. Evolution of compressive strains in retained austenite during sub-zero Celsius martensite formation and tempering, Acta Materialia 65 (2014) 383-392.

[9] S.R. Meka, E. Bischoff, B. Rheingans, E.J. Mittemeijer. Octapod-shaped, nanosized, amorphous precipitates in a crystalline ferrite matrix, Philosophical Magazine Letters 93 (2013) 238-245.

[10] R. Abbaschian, L. Abbaschian, R.E. Reed-Hill. Physical metallurgy principles. 4th ed., Course Technology, Stamford, 2010.

[11] D.A. Porter, K.E. Easterling. Phase Transformations in Metals and Alloys, Van Nostrand Reinhold, London, 1982.

[12] Z. Guo, W. Sha. Quantification of precipitate fraction in Al-Si-Cu alloys, Mat Sci Eng a-Struct 392 (2005) 449-452.

[13] S.C. Moss, M.A.c. Krivoglaz. Theory of X-ray and thermal-neutron scattering by real crystals, Plenum Press, New York, 1969.

[14] T.C. Bor, A.T.W. Kempen, F.D. Tichelaar, E.J. Mittemeijer, E. van der Giessen. Diffraction-contrast analysis of misfit strains around inclusions in a matrix: VN particles in α-Fe, Philosophical Magazine A 82 (2002) 971-1001.

[15] P. Van Mourik, T.H. De Keijser, N.M. Van der Pers, E.J. Mittemeijer. On Misfit-Induced Lattice Spacing Variations in 2-Phase Alloys - the Case of Cooling-Induced Microstrains in the Al-Matrix of Fully Aged Alsi Alloys, Scripta Metallurgica 22 (1988) 1547-1551.

[16] J.G.M. van Berkum, R. Delhez, T.H. de Keijser, E.J. Mittemeijer. Diffraction-line broadening due to strain fields in materials; Fundamental aspects and methods of analysis, Acta Crystallographica Section A 52 (1996) 730-747.

[17] K.S. Jung, R.E. Schacherl, E. Bischoff, E.J. Mittemeijer. The kinetics of the nitriding of ternary Fe-2 at pct Cr-2 at pct Ti alloy, Metallurgical and Materials Transactions A: Physical Metallurgy and Materials Science 43 (2012) 763-773.

[18] J.D. Eshelby. Distortion of a Crystal by Point Imperfections, Journal of Applied Physics 25 (1954) 255-261.

[19] J.D. Eshelby. The Continuum Theory of Lattice Defects, Solid State Physics-Advances in Research and Applications 3 (1956) 79-144.

[20] A.G. Khachaturyan. The Theory of Structural Transformations in Solids, Wiley, New York, 1983.

[21] T. Mura. Micromechanics of Defects in Solids, Martinus Nijhoff Publishers, The Hague, 1982.

[22] P. van Mourik, E.J. Mittemeijer, T.H. de Keijser. On Precipitation in Rapidly Solidified Aluminium-Silicon Alloys, Journal of Materials Science 18 (1983) 2706-2720.

[23] E.J. Mittemeijer, P. van Mourik, T.H. de Keijser. Unusual Lattice-Parameters in 2-Phase Systems after Annealing, Philosophical Magazine A-Physics of Condensed Matter Structure Defects and Mechanical Properties 43 (1981) 1157-1164.

[24] E.J. Mittemeijer, A. van Gent. Unusual Lattice-Parameters in Two-Phase Systems - the Case of Aged Nitrogen-Ferrite, Scripta Metallurgica 18 (1984) 825-828.

[25] J. Zhou, J. Duszczyk, B.M. Korevaar. As-Spray-Deposited Structure of an Al-20Si-5Fe Osprey Preform and Its Development during Subsequent Processing, J Mater Sci 26 (1991) 5275-5291.

[26] G. Timmermans, L. Froyen. Calculation of the effect of alloy characteristics on the permanent expansion of cold compacted hypereutectic Al-Si-Fe-X powder after thermal treatment, Scripta Mater 40 (1999) 743-750.

[27] N.G. Chechenin, A.R. Chezan, C.B. Craus, D.O. Boerma, P.M. Bronsveld, J.T.M. De Hosson, L. Niesen. Precipitate formation in low-temperature nitrided cold-rolled Fe94Ni4Ti2 and Fe93Ni4Cr3 films, Metall Mater Trans A 33 (2002) 3075-3087.

[28] H. Lu, P. Kadolkar, K. Nakazawa, T. Ando, C.A. Blue. Precipitation behavior of AA2618, Metallurgical and Materials Transactions A: Physical Metallurgy and Materials Science 38 (2007) 2379-2388.

[29] A. Leineweber, E.J. Mittemeijer. Notes on the order-of-reflection dependence of microstrain broadening, Journal of Applied Crystallography 43 (2010) 981-989.

[30] L. Vegard. The constitution of the mixed crystals and the filling of space of the atoms, Zeitschrift Fur Physik 5 (1921) 17-26.

[31] J.W. Christian. The Theory of Transformations in Metals and Alloys, Second Edition (2002) p. 200-208.

[32] P. van Mourik, T.H. de Keijser, E.J. Mittemeijer. Misfit strains and excess vacancies in liquid-quenched and solid-quenched AlSi alloys on aging. in Proceedings of "Rapidly Solidified Materials". San Diego, CA, USA, 1985. p.341-350.

[33] S.S. Quek, Y. Xiang, D.J. Srolovitz. Loss of interface coherency around a misfitting spherical inclusion, Acta Materialia 59 (2011) 5398-5410.

[34] P.A. Geslin, B. Appolaire, A. Finel. Investigation of coherency loss by prismatic punching with a nonlinear elastic model, Acta Materialia 71 (2014) 80-88.

[35] J.G.M. van Berkum, R. Delhez, T.H. de Keijser, E.J. Mittemeijer, P. van Mourik. Note on relaxation of cooling-induced strains in two-phase AlSi-alloys at room temperature, Scripta Metallurgica et Materialia 25 (1991) 2255-2258.

[36] R.E. Schacherl, P.C.J. Graat, E.J. Mittemeijer. Gaseous nitriding of iron-chromium alloys, Zeitschrift Fur Metallkunde 93 (2002) 468-477.

[37] G. Miyamoto, A. Yonemoto, Y. Tanaka, T. Furuhara, T. Maki. Microstructure in a plasma-nitrided Fe–18 mass% Cr alloy, Acta Materialia 54 (2006) 4771-4779.

[38] N.E. Vives Díaz, S.S. Hosmani, R.E. Schacherl, E.J. Mittemeijer. Nitride precipitation and coarsening in Fe–2.23at.% V alloys: XRD and (HR)TEM study of coherent and incoherent diffraction effects caused by misfitting nitride precipitates in a ferrite matrix, Acta Materialia 56 (2008) 4137-4149.

[39] D.H. Jack. The structure of nitrided iron-titanium alloys, Acta Metallurgica 24 (1976) 137-146.

[40] D.S. Rickerby, S. Henderson, A. Hendry, K.H. Jack. Structure and Thermochemistry of Nitrided Iron Titanium-Alloys, Acta Metall Mater 34 (1986) 1687-1699.

[41] Z. Basinski, W. Hume-Rothery, A. Sutton, F. Sutton. The lattice expansion of iron, Proceedings of the Royal Society A: Mathematical, Physical and Engineering Sciences 229 (1955) 459-467.

[42] G.V. Samsonov. Plenum Press Handbooks of High-Temperature Materials: No.2 Properties index, Plenum Press, New York, 1964.

[43] M. Akhlaghi, T. Steiner, S.R. Meka, A. Leineweber, E.J. Mittemeijer. Lattice-Parameter Change Induced by Accomodation of Precipitates/Matrix Misfit; Misfitting Nitrides in Ferrite, Submitted to Acta Materialia (2015).

[44] M.A.J. Somers, R.M. Lankreijer, E.J. Mittemeijer. Excess Nitrogen in the Ferrite Matrix of Nitrided Binary Iron-Based Alloys, Philosophical Magazine A 59 (1989) 353-378.

[45] H.H. Podgurski, F.N. Davis. Thermochemistry and nature of nitrogen absorption in nitrogenated Fe-Ti alloys, Acta Metallurgica 29 (1981) 1-9.

[46] A.E. Berkowitz, J.R. Mitchell, M.J. Carey, A.P. Young, S. Zhang, F.E. Spada, F.T. Parker, A. Hutten, G. Thomas. Giant Magnetoresistance in Heterogeneous Cu-Co Alloys, Phys Rev Lett 68 (1992) 3745-3748.

[47] C. Michaelsen. On the Structure and Homogeneity of Solid-Solutions - the Limits of Conventional X-Ray-Diffraction, Philosophical Magazine a-Physics of Condensed Matter Structure Defects and Mechanical Properties 72 (1995) 813-828.

[48] E.J. Mittemeijer, A.B.P. Vogels, P.J. van der Schaaf. Aging at Room-Temperature of Nitrided Alpha-Iron, Scripta Metallurgica 14 (1980) 411-416.

[49] E.J. Mittemeijer. Lattice Distortions in Nitrided Iron and Steel, Haerterei-Technische Mitteilungen 36 (1981) 57-67.

[50] P. Ferguson, K.H. Jack. Quenched-Aging and Strain-Aging of Nitrogen-Ferrite. Proceedings of Heat Treatment `81. Londen: The Metals Society, 1983. p.158-163.

[51] M.J. van Genderen, A. Böttger, R.J. Cernik, E.J. Mittemeijer. Early stages of decomposition in iron-carbon and iron-nitrogen martensites: Diffraction analysis using synchrotron radiation, Metallurgical Transactions A 24 (1993) 1965-1973.

[52] T. Steiner, M. Akhlaghi, S.R. Meka, E.J. Mittemeijer. Diffraction-line shifts and broadenings in continuously and discontinuously coarsening precipitate-matrix systems; relaxation of elastic misfit strain: the case of initially coherent nitride precipitates in a ferrite matrix, submitted to Journal of Materials Science (2015).

[53] ICDD Data Base. PCPDFWIN, 2002.

[54] A. Taylor, R.W. Floyd. Precision measurements of lattice parameters of non-cubic crystals, Acta Crystallographica 3 (1950) 285-289.

[55] H. Wawra. Kröner-limits of elastic moduli of materials of technical importance. Part II: elastic moduli of elements as function of temperature (in German), Zeitschrift für Metallkunde 69 (1978) 518-523.

[56] J. Grossman, A. Mizel, M. Côté, M. Cohen, S. Louie. Transition metals and their carbides and nitrides: Trends in electronic and structural properties, Physical Review B 60 (1999) 6343-6347.

[57] D. Dzivenko, A. Zerr, N. Guignot, M. Mezouar, R. Riedel. Compressibility of cubic vanadium mononitride, EPL (Europhysics Letters) 92 (2010) 66001.

[58] Y. Wang, J. Zhang, H. Xu, Z. Lin, L.L. Daemen, Y. Zhao, L. Wang. Thermal equation of state of copper studied by high P-T synchrotron x-ray diffraction, Applied Physics Letters 94 (2009) 071904.

[59] C.J. Smithells. Metals Reference Book. 5 ed., Butterworth & Co., London 1976.

[60] O. Madelung, U. Rössler, M. Schulz. Silicon (Si) Young's modulus, torsion modulus, bulk modulus (various structures). Landolt-Börnstein - Group III Condensed Matter, vol. 41A1a Springer-Verlag GmbH, Heidelberg, 2001

Chapter 6

Dependence of the nitriding rate of ferritic and austenitic substrates on the crystallographic orientation of surface grains; gaseous nitriding of Fe-Cr and Ni-Ti alloys

M. Akhlaghi, M. Jung, S.R. Meka, M. Fonovic, A. Leineweber and E.J. Mittemeijer

Abstract

Gaseous nitriding of ferritic Fe-Cr and austenitic Ni-Ti solid solutions reveals that the extent of the uptake of dissolved nitrogen depends on the crystallographic orientation of the surface grains of the substrate. In both ferritic and austenitic substrates, the surface nitrogen concentration and the nitriding depth decrease upon increasing the smallest angle between the surface normal and the normal of a {100} plane of the surface grain considered. This phenomenon could be ascribed to the residual compressive macrostress developing during nitriding which varies as a function of crystallographic orientation of the (surface) grains due to the elastically anisotropic nature of ferrite and austenite solid solutions investigated in this study.

6.1. Introduction

Nitriding is a thermochemical surface treatment employed to pronouncedly enhance the wear, fatigue and corrosion resistances of metallic, especially steel components [1, 2]. To arrive at fundamental understanding of the nitriding behavior of multicomponent *ferritic* (bcc) steels, research has been focused on ferritic model alloys such as iron-based binary Fe-Cr alloys [3-9]. Upon nitriding of Fe-Me (Me: Cr, V, Al, Ti, Mo) alloys, the nitrogen dissolves interstitially in the matrix and, after surpassing the solubility product of Me-nitride, precipitation of nanosized, (semi-) coherent MeN nitride platelets develop in the matrix, leading to distinct enhancement of particularly mechanical properties [10-15].

In the case of *austenitic* (fcc), stainless steels, the nitriding treatment is usually performed at low temperatures (< 450°C) and for relatively short times, in order to avoid distinct diffusion of Me and thus formation of MeN precipitates; in this way a high level of N supersaturation can be realized, while preserving Me (in this case Me usually is Cr) in dissolved state. Austenite with such high level of N supersaturation is known in the literature as expanded austenite (previously indicated by the unfortunate name S-phase) [16-27]. The extremely high content of N (i.e. far above the amount compatible with equilibrium) absorbed by the alloyed austenitic matrix, has been attributed to the trapping of N, at octahedral interstitial sites, by alloying element atoms dissolved in the matrix with high affinity for N (such as Cr and Ti) [18, 25, 28]. A similar, expanded austenite (fcc) phase was also observed during low-temperature nitriding/carburizing of nonferrous Ni-based [29-31] and Co-based [32] alloys.

The surface nitrogen content and the thickness of the case of expanded austenite were shown to depend on the crystallographic orientation of the grain considered with respect to the specimen surface: the nitrided depth and the surface nitrogen content are the larger the smaller the angle is between the surface normal and the normal of the {100} lattice plane [16, 30, 33]; the smallest nitrided zone depth and the smallest surface nitrogen content occur for the grains with a {111} plane parallel to the surface. The following explanations for this phenomenon have been offered:

(i) Some researchers have attributed this phenomenon to a supposed intrinsic anisotropy of the nitrogen diffusivity [16, 18]. However, the diffusivity in cubic lattices is essentially isotropic [34].

(ii) The rate of the nitriding reaction between a nitriding medium and a solid substrate can depend on the crystallographic structure of the solid surface exposed to the nitriding medium [35, 36]. As a result, the nitrogen fluxes passing through the surface adjacent grains of different crystallographic orientations can be different.

(iii) Finally, the magnitude of the residual (compressive) macrostress parallel to the surface of the heterogeneously nitrided specimens [9, 30, 37] can depend on the crystallographic

orientation of the grain adjacent to the surface with respect to the surface (note the anisotropy of the intrinsic, single crystal elastic constants). As a consequence, the nitrogen solubility level of the surface [26] and the nitrogen diffusivity [38] can depend on the crystallographic orientation of the surface adjacent grains with regards to the surface.

Against the above background, and recognizing that there appears to be no reason that the effect discussed should be restricted to austenitic substrates only, in the present work, low temperature gaseous nitriding experiments have been carried out on substrates of both *ferritic* Fe-Cr and *austenitic* Ni-Ti alloys. This study shows, for the first time, the occurrence of the surface-grain, crystallographic orientation dependent nitriding rate of *ferritic* alloys. A general explanation for the phenomenon discussed is offered, which is based on the effect of the residual, nitriding induced macrostress on the nitrogen solubility for differently oriented surface grains of an intrinsically elastically anisotropic polycrystalline substrate.

6.2. Theoretical background

6.2.1. Stressed-solid /gas-phase thermodynamic equilibrium

The chemical potential of the nitrogen dissolved in a stress-free (iron) matrix phase ($\mu_N^{\sigma=0}$) is related to the chemical potential of nitrogen in the standard state (μ_N°) and the activity of the dissolved nitrogen ($a_N^{\sigma=0}$) [39]:

$$\mu_N^{\sigma=0} = \mu_N^{\circ} + RTlna_N^{\sigma=0} = \mu_N^{\circ} + RTln(C_N^{\sigma=0}\gamma_N^{\sigma=0}) \quad (6\text{-}1)$$

where R is the gas constant and T is the absolute temperature. The nitrogen activity can be written as the product of the corresponding nitrogen concentration ($C_N^{\sigma=0}$) and the nitrogen activity coefficient ($\gamma_N^{\sigma=0}$).

The chemical potential of nitrogen dissolved in the stressed solid matrix phase ($\mu_N^{\sigma\neq0}$) is described as:

$$\mu_N^{\sigma\neq0} = \mu_N^{\circ} + RTlna_N^{\sigma\neq0} = \mu_N^{\circ} + RTln(C_N^{\sigma\neq0}\gamma_N^{\sigma\neq0}) \quad (6\text{-}2)$$

where $a_{\mathrm{N}}^{\sigma\neq0}$ is the activity of nitrogen in the stressed matrix phase and $C_{\mathrm{N}}^{\sigma\neq0}$ and $\gamma_{N}^{\sigma\neq0}$ are the corresponding nitrogen concentration and nitrogen activity coefficient. Eq. (6-2) can be rewritten according to [40, 41] as:

$$\mu_{\mathrm{N}}^{\sigma\neq0} = \mu_{\mathrm{N}}^{\circ} + \mathrm{R}Tln(C_{\mathrm{N}}^{\sigma\neq0}\gamma_{\mathrm{N}}^{\sigma=0}) - \bar{V}_{\mathrm{N}}\sigma_{\mathrm{h}} \tag{6-3}$$

where $\bar{V}_{\mathrm{N}}$ is the partial molar volume of nitrogen in the matrix phase and σ_{h} is the hydrostatic component of the state of stress acting on the matrix-phase grain considered.

Once equilibrium has been attained at the surface of a (hydrostatically) stressed specimen and of a stress-free specimen with the *same* nitriding atmosphere of defined nitriding potential (at a certain temperature; [1]), the chemical potentials of N in the stress-free specimen ($\mu_{\mathrm{N,eq}}^{\sigma=0}$) and of N in the stressed specimen ($\mu_{\mathrm{N,eq}}^{\sigma\neq0}$) are necessarily the same and equal to the chemical potential of N in the gaseous nitriding medium ($\mu_{\mathrm{N,eq}}^{\mathrm{gas}}$):

$$\mu_{\mathrm{N,eq}}^{\sigma=0} = \mu_{\mathrm{N,eq}}^{\sigma\neq0} = \mu_{\mathrm{N,eq}}^{\mathrm{gas}} \tag{6-4}$$

Accordingly, it follows from Eqs. (6-1) and (6-3) [41, 42]:

$$\frac{C_{\mathrm{N,eq}}^{\sigma\neq0}}{C_{\mathrm{N,eq}}^{\sigma=0}} = \exp\left(\frac{\bar{V}_{\mathrm{N}}\sigma_{\mathrm{h}}}{\mathrm{R}T}\right) \tag{6-5}$$

where $C_{\mathrm{N,eq}}^{\sigma\neq0}$ and $C_{\mathrm{N,eq}}^{\sigma=0}$ are the equilibrium N solubilities in the matrix phase in the presence and in the absence of stress, respectively.

In the following discussion it will be argued how different values for the (hydrostatic component of the state of) stress can occur for differently oriented surface adjacent grains.

Upon nitriding a residual, biaxial, rotationally symmetric *compressive* state of stress develops due to the volume misfit of the nitrided case and the unnitrided core of the specimen [43]: $\sigma_{\mathrm{xx}} = \sigma_{\mathrm{yy}} \equiv \sigma_{//}$ and $\sigma_{\mathrm{zz}} = 0$ with x, y and z as the principal axes for the state of stress (equal to the principal axes for the state of strain for cubic crystals) with the x and y axes in the plane of the surface and the z axis perpendicular to the surface. Usually, the residual stress $\sigma_{//}$ is considered to be the same in every surface adjacent grain of the loaded specimen. However, for intrinsically elastically anisotropic materials, the (state of) stress will actually vary from grain to grain by the elastic interaction of each grain with its surroundings: so-called elastic grain interaction [44, 45].

Now, consider hypothetically a set of non-interacting surface adjacent single crystals with a (*hkl*) plane parallel to the surface, of variable rotation around the surface normal, called "(*hkl*) set" in the following. Then, the state of stress *as described in the specimen frame of reference* (*x*, *y*, *z*) is the same for each crystal of the (*hkl*) set, independent of its angle of rotation around the surface normal, as $\sigma_{xx} = \sigma_{yy}$. For the relationship between $\sigma_{//}$ and $\varepsilon_{\perp}$ (= strain in the surface-normal direction) it straightforwardly follows:

$$\sigma_{//}(hkl) = \frac{1}{2S_{12}^{xyz}(hkl)}\varepsilon_{\perp}(hkl) \tag{6-6}$$

with S_{12}^{xyz} as a single crystal elastic constant in the specimen frame of reference which is related to the intrinsic single crystal elastic constants in the crystal frame of reference (for cubic crystalline materials) by [46]:

$$S_{12}^{xyz}(hkl) = S_{12} + (S_{11} - S_{12} - \frac{1}{2}S_{44})\Gamma_{hkl} \tag{6-7}$$

with Γ_{hkl} as the so-called orientation factor given by [44]:

$$\Gamma_{hkl} = \frac{h^2k^2 + h^2l^2 + k^2l^2}{(h^2 + k^2 + l^2)^2} \tag{6-8}$$

Considering the same set of (*hkl*) crystals in the real, massive polycrystalline specimen, the in reality occurring elastic interaction of each grain with its specific surroundings will lead to different values for $\sigma_{//}$ and $\varepsilon_{\perp}$ for each grain of the (*hkl)* set. (e.g. see Ref. [47, 48]). It will now be assumed that the averaging of the grain interaction in the specimen [45, 49] brings about that the principle features of the intrinsic elastic anisotropy do prevail in the polycrystalline aggregate [50], so that Eq. (6-7) remains valid by interpreting $\sigma_{//}$ and $\varepsilon_{\perp}$ as average values for the (*hkl*) set. Hence, in this paper different (average) states of stress are adopted for different (*hkl*) sets.

The dependence of $1/(2S_{12}^{xyz}(hkl))$ is shown in Figure **6-1** as a function of Γ_{hkl} for pure bcc (ferritic) iron and pure fcc Ni. Evidently (note that both $\sigma_{//}$ (see above) and $1/2S_{12}^{xyz}(hkl)$ are negative), for the same value of $\varepsilon_{\perp}$, the absolute value of the $\sigma_{//}$ is smallest for (*hkl*)=(100) (Γ_{hkl}=0) and largest for (*hkl*)=(111) (Γ_{hkl}=0.33).

Finally, it should be recognized that the treatment leading to Eq. (6-5) is valid for a hydrostatic state of stress (so that the stress is a scalar). At the moment no practically applicable, comprehensive treatment of the thermodynamics of stressed solids exists (for a rigorous

consideration, based on so-called "network solids", incompatible with common practice, see Ref. [51]). It is proposed here, for the case of a non-hydrostatic state of stress, to apply Eq. (6-5) by equating σ_h with the equivalent hydrostatic stress given by the average of the principal components of the stress tensor, i.e. $\sigma_h = (\sigma_{xx} + \sigma_{yy} + \sigma_{zz})/3$, which here becomes (see above): $\sigma_h = \frac{2}{3}\sigma_{//}$.

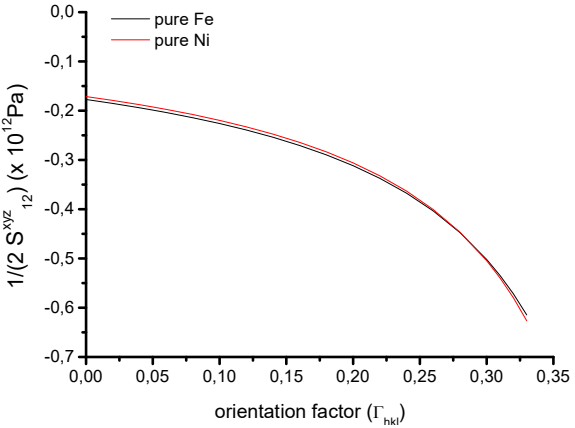

Figure 6-1. The elastic compliance dependent term, $\frac{1}{2\,S_{12}^{xyz}(hkl)}$, as a function of orientation factor (Γ_{hkl} varies from 0 for (100) plane parallel to the surface to 0.33 for (111) plane parallel to the surface) for pure ferrite and pure Ni. The elastic compliances are considered as follows: for pure ferrite; S_{11}= 7.57 TPa^{-1}, S_{12}= -2.82 TPa^{-1} and S_{44}= 8.62 TPa^{-1} and for pure Ni; S_{11}= 7.69 TPa^{-1}, S_{12}= -2.92 TPa^{-1}, S_{44}= 8.36 TPa^{-1} [60].

Because $\sigma_h = \frac{2}{3}\sigma_{//}$ will in general be different for different (*hkl*) sets, it follows that different equilibrium nitrogen solubilities occur at the surface for the different (*hkl*) sets (see Eq. (6-5)). Then also the depths of the nitrided zones of different (*hkl*) sets will be different as the diffusional flux increases with increasing nitrogen concentration gradient. The remainder of this paper presents experimental validation for these conclusions.

To determine σ_h for each (*hkl*) set, the strain $\varepsilon_\perp$, as caused by the stress parallel to the surface as consequence of the macroscopic misfit of nitrided case and unnitrided core, is measured for each (*hkl*) set and $\sigma_h = \frac{2}{3}\sigma_{//}$ then follows by application of Eqs. (6-6)-(6-8). The strain $\varepsilon_\perp(hkl)$ can be determined from (i) the average lattice spacing of the (*hkl*) planes parallel to the surface as determined for the (*hkl*) set of the macroscopically stressed specimen (a heterogeneously nitrided specimen), $d_\perp(hkl)$, and (ii) the corresponding lattice spacing of a macroscopically nitrided specimen devoid of the planar state of stress considered (reference specimen; further see section 6.4.2), $d_0(hkl)$, as follows:

$$\varepsilon_{\perp}(hkl) = \frac{d_{\perp}(hkl) - d_0(hkl)}{d_0(hkl)} \tag{6-9}$$

6.3. Experimental

6.3.1. Specimen preparation

Melts of two alloys of Fe-Cr (Fe-2 at.% Cr and Fe-4.5 at.% Cr) and a melt of Ni-Ti alloy (Ni-5 at.% Ti) were prepared in Al_2O_3 crucibles, under a protective argon gas (99.999 vol.%) atmosphere, from pure Fe (99.98 wt.%) and pure Cr (99.999 wt.%), and pure Ni (99.98 wt. %) and pure Ti (99.999 wt.%), respectively. Subsequently, casts of Fe-Cr (of cylindrical shape with a diameter of 10 mm and a length of 100 mm) and of Ni-Ti (of rectangular shape with width dimensions of 15 mm and 30 mm and a length of 150 mm) were obtained by pouring the melts in appropriate Cu molds. The results of chemical analyses of the produced casts have been presented in Refs. [31, 52]. The cast Fe-Cr ingots were encapsulated in a quartz tube filled with argon gas and were homogenized at 1000 °C for 1 h. The cast Ni-Ti ingots were homogenized in a horizontal quartz tube furnace at 1050 °C for 24 h under a protective flowing (50 ml/min) hydrogen atmosphere by placing the ingot in the middle of the furnace together with a Zr plate as oxygen getter. Afterwards, the Fe-Cr and Ni-Ti casts were cold-rolled to sheets of 1 mm thickness.

Specimens with lateral dimensions of 10 × 15 mm^2 and 25 × 20 mm^2 were cut from these 1mm thick sheets of Fe-4.5 at.% Cr and Ni-Ti alloys, respectively. In order to obtain relatively large grains (approx. 50 μm), the Fe-4.5 at.% Cr specimens were recrystallized at 800 °C for 3 h after encapsulating the specimens in a quartz tube filled with Ar gas and the Ni-Ti specimens were recrystallized at 850 °C for 3 h in a hydrogen atmosphere, followed by slow cooling to room temperature for both types of specimens. A thin foil of the Fe-2 at.% Cr alloy, to be homogenously nitrided (of section 6.5), was produced as described in Ref. [52].

Immediately prior to nitriding, the surfaces of all specimens were ground and polished (final polishing step: 1 μm diamond suspension) and subsequently cleaned with ethanol in an ultrasonic bath.

6.3.2. Nitriding experiments

Controlled gaseous nitriding was performed in a vertical quartz-tube furnace with an inner-tube diameter of 28 mm in an ammonia/hydrogen gas flux. The flow rate of each gas component was adjusted separately using mass-flow controllers. The Fe-Cr alloy specimens were nitrided at 450°C using a nitriding potential (r_N; see Ref. [1]) of 0.104 $atm^{-1/2}$ for 216 h (Fe-2 at.% Cr thin

foil) and for 1 h, 3 h, 6 h, 15 h and 30 h (1 mm thick specimens of Fe-4.5 at.% Cr). The Ni-Ti alloy specimens were nitrided at 400 °C for 65 h using a nitriding potential of 500 $atm^{-1/2}$. The nitriding potentials were chosen such that no iron or nickel nitrides could develop (i.e. the development of only a diffusion zone occurs in all nitrided alloys [1]). Nitriding experiments for the thick specimens were ended by quenching the specimens to room temperature which was achieved by dropping the specimens into nitrogen-flushed water. To avoid breakage of the thin foil of Fe-2 at.% Cr during water quenching, the nitrided thin foil was lifted up into the low temperature zone of the furnace where the foil was allowed to cool slowly in the nitriding atmosphere.

6.3.3. Specimen characterization

6.3.3.1. Light microscopy

To characterize the nitrided zone of the Ni-Ti and the Fe-Cr specimens, pieces from the nitrided specimens were cut normal to the specimen surface, and were electroplated with a nickel layer using a Watts bath at 70°C. Purpose of the Ni-plating is to protect the nitrided layer during the following specimen preparation process. Subsequently, the specimen was embedded in Struers PolyFast. The cross-section was then ground and polished (final polishing step using 1 µm diamond suspension) and etched using an aqueous solution composed of 1 part of 10 wt.% NaCN in water and 1 part of 10 wt.% $(NH_4)_2S_2O_8$ in water for 35 s at room temperature in the case of Ni-Ti specimen, and using 1% Nital (1 vol.% HNO_3 in ethanol) at room temperature during about 10 s for the Fe-2.0 at.%Cr thin foil and for about 30 s for the Fe-4.5 at.%Cr 1 mm thick specimens. Optical micrographs from the etched cross-sections were recorded to measure the nitrided zone depth on each grain in the cross-section using a Zeiss Axiophot microscope equipped with an Olympus ColorView IIIu digital camera. An accurate determination of nitrided zone depth on various grains in the cross-section of nitrided Fe-Cr specimens was impossible by light-optical micrography due to the unclear interface between the nitrided and unnitrided regions. Therefore, optical micrographs recorded from these specimens are not presented in this paper.

6.3.3.2. X- ray diffraction (XRD)

XRD patterns was recorded from the surface of the 1 h nitrided Fe-4.5 at.% Cr specimen using a PANalytical X'Pert diffractometer in Bragg-Brentano configuration equipped with a Co tube and a graphite monochromator in the diffracted beam. XRD pattern was recorded from the surface of the 65 h nitrided Ni-5 at.% Ti specimen using a PANalytical X'Pert diffractometer in Bragg-Brentano configuration equipped with a Cu tube and a Johannson monochromator in the primary beam. The

lattice spacings corresponding to the (*hkl*) reflections were calculated from their peak positions determined by fitting pseudo-Voigt functions using the software TOPAS (Version 4.2, Bruker AXS).

6.3.3.3. Electron probe microanalysis (EPMA)

To determine the elemental (Cr, N and Fe) concentrations of the nitrided zone of the Fe-Cr specimens and the elemental (Ti, N and Ni) concentrations of the nitrided zone of the Ni-Ti specimens, electron probe microanalysis (EPMA) was performed. To obtain the element contents at each measurement point, the intensities of the characteristic X-ray emission peaks were measured and divided by the corresponding intensities obtained from standard samples of pure Fe, Cr, Ti, Ni and γ′-Fe_4N (for N-K_α). Elemental concentrations were calculated from the intensity ratios applying the $\Phi(\rho z)$ approach [53] (note that in the case of nitrided Ni-Ti alloy, due to the overlapping of the N-K_α and Ti-L_1 emission lines, for the accurate determination of N content, the procedure described in Ref. [31] was applied). For these measurements, a Cameca SX100 microprobe (acceleration voltage U = 15 kV, current I = 100 nA, spot size about 1 μm) was used.

6.3.3.4. Electron backscatter diffraction (EBSD)

Electron Backscatter Diffraction (EBSD) was performed on the polished surface of an unnitrided Fe-4.5 at.% Cr (1mm thick) specimen (final polishing step: 0.05 μm OPS-suspension) and the cross-sections of a nitrided Fe-2 at.% Cr thin foil and the nitrided Fe-4.5 at.% Cr and Ni-Ti specimens (final polishing step: 0.05 μm OPS-suspension) with a Zeiss Leo 438 VP scanning electron microscope equipped with an EDAX TSL EBSD measurement system. The data were analyzed using the software OIM version 5. For determining the crystallographic orientation adjacent to the surface of grains, (i) for EBSD measurements performed on the surface of unnitrided specimens, the specimen surface normal direction (ND) was considered as reference direction and (ii) for EBSD measurements presented on the cross-section of nitrided specimens, the specimen rolling direction (RD) was considered as reference direction. In this way, it was possible to identify the same grains (adjacent to the surface of specimen) in both the surface and the cross-section of the same specimen (see also Ref. [30]).

6.4. Results and evaluation

6.4.1. Dependence of surface nitrogen content and nitrided zone depth on crystallographic orientation of surface grains

6.4.1.1. Ni-Ti (fcc) specimens

Formation of an expanded-austenite layer has been observed during nitriding of Ni-Ti alloy specimen [31]. The thickness of this layer formed in different grains adjacent to the surface varies. In order to trace the surface-grain orientation dependence of the extent of nitriding, the crystallographic orientation of each surface adjacent grain with respect to the surface was determined by EBSD (cf. section 6.3.3.4) and expressed by the orientation factor, Γ_{hkl} with (*hkl*) being the lattice plane parallel to the surface (cf. Eq. (6-8)). The orientation factor provides a measure of how large the deviation of the (100) planes of a particular grain from the surface is. Thus, for example, orientation factor values of 0.1, 0.2 and 0.3 represent (100) planes inclined at angles of 19°, 30° and 44.5°, respectively, with respect to the specimen surface. As illustrated in Figure **6-2**, the nitrided zone depth is distinctly larger for the grain with a (100) plane nearly parallel to the specimen surface (i.e. the grain with a (117) plane parallel to the surface; Γ=0.04) than for the grain with a (111) plane parallel to the specimen surface (Γ=0.33). Moreover, the nitrogen-concentration depth profiles measured by EPMA across three surface adjacent grains of this specimen, with orientation factors of 0.19, 0.28 and 0.32, reveal that not only the nitrided depth but also the nitrogen content in the solid at the surface depends on the orientation of the surface adjacent grains (Figure **6-3**): it is concluded that both the surface nitrogen content and the nitrided depth decrease with increasing orientation factor. It is noted that similar observations have been made for austenitic steel (e.g. [26, 27]).

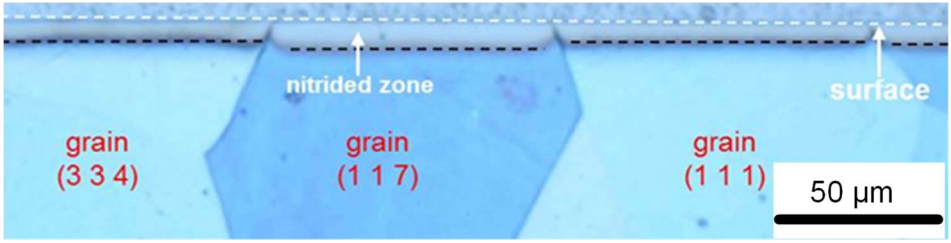

Figure 6-2. Light optical macrograph taken from the cross-section of nitrided Ni-5 at.% Ti alloy nitrided at 400°C for 65 h using r_N= 500 atm $^{-1/2}$. Thickness of the expanded austenite layer is different for differently oriented grains. The thickness of the expanded austenite layers developed in (334), (117) and (111) oriented grains are 9.8 µm, 13.2 µm and 9.2 µm, respectively.

6.4.1.2. Fe-Cr (bcc) specimens

EPMA measurements carried out *on* the surface of a 3h nitrided Fe-4.5 at.% Cr specimen (Figure **6-4**) indicate that the nitrogen surface content is different for different surface adjacent grains of this ferritic specimen: The lowest surface nitrogen content is observed for surface adjacent grains with a (111) plane parallel to the surface (Γ=0.33).

The crystallographic orientation of each surface adjacent grain with respect to the surface was determined by EBSD from the surface of nitrided specimens and expressed by the orientation factor, Γ_{hkl}. Thus, the quantitative relationship between the nitrogen content in the solid at the surface as a function of the orientation factor was determined for specimens nitrided for different times. The results are shown in Figure **6-5**. Evidently, the surface nitrogen content decreases with increasing orientation factor. With increasing nitriding time, a saturation level of N is approached and at the same time, the differences between the surface nitrogen contents for the differently oriented grains reduce (compare also Figure **6-6**(a) and (b); see section 6.5 for discussion).

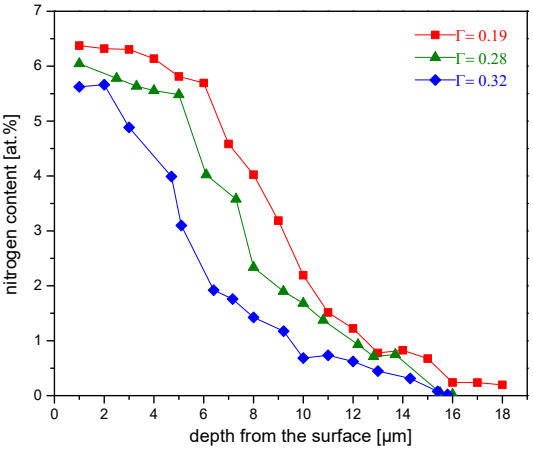

Figure 6-3. Nitrogen-depth profiles measured by EPMA for differently oriented grains (with the different orientation factors (Γ)) on a cross-section of a Ni-5 at.% Ti specimen nitrided for 65 h at 400°C using r_N= 500 atm $^{-1/2}$. Both the surface N content and the nitrided zone depth are different for differently oriented grains.

Several nitrogen-concentration depth profiles were determined by EPMA for differently oriented grains, on cross-sections of Fe-4.5 at.% Cr specimens nitrided for 1 h and 30 h (Figure **6-6**). According to Figure **6-6**(a), the depth of the nitrided zone is larger for the grain with a (100) lattice plane (closely) parallel to the surface (Γ=0.05) as compared to the grain with a (111) lattice plane (closely) parallel to the surface (Γ=0.31). As for the (fcc) Ni-Ti specimens, it can be concluded that also for the (bcc) Fe-Cr specimens, both the surface N content and the nitrided depth decreases with increasing orientation factor. This is the first time that this effect has been observed for ferritic specimens.

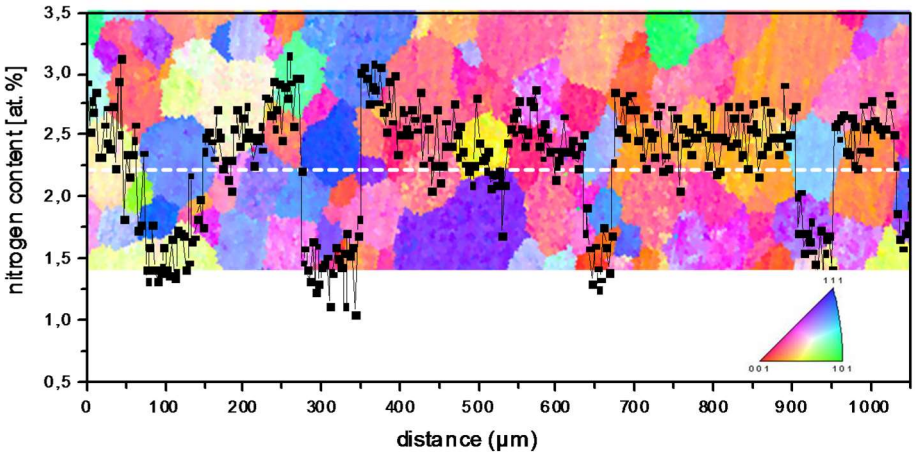

Figure 6-4. EPMA and EBSD (with incorporated corresponding [001] inverse pole figure (IPF)) measurements performed on the surface of a nitrided Fe-4.5 at.% Cr specimen (450°C, r_N= 0.1 $atm^{-1/2}$ for 3h). The dotted white line shows the line scan of EPMA measurement. Nitrogen content is low in grains with blue color (i.e. with the (111) plane parallel to the surface).

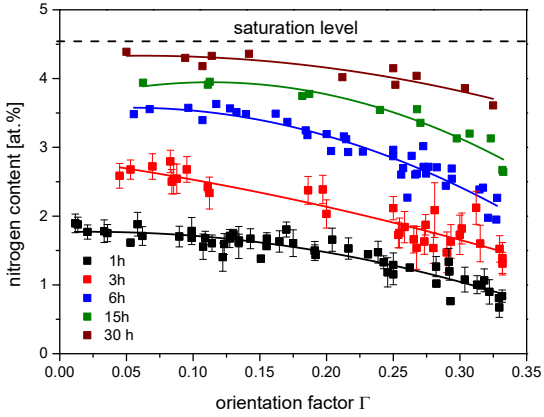

Figure 6-5. Nitrogen content measured on the surface of various grains of Fe-4.5 at.% Cr as a function of the orientation factor of the corresponding grains, as measured from specimen nitrided for different times. Nitriding experiments were performed at 450°C and r_N=0.1 $atm^{-1/2}$ for 1 h, 3 h, 6 h, 15 h and 30 h. Single N content for each grain was obtained by averaging EPMA data points measured within each grain (measured points on the grain boundaries were neglected; nucleation of precipitates is faster at grain boundaries as compared to areas far from grain boundaries). To exemplify the error of the measured averaged N content for each grain, error bars for two nitriding times (1 h and 3 h) have been shown. The polynomial fits have been given only to guide the eye. Evidently, the surface N content decreases with increasing orientation factor.

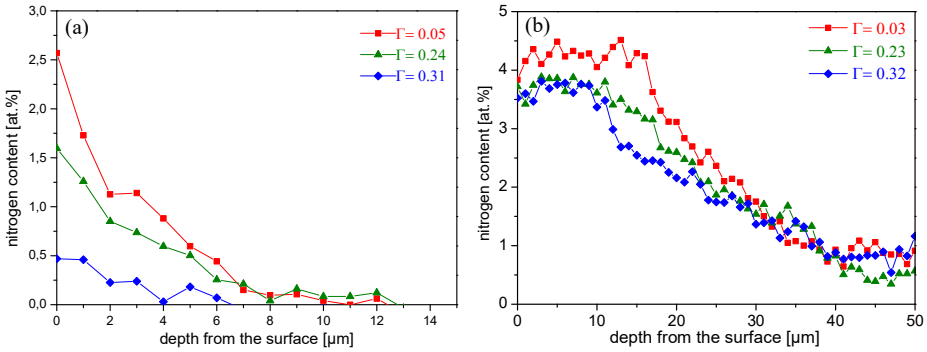

Figure 6-6. Nitrogen-depth profiles measured for differently oriented grains (with the different orientation factors (Γ)) on the cross-section of a Fe-4.5 at.% Cr specimen nitrided for a) 1 h and b) 30 h. Both the surface N content and the nitrided zone depth are different for differently oriented grains.

6.4.2. Dependence of residual stress on crystallographic orientation of surface grains

Values of the strains $\varepsilon_{\perp}(hkl)$ for grains with (100) lattice planes and grains with (111) lattice planes parallel to the surface (i.e. a (100) set and a (111) set) of a 65 h nitrided Ni-5 at.% Ti specimen and for grains with (100) lattice planes and grains with (211) lattice planes parallel to the surface (i.e. a (100) set and a (211) set) of a 1 h nitrided Fe-4.5 at.% Cr specimen have been determined from $d_{\perp}(hkl)$ and $d_0(hkl)$ according to Eq. (9). Values of $d_{\perp}(hkl)$ as measured from the positions of the intensity maxima of the (200) and (111) surface adjacent expanded austenite component reflections in the X-ray diffractogram of the 65 h nitrided Ni-Ti specimen (see Fig. 5b in [31]), are also shown in Table **6-1**. Values of $d_{\perp}(hkl)$, lattice spacings as measured from the positions of the intensity maxima of the (200) and (211) ferrite reflections in the X-ray diffractogram of the 1 h nitrided Fe-Cr specimen, are also shown in Table **6-2**. Values of $d_0(hkl)$ must represent a (hypothetical) homogenous specimen which is devoid of the planar state of stress. Values of $d_0(hkl)$ have been calculated for the Ni-Ti and Fe-Cr specimens as follows:

6.4.2.1. Ni-Ti (fcc) specimens

Values of $d_0(hkl)$ for a homogenous, stress free specimen, containing the same amount of dissolved N and dissolved Ti as in the matrix of the nitrided region of the surface grains of the heterogeneously nitrided specimen, have been calculated as follows:

$$d_0(hkl) = d_{\text{pure Ni}}(hkl) + \Delta d_{\text{dis-N}}(hkl) + \Delta d_{\text{dis-Ti}}(hkl) \quad (6\text{-}10)$$

where $d_{\text{pure Ni}}(hkl)$ is the lattice spacing of pure Ni [54] and $\Delta d_{\text{dis-N}}(hkl)$ and $\Delta d_{\text{dis-}}(hkl)$ are the lattice-spacing changes of pure Ni due to dissolved N and dissolved Ti, respectively.

Table 6-1. Values used for the calculation of $\varepsilon_\perp$ (strain in the surface-normal direction, Eq. (6-9)) for grains with (100) lattice planes and for grains with (111) lattice planes parallel to the surface of the 65 h nitrided Ni-5 at.% Ti specimen. The error in the lattice-spacing values (column 1), obtained by fitting the measured diffractograms, is ± 0.0001 Å.

(hkl)	$d_\perp$ (Å)	$d_{\text{pure Ni}}$ (Å)	$\Delta d_{\text{dis-N}}$ (Å)	$\Delta d_{\text{dis-Ti}}$ (Å)	$d_\circ$ (Å)
100	1.8250	1.7619	0.0372	0.0050	1.8041
111	2.0817	2.0345	0.0319	0.0058	2.0722

Table 6-2. Values used for the calculation of $\varepsilon_\perp$ (strain in the surface-normal direction, Eq. (6-9)) for grains with (100) lattice planes and for grains with (211) lattice planes parallel to the surface of the 1 h nitrided Fe-4.5 at.% Cr specimen. The error in the lattice-spacing values (column 1), obtained by fitting the measured diffractograms, is ±0.0001 Å.

(hkl)	$d_\perp$ (Å)	$d_{\text{pure Fe}}$ (Å)	$\Delta d_{\text{dis-N}}$ (Å)	$\Delta d_{\text{dis-}}$ (Å)	Δd_h (Å)	$d_\circ$ (Å)
100	1.4442	1.4332	0.0004	0.0008	0.0034	1.4378
211	1.1755	1.1702	0.0002	0.0008	0.0010	1.1722

For calculation of $\Delta d_{\text{dis-N}}(hkl)$ for the (100) and (111) sets, the amounts of dissolved nitrogen atoms in the Ni-rich matrix of these two sets are required. The average nitrogen contents measured in the nitrided region (thickness about 6 μm) of a (100) grain and in the nitrided region (thickness about 4 μm) of a (111) grain of the specimen nitrided for 65 h, as determined by EPMA, are 6.2 at.% and 4.6 at.%, respectively (see Figure **6-3**: the red curve corresponds to a (100) grain and the blue curve corresponds to a (111) grain). The corresponding changes of the Ni-lattice spacing, $\Delta d_{\text{di N}}$, for the (100) and (111) sets follow from a lattice-parameter increase of $+0.012$ Å per at.% of dissolved N [31].

The values of $\Delta d_{\text{dis-Ti}}(hkl)$ for the (100) and (111) sets, for 5 at.% Ti dissolved in Ni matrix, follow from a lattice-parameter increase of $+0.0020$ Å per at.% of dissolved Ti [55].

6.4.2.2. Fe-Cr (bcc) specimens

Values of $d_0(hkl)$ for a homogenous specimen, devoid of the planar state of stress, containing the same amounts of CrN precipitates, dissolved N and (remaining) dissolved Cr as in the matrix of the nitrided region of the surface grains of the heterogeneously nitrided specimen, have been calculated as follows:

$$d_0(hkl) = d_{\text{pure Fe}}(hkl) + \Delta d_{\text{dis- N}}(hkl) + \Delta d_{\text{dis-}}\ (hkl) + \Delta d_h(hkl) \qquad (6\text{-}11)$$

where $d_{\text{pure Fe}}(hkl)$ is the lattice spacing of pure Fe [54] and $\Delta d_{\text{dis- N}}(hkl)$ and $\Delta d_{\text{dis-C}}\ (hkl)$ are the lattice -spacing changes of pure Fe due to dissolved N and (remaining) dissolved Cr in the matrix, respectively. $\Delta d_h(hkl)$ represents the lattice-spacing change due to a hydrostatic component of stress (see below).

For calculation of $\Delta d_{\text{dis N}}(hkl)$ for the (100) and (211) sets, the amounts of dissolved nitrogen atoms in the ferrite matrix of these two sets are required. The maximum amount of dissolved nitrogen after complete nitriding of an Fe-4.5 at.% Cr specimen (implying all Cr has precipitated) at 450°C and r_N= 0.1 atm$^{-0.5}$ is 0.42 at.% (as deduced from weight-uptake measurements as described in Ref. [52]). The average nitrogen contents measured in the nitrided region of a (100) grain and in the nitrided region of a (211) grain of the specimen nitrided for 1 h, as determined by EPMA, are 1.4 at.% and 0.7 at.%, respectively (see Figure **6-6**(a): the red curve corresponds to a (100) grain and the green curve corresponds to a (211) grain). Correspondingly, the amounts of dissolved N in the surface region of the (100) grain and in the surface region of the (211) grain are now estimated as [(1.4/(4.5+0.42))×0.42) at.%]=0.12 at.% and [(0.7/(4.5+0.42))×0.42) at.%]=0.06 at.%, respectively. The corresponding changes of the ferrite-lattice spacing, $\Delta d_{\text{dis- N}}$ for the (100) and (211) sets, follow from a lattice-parameter increase of $+0.0079$ Å per at.% of dissolved N [56].

For calculation of $\Delta d_{\text{dis- Cr}}(hkl)$ for the (100) and (211) sets, the amounts of remaining dissolved Cr in the ferrite matrix of these two sets are required. These data can be obtained by subtracting the Cr content contributing to the CrN precipitation from the total Cr content of the alloy (4.5 at.%). Thus, the amounts of remaining dissolved Cr in the surface regions of the (100) and the (211) grains are 3.2 at.% and 3.9 at.%, respectively. The corresponding changes of the ferrite-lattice spacing , $\Delta d_{\text{dis- Cr}}$ for the (100) and (211) sets follow from a lattice-parameter increase of $+0.0005$ Å per at.% of dissolved Cr [57].

The nitrided regions contain tiny, misfitting coherent CrN precipitates which evoke a (tensile) hydrostatic stress component in the ferrite matrix [52, 58], also in the reference specimen, which

leads to a corresponding change of the lattice spacing, $\Delta d_{\mathrm{h}}(hkl)$. Therefore, in order to determine the sole effect of the stress parallel to the surface as caused by the macroscopic misfit of nitrided case and unnitrided core in the actual heterogeneously nitrided specimen, $\Delta d_{\mathrm{h}}(hkl)$ has to be incorporated in the calculation of $d_0(hkl)$ (see Eq.(6-11)). For the current case (coherent precipitates of CrN in the ferrite matrix), $\Delta d_{\mathrm{h}}(hkl)$ can be straightforwardly calculated using the model described in Ref. [52]. To this end, the average amount of CrN precipitates in the nitrided regions of the surface adjacent grains with (100) and (211) planes parallel to specimen surface must be known. These data follow from the nitrogen content contributing to the CrN precipitation (i.e. the total measured nitrogen content minus the amount of dissolved nitrogen; see above) in the nitrided regions of the (100) grains and the (211) grains: 1.28 at.% N for the (100) grains and 0.64 at.% N for the (211) grains.

The thus determined values of $d_{\mathrm{pure\,Ni}}(hkl)$, $\Delta d_{\mathrm{dis-\,N}}(hkl)$, $\Delta d_{\mathrm{dis-Ti}}(hkl)$ and finally $d_0(hkl)$ for the (100) and (111) sets of Ni-Ti specimen are shown in Table **6-1**. The thus determined values of $d_{\mathrm{pure\,Fe}}(hkl)$, $\Delta d_{\mathrm{dis-\,N}}(hkl)$, $\Delta d_{\mathrm{dis-Cr}}(hkl)$, $\Delta d_{\mathrm{h}}(hkl)$ and finally $d_0(hkl)$ for the (100) and (211) sets of Fe-Cr specimen are shown in Table **6-2**.

The elastic strains $\varepsilon_{\perp}(hkl)$ can now be calculated applying Eq. (6-9). The results have been gathered in Table **6-3**, together with the corresponding values of $1/(2S_{12}^{xyz}(hkl))$ (calculated for pure nickel and iron according to Eq. (6-7)) and the values of the acting biaxial stress obtained by use of Eq. (6-6). The finally resulting values of the equilibrium N solubility ratio, $C_{N,eq}^{\sigma\neq 0}/C_{N,eq}^{\sigma=0}$ (calculated by application of Eq. (6-5)), for the (100) and (111) sets of the Ni-Ti specimen and for the (100) and (211) sets of Fe-Cr specimen have been given in the last column of Table **6-3**. It is remarked that these results should be considered to be of at most semi quantitative in view of the assumptions made (see section 6.2).

It follows that the larger value of equilibrium N solubility is predicted (from the determined stress value) to occur for grains with {100} planes parallel to the surface of Ni-Ti and Fe-Cr specimens, as compared to grains with {211} or {111} planes parallel to the specimen's surface. This well agrees with the experimental observations.

6.5. General discussion

The results presented in sections 6.4.1 and 6.4.2. indicate that the stress and the surface nitrogen solubility in both nitrided fcc Ni-Ti and nitrided bcc Fe-Cr alloys depend on the crystallographic orientation of the surface adjacent grains, such that with increasing value of Γhkl, the stress and the surface nitrogen concentration decrease. Thereby, the correspondence of stress and equilibrium nitrogen solubility for a (hkl) set, as described by Eq. (6-5), is experimentally validated qualitatively.

Table 6-3. Values used for calculation of equilibrium nitrogen ratio (Eq. (6-5)) for grains with (100) lattice planes and grains with (111) lattice planes parallel to the surface of the 65 h nitrided Ni-5 at.% Ti specimen and for grains with (100) lattice planes and grains with (211) lattice planes parallel to the surface of the 1 h nitrided Fe-4.5 at.% Cr specimen. For calculation of equilibrium N ratio (Eq. (6-5)), the partial molar volume of nitrogen in iron ($\bar{V}_N$) was deduced from the expansion of the ferrite lattice due to nitrogen dissolution [61] as 5.12 cm^3/mol and the partial molar volume of nitrogen in nickel was deduced from the expansion of the Ni lattice due to nitrogen dissolution [31] as 6.73 cm^3/mol.

alloy	(*hkl*)	$\varepsilon_\perp$	$1/(2S_{12}^{xyz})$ (GPa)	$\sigma_{//}$ (MPa)	$\frac{C_{N,eq}^{\sigma\neq 0}}{C_{N,eq}^{\sigma=0}}$
Ni-5 at.% Ti	$(100)_{Ni}$	0.0116	-171	-1984	0.2
	$(111)_{Ni}$	0.0046	-626	-2880	0.1
Fe- 4.5 at.% Cr	$(100)_{Fe}$	0.0045	-177	-797	0.6
	$(211)_{Fe}$	0.0028	-384	-1075	0.5

A consequence of the proposed interpretation of the current experimental results is that in a *homogeneously* nitrided specimen, i.e. without a biaxial state of stress imposed by the misfit of nitrided case and unnitrided core (as in the heterogeneously nitrided specimens considered until now), the results for nitrogen surface concentration should be the same for the different (*hkl*) sets.

This prediction was verified by the following experiment: a thin foil of Fe-2 at.% Cr (of section 6.3.1) alloy was homogeneously nitrided (i.e. the same amount of N occurs at all depths). A thin foil specimen of modest Cr content shows so-called, "weak Me-N interaction" and as a consequence, the specimen is gradually enriched in N simultaneously at all depths [1, 59]. The thus obtained homogeneously nitrided thin foil with no residual macrostress (as verified by $\sin^2\psi$ stress measurement [45] performed in this project) indeed showed the absence of surface-grain orientation dependence of the surface nitrogen content for two grains crossing the specimen thickness and of largely different orientations (Γ=0.02 and Γ=0.30); see EPMA and EBSD results shown in Figure **6-7**, thereby providing full support for the interpretation offered above.

It is noted that the decrease upon continued nitriding of the differences between the surface nitrogen contents for the differently oriented surface adjacent grains, as shown in Figure **6-5** and Figure **6-6**(a) and (b), is fully compatible with the present explanation: towards specimen homogenization, i.e. for increasing nitriding time, the residual stress in the surface region naturally decreases and thereby the difference in stress level of the (*hkl*) sets also decreases.

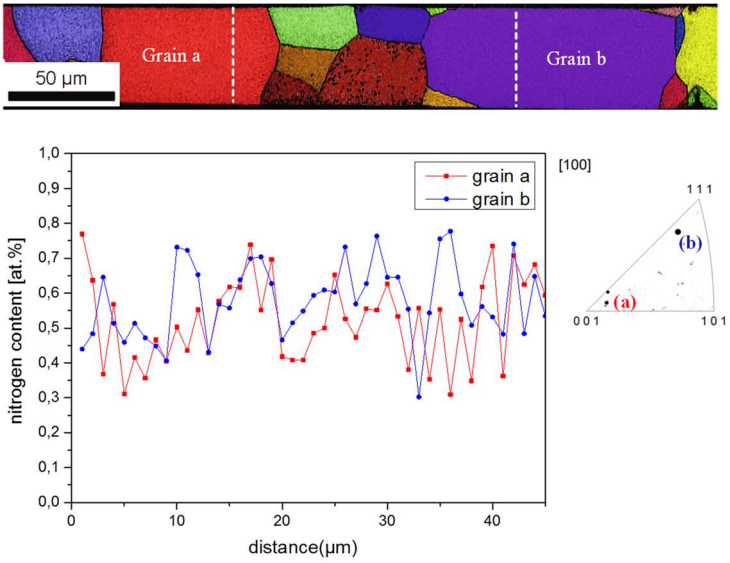

Figure 6-7. N-depth profiles measured along two grains with largely different orientations (with respect to the surface of the specimen; Γ=0.02 and Γ=0.30) on the cross-section of nitrided Fe- 2at.% Cr thin foil (450°C, r_N=0.1 atm $^{-1/2}$and 216 h). EBSD orientation map and [100] inverse pole figure (IPF) were also recorded.

6.6. Conclusions

The extent of nitriding (surface nitrogen concentration and nitrided depth) depends on the crystallographic orientation of the surface grains of the substrate. This effect not only was observed upon nitriding of austenitic (Ni-Ti) solid solutions but, for the first time, also upon nitriding of ferritic (Fe-Cr) solid solutions.

The effect could be ascribed to the occurrence of a state of residual planar stress invoked in the nitrided surface region:

(i) The value of this stress parallel to the surface is different for grains of crystallographic orientations different with respect to the surface.

(ii) A simple thermodynamic theory relates the values of stress parallel to the surface to the change of the equilibrium solubility of nitrogen.

In the absence of stress, as holds for homogenously nitrided specimens, no differences between the variously oriented surface grains with respect to their equilibrium solubility of nitrogen are expected and do not occur indeed.

Acknowledgements

The authors thank Dr. E. Bischoff for assistance with the EBSD measurements, Mrs. S. Haug for assistance with the EPMA experiments, Mr. P. Kress for assistance with the nitriding experiments and T. Steiner for assistance with analyzing the X-ray diffractograms.

References

[1] E.J. Mittemeijer. Fundamentals of Nitriding and Nitrocarburizing. in: Dossett J, Totten GE, (Eds.). ASM Handbook, vol. 4A. Steel Heat Treating Fundamentals and Processes, 2013. pp. 619-646.

[2] D.H. Jack, K.H. Jack. Invited Review - Carbides and Nitrides in Steel, Materials Science and Engineering 11 (1973) 1-27.

[3] B. Mortimer, P. Grieveson, K.H. Jack. Precipitation of Nitrides in Ferritic Iron Alloys Containing Chromium, Scandinavian Journal of Metallurgy 1 (1972) 203-209.

[4] E.J. Mittemeijer, A.B.P. Vogels, P.J. Vanderschaaf. Morphology and Lattice-Distortions of Nitrided Iron and Iron-Chromium Alloys and Steels, Journal of Materials Science 15 (1980) 3129-3140.

[5] R.E. Schacherl, P.C.J. Graat, E.J. Mittemeijer. Gaseous nitriding of iron-chromium alloys, Zeitschrift Fur Metallkunde 93 (2002) 468-477.

[6] M. Sennour, P.H. Jouneau, C. Esnouf. TEM and EBSD investigation of continuous and discontinuous precipitation of CrN in nitrided pure Fe-Cr alloys, Journal of Materials Science 39 (2004) 4521-4531.

[7] G. Miyamoto, A. Yonemoto, Y. Tanaka, T. Furuhara, T. Maki. Microstructure in a plasma-nitrided Fe–18 mass% Cr alloy, Acta Materialia 54 (2006) 4771-4779.

[8] S.S. Hosmani, R.E. Schacherl, E.J. Mittemeijer. Nitrogen absorption by Fe-1.04at.%Cr alloy: uptake of excess nitrogen, Journal of Materials Science 43 (2008) 2618-2624.

[9] E.J. Mittemeijer, M.A.J. Somers. Thermochemical Surface Engineering of Steels Woodhead Publishing, 2015.

[10] H.H. Podgurski, H.E. Knechtel. Nitrogenation of Fe-Al Alloys .1. Nucleation and Growth of Aluminum Nitride, Transactions of the Metallurgical Society of AIME 245 (1969) 1595-&.

[11] J.H. Driver, J.M. Papazian. Electron and Field-Ion Metallography of Zones in Nitrided Fe-Mo Alloys, Acta Metallurgica 21 (1973) 1139-1149.

[12] H.H. Podgurski, F.N. Davis. Thermochemistry and nature of nitrogen absorption in nitrogenated Fe-Ti alloys, Acta Metallurgica 29 (1981) 1-9.

[13] P.M. Hekker, H.C.F. Rozendaal, E.J. Mittemeijer. Excess Nitrogen and Discontinuous Precipitation in Nitrided Iron Chromium-Alloys, Journal of Materials Science 20 (1985) 718-729.

[14] N.E.V. Diaz, S.S. Hosmani, R.E. Schacherl, E.J. Mittemeijer. Nitride precipitation and coarsening in Fe-2.23 at.% V alloys: XRD and (HR)TEM study of coherent and incoherent diffraction effects caused by misfitting nitride precipitates in a ferrite matrix, Acta Materialia 56 (2008) 4137-4149.

[15] S.R. Meka, E. Bischoff, S.S. Hosmani, E.J. Mittemeijer. Interrelationships of defects, nitride modification and excess nitrogen in nitrided Fe-4.75 at.% Al alloy, International Journal of Materials Research 105 (2014) 1057-1066.

[16] O. Ozturk, D.L. Williamson. Phase and Composition Depth Distribution Analyses of Low-Energy, High-Flux N-Implanted Stainless-Steel, Journal of Applied Physics 77 (1995) 3839-3850.

[17] G.A. Collins, R. Hutchings, K.T. Short, J. Tendys, X. Li, M. Samandi. Nitriding of austenitic stainless steel by plasma immersion ion implantation, Surface and Coatings Technology 74-75 (1995) 417-424.

[18] D.L. Williamson, J.A. Davis, P.J. Wilbur. Effect of austenitic stainless steel composition on low-energy, high-flux, nitrogen ion beam processing, Surface & Coatings Technology 104 (1998) 178-184.

[19] Y. Sun, X.Y. Li, T. Bell. X-ray diffraction characterisation of low temperature plasma nitrided austenitic stainless steels, Journal of Materials Science 34 (1999) 4793-4802.

[20] S. Mandl, B. Rauschenbach. Nitrogen diffusion in austenitic stainless steel and the formation of expanded austenite, Defects and Diffusion in Metals Iii 188-1 (2001) 125-136.

[21] T. Christiansen, M.A.J. Somers. Low temperature gaseous nitriding and carburising of stainless steel, Surface Engineering 21 (2005) 445-455.

[22] T. Czerwiec, H. He, G. Marcos, T. Thiriet, S. Weber, H. Michel. Fundamental and Innovations in Plasma Assisted Diffusion of Nitrogen and Carbon in Austenitic Stainless Steels and Related Alloys, Plasma Processes and Polymers 6 (2009) 401-409.

[23] A. Martinavicius, G. Abrasonis, W. Moller, C. Templier, J.P. Riviere, A. Declemy, Y. Chumlyakov. Anisotropic ion-enhanced diffusion during ion nitriding of single crystalline austenitic stainless steel, Journal of Applied Physics 105 (2009).

[24] J.C. Stinville, P. Villechaise, C. Templier, J.P. Riviere, M. Drouet. Lattice rotation induced by plasma nitriding in a 316L polycrystalline stainless steel, Acta Materialia 58 (2010) 2814-2821.

[25] H. Dong. S-phase surface engineering of Fe-Cr, Co-Cr and Ni-Cr alloys, International Materials Reviews 55 (2010) 65-98.

[26] D. Wu, H. Kahn, J.C. Dalton, G.M. Michal, F. Ernst, A.H. Heuer. Orientation dependence of nitrogen supersaturation in austenitic stainless steel during low-temperature gas-phase nitriding, Acta Materialia 79 (2014) 339-350.

[27] H. Kahn, G.M. Michal, F. Ernst, A.H. Heuer. Poisson Effects on X-Ray Diffraction Patterns in Low-Temperature-Carburized Austenitic Stainless Steel, Metallurgical and Materials Transactions a-Physical Metallurgy and Materials Science 40A (2009) 1799-1804.

[28] T. Christiansen, M.A.J. Somers. On the crystallographic structure of S-phase, Scripta Materialia 50 (2004) 35-37.

[29] C. Leroy, T. Czerwiec, C. Gabet, T. Belmonte, H. Michel. Plasma assisted nitriding of Inconel 690, Surface & Coatings Technology 142 (2001) 241-247.

[30] H. He, T. Czerwiec, C. Dong, H. Michel. Effect of grain orientation on the nitriding rate of a nickel base alloy studied by electron backscatter diffraction, Surface & Coatings Technology 163 (2003) 331-338.

[31] M. Fonović, A. Leineweber, O. Robach, E.A. Jägle, E.J. Mittemeijer. The Nature and Origin of “Double Expanded Austenite” in Ni-Based Ni-Ti Alloys Developing Upon Low Temperature Gaseous Nitriding, Metallurgical and Materials Transactions A: Physical Metallurgy and Materials Science 46 (2015) 4115-4131.

[32] X.Y. Li, N. Habibi, T. Bell, H. Dong. Microstructural characterisation of a plasma carburised low carbon Co - Cr alloy, Surface Engineering 23 (2007) 45-51.

[33] A. Martinavicius, G. Abrasonis, W. Moller. Influence of crystal orientation and ion bombardment on the nitrogen diffusivity in single-crystalline austenitic stainless steel, Journal of Applied Physics 110 (2011).

[34] J.F. Nye. Physical Properties of Crystals: Their Representation by Tensors and Matrices, Oxford University Press, Oxford, 1985.

[35] M. Grunze, F. Bozso, G. Ertl, M. Weiss. Interaction of Ammonia with Fe(111) and Fe(100) Surfaces, Applied Surface Science 1 (1978) 241-265.

[36] J. Mc Allister, R.S. Hansen. Catalytic Decomposition of Ammonia on Tungsten (100), (110), and (111) Crystal Faces, Journal of Chemical Physics 59 (1973) 414-422.

[37] T. Christiansen, K.V. Dahl, M.A.J. Somers. Nitrogen diffusion and nitrogen depth profiles in expanded austenite: experimental assessment, numerical simulation and role of stress, Materials Science and Technology 24 (2008) 159-167.

[38] H. He, J.X. Zou, C. Dong, T. Czerwiec, H. Michel. Stress induced anisotropic diffusion during plasma-assisted nitriding of a Ni-based alloy, Pricm 5: The Fifth Pacific Rim International Conference on Advanced Materials and Processing, Pts 1-5 475-479 (2005) 3669-3672.

[39] E.J. Mittemeijer, J.T. Slycke. Chemical Potentials and Activities of Nitrogen and Carbon Imposed by Gaseous Nitriding and Carburising Atmospheres, Surface Engineering 12 (1996) 152-162.

[40] J.C.M. Li, R.A. Oriani, L.S. Darken. Thermodynamics of Stressed Solids, Zeitschrift Fur Physikalische Chemie-Frankfurt 49 (1966) 271-&.

[41] H.A. Wriedt, R.A. Oriani. Effect of tensile and compressive elastic stress on equilibrium hydrogen solubility in a solid, Acta Metallurgica 18 (1970) 753-760.

[42] R.A. Swalin. Thermodynamics of Solids. 2nd ed. ed., Wiley, New York, 1972.

[43] N.E. Vives Diaz, R.E. Schacherl, L.F. Zagonel, E.J. Mittemeijer. Influence of the microstructure on the residual stresses of nitrided iron-chromium alloys, Acta Materialia 56 (2008) 1196-1208.

[44] I.C. Noyan, J.B. Cohen. Residual Stress measurement by Diffraction and Interpretation, Springer-Verlag, New York, 1987.

[45] U. Welzel, J. Ligot, P. Lamparter, A.C. Vermeulen, E.J. Mittemeijer. Stress analysis of polycrystalline thin films and surface regions by X-ray diffraction, Journal of Applied Crystallography 38 (2005) 1-29.

[46] J. Turley, G. Sines. Anisotropic behaviour of the compliance and stiffness coefficients for cubic materials, Journal of Physics D: Applied Physics 4 (1971) 1731.

[47] M.K.A. Koker, U. Welzel, E.J. Mittemeijer. Elastic mechanical grain interactions in polycrystalline materials; Analysis by diffraction-line broadening, Philosophical Magazine 93 (2013) 2967-2994.

[48] M.K.A. Koker, U. Welzel, E.J. Mittemeijer. Measurement of X-ray diffraction-line broadening induced by elastic mechanical grain interaction, Journal of Applied Crystallography 47 (2014) 391-401.

[49] U. Welzel, E.J. Mittemeijer. Diffraction stress analysis of macroscopically elastically anisotropic specimens: On the concepts of diffraction elastic constants and stress factors, Journal of Applied Physics 93 (2003) 9001-9011.

[50] T. Gnaupel-Herold, P.C. Brand, H.J. Prask. Accessing the Elastic Properties of Cubic Materials with Diffraction Methods, Advances in X-ray Analysis 42 (1999) 464-470.

[51] F.C. Larché, J.W. Cahn. The Interactions of Composition and Stress in Crystalline Solids, Journal of Research of the National Bureau of Standards 89 (1984) 467-500.

[52] M. Akhlaghi, T. Steiner, S.R. Meka, A. Leineweber, E.J. Mittemeijer. Lattice-Parameter Change Induced by Accommodation of Precipitates/Matrix Misfit; Misfitting Nitrides in Ferrite, Acta Materialia 98 (2015) 254-262.

[53] J.L. Pouchou, F. Pichoir. A New Model for Quantitative X-Ray-Microanalysis .2. Application to in-Depth Analysis of Heterogeneous Samples, Recherche Aerospatiale (1984) 349-367.

[54] I.J.-I.C.f.D. Data. PCPDFWIN, 2002.

[55] W.B. Pearson. in: Pearson WB, (Ed.). A Handbook of Lattice Spacings and Structures of Metals and Alloys, vol. 4. Pergamon, 1958. pp. 634.

[56] H.A. Wriedt, L. Zwell. Lattice Dilation of Alpha-Iron by Nitrogen, Transactions of the Metallurgical Society of AIME 224 (1962) 1242-&.

[57] A. Sutton, W. Hume-Rothery. The lattice spacings of solid solutions of titanium, vanadium, chromium, manganese, cobalt and nickel in α-iron, Philosophical Magazine 46 (1955) 1295-1309.

[58] M.A.J. Somers, R.M. Lankreijer, E.J. Mittemeijer. Excess Nitrogen in the Ferrite Matrix of Nitrided Binary Iron-Based Alloys, Philosophical Magazine A 59 (1989) 353-378.

[59] M.H. Biglari, C.M. Brakman, M.A.J. Somers, W.G. Sloof, E.J. Mittemeijer. On the Internal Nitriding of Deformed and Recrystallized Foils of Fe-2 at-Percent Al, Z Metallkd 84 (1993) 124-131.

[60] C.J. Smithells. Metals Reference Book. 5th edition ed., Butterworth, London, 1976.

[61] P. Ferguson, K.H. Jack. Quenched-Aging and Strain-Aging of Nitrogen-Ferrite. Proceedings of Heat Treatment `81. Londen: The Metals Society, 1983. p.158-163.

Chapter 7

Summary

The initial microstructure of the unnitrided specimen has a significant influence on the nitriding response of binary Fe-*Me* (*Me*: Mo or Al) alloys specimens. This effect was not investigated until now for the case of nitrided ternary Fe-Me_1-Me_2 alloys The role of the initial microstructure was studied upon nitriding Fe-4.1 at.% Cr-7.9 at.% Al specimens (chapter 2). To this end, the recrystallized and cold-rolled specimens were nitrided at low nitriding temperature of 400 °C. Application of such low nitriding temperature inhibits recrystallization of the cold-rolled specimen during the nitriding process, thereby exposing the role of the dislocations on the nitride-precipitation process. Nitrogen-depth profiles as measured on the cross-sections of the recrystallized and the cold-rolled specimens reveal that development of mixed precipitates occurs during nitriding of the recrystallized specimen: i.e. the development of metastable, ternary, cubic, NaCl-type $Cr_{1-x}Al_xN$ nitrides was observed. However, in the case of cold-rolled specimen, successive precipitation of binary nitrides of Al and Cr occurs. The difference in distribution of nitrogen in the nitrided regions of recrystallized and cold-rolled specimens is shown in Figure 7-1. The crystal structure of the precipitates developed in both types of specimens is of the cubic, NaCl-type. The absence of stable hexagonal AlN nitride has been attributed to the decrease of misfit-strain energy being larger than the increase of chemical energy by incorporation of Al into the developing binary CrN nitride, i.e., the nucleation barrier for the development of stable hexagonal AlN is larger than that for the development of metastable ternary $Cr_{1-x}Al_xN$ nitride. The formation of the separate binary nitrides in the cold-rolled specimens has been attributed to the role of dislocations serving as easy, heterogeneous nucleation sites.

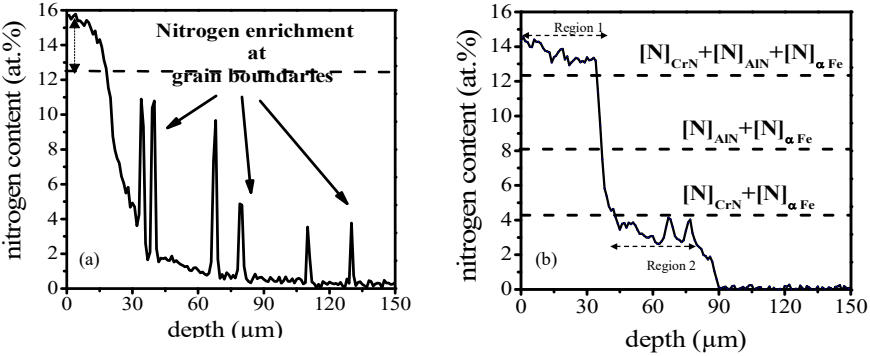

Figure 7-1. Nitrogen concentration-depth profiles (EPMA recorded from the cross-section of a) recrystallized and b) cold-rolled Fe-Cr-Al specimens nitrided for 144 h. The nitrogen taken up above the dashed line of highest level (indicated with double arrow in (a)) is called excess nitrogen. Enrichment of nitrogen at the grain boundaries in (a) depicts the heterogeneous nucleation of nitrides at the grain boundaries. Dashed horizontal lines in (b) represent the nitrogen levels expected for different possible scenarios of nitride development.

Upon precipitation of misfitting coherent nitrides during nitriding of thin-foils of binary Fe-Me (Me: Cr and V) alloys, a hydrostatic tensile lattice-stain component results from the elastic accommodation of volume misfit of nitrides and ferrite matrix. The change of the ferrite-matrix lattice parameter can be traced upon precipitation of the nitrides by X-ray diffraction measurements. The theory originally developed for the case of imperfections (by Eshelby) in solids can be applied for quantitatively describing the lattice-parameter changes of the matrix, the nitrides and the aggregate (matrix+ nitrides) as function of volume fraction and type of nitrides. As dissolved nitrogen has also an extra influence on expansion of matrix lattice, the dissolved nitrogen atoms were driven out of the specimen by applying denitriding (i.e., hydrogen reduction), as has been shown schematically in Figure 7-2. The coherent diffraction of the aggregate, consisting of matrix and coherent precipitates, occurred for nitrided Fe-Me (Me: Cr and V) alloys. Good agreement between the experimental results and the model predictions was realized (Figure 7-2) (chapter 3). Upon aging of the homogenously nitrided Fe-Cr thin-foils, backshift of the diffraction-peak maximum towards higher diffraction angles has been observed (chapter 4). Upon aging of the nitrided Fe-Cr alloys, coarsening of CrN nitrides leads to change of the misfit-accommodation mode from elastic to plastic. This misfit relaxation can occur gradually during continues coarsening or can occur abruptly upon discontinuous coarsening of CrN nitrides. The tracing of the misfit-relaxation process is possible applying X-ray diffraction.

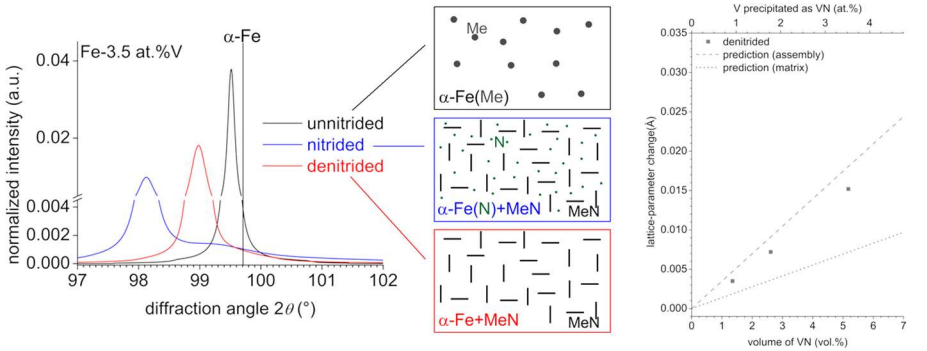

Figure 7-2. The change of X-ray reflection maximum due to nitriding and subsequent denitriding. Comparison of model predicted and experimental data for the difference of the lattice parameter of denitrided Fe-V specimens and the lattice parameter of pure, single-phase ferrite as function of the amount of precipitated nitride phase.

In general, it is possible to predict the change of the lattice parameters of the matrix, the second-phase and the assembly in two-phase systems using Eshelby model. The comparison between the change of lattice parameters experimentally obtained by X-ray diffraction and the change of lattice parameter theoretically reveals good agreement. For applying the model, it is important to indicate the type of diffraction (coherent/incoherent) and the type of misfit (precipitation induced misfit/thermal misfit). An overview on such misfit induced changes of lattice parameters in two phase systems has been presented in chapter 5 and has been summarized in Table 7-1.

Table 7-1. Types of systems consisting of a matrix with misfitting second-phase particles, categorized on the basis of the type of elastically accommodated misfit (column 2) and of the type of precipitate/matrix diffraction (column 3).

type of system	type of elastically accommodated misfit	type of precipitate/ matrix diffraction	case studies
1	transformation misfit	coherent	nitrided Fe-Me alloys Co clusters in decomposed Cu-Co alloy
2	transformation misfit	incoherent	aged (at RT) Fe-N alloy
3	thermal misfit	incoherent	aged AlSi alloy nitrided and aged Fe-Cr alloys

The extent of the uptake of dissolved nitrogen during nitriding of ferritic Fe-4.5 at.% Cr and austenitic Ni-5 at.% Ti is a function of the crystallographic orientation of the surface grains.

Therefore, not only the surface nitrogen content, but also the nitrided depth developing on each surface grain is different from one grain to another. For cubic materials, the surface-nitrogen concentration and the nitride depth decrease upon increasing the smallest angle between the surface normal and the normal of a {100} plane of the surface grain considered. This phenomenon has been attributed to the different state of biaxial stress developing in each differently oriented surface grain due to the elastically anisotropic nature of ferrite and austenite. Because of the difference in magnitude of biaxial stress acting on the differently oriented grains, the equilibrium solubility of nitrogen in the different grains is different. As can be seen in Figure 7-3, the lowest and highest amounts of nitrogen absorption occurred for grains with their {111} and {100} planes parallel to the specimen surface, respectively (Chapter 6).

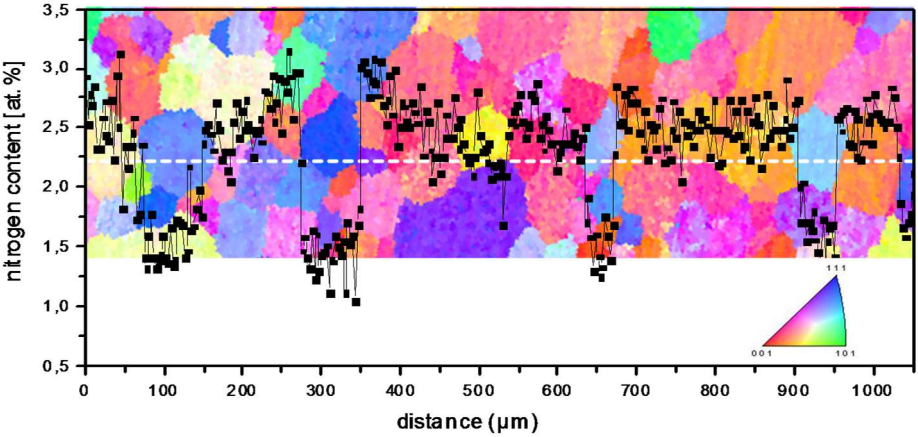

Figure 7-3. EPMA and EBSD (with incorporated corresponding [001] inverse pole figure (IPF)) measurements performed on the surface of a nitrided Fe-4.5 at.% Cr specimen (450°C, r_N= 0.1 atm$^{-1/2}$ for 3h). The dotted white line shows the line scan of EPMA measurement. Nitrogen content is low in grains with blue color (i.e. with the (111) plane parallel to the surface) and high in grains with red color (i.e., with the (100) plane parallel to the specimen surface).

Chapter 8

Zusammenfassung in deutscher Sprache

Das zu Beginn vorhandene Gefüge des unnitrierten Werkstücks hat einen bedeutenden Einfluss auf das Nitrierverhalten binärer Fe-*Me* (*Me*: Mo oder Al) Legierungen. Dieser Effekt wurde bisher nicht an ternären Fe-Me_1-Me_2-Legierungen untersucht. Die Auswirkungen des Anfangsgefüges auf das Nitrierverhalten wurde beim Nitrieren von Fe-4.1 at.% Cr-7.9 at.% Al Proben untersucht (Kapitel 2). Zu diesem Zweck wurden rekristallisierte und kaltgewalzte Proben bei einer niedrigen Nitriertemperatur von 400 °C nitriert. Die Anwendung solch niedriger Nitriertemperaturen verhindert die Rekristallisation der kaltgewalzten Proben während des Nitrierens, wodurch der Einfluss der Versetzungen auf die Nitridausscheidung sichtbar wird. An Querschliffen von rekristallisierten und kaltgewalzten Proben aufgenommene Stickstofftiefenprofile zeigen die Entstehung von gemischten Nitriden während des Nitrierens rekristallisierter Proben: das heißt, es wurde die Entstehung von metastabilen, ternären, kubischen $Cr_{1-x}Al_xN$ Nitriden mit einer Kristallstruktur vom NaCl-Typ beobachtet. Im Fall von kaltgewalzten Proben wurde jedoch die aufeinander folgende Ausscheidung von binären Al- und Cr-Nitriden beobachtet. Die unterschiedliche Stickstoffverteilung in der Nitrierschicht von rekristallisierten und kaltgewalzten Proben ist in Abbildung 8-1 gezeigt. Die Kristallstruktur der in beiden Arten von Proben gebildeten Ausscheidungen ist vom kubischen NaCl-Typ. Die Abwesenheit des stabilen hexagonalen AlN-Nitrids wird der Tatsache zugeschrieben, dass die Absenkung der Verzerrungsenergie größer ist als die Zunahme der chemischen Energie durch die Aufnahme von Al in das sich bildende binäre CrN Nitrid, d.h., die Keimbildungsbarriere zur Bildung des stabilen hexagonalen AlN ist größer als diejenige zur Bildung von metastabilem $Cr_{1-x}Al_xN$-Nitrid. Die Bildung von separaten binären Nitriden in den kaltgewalzten Proben wurde der Wirkung von Versetzungen als günstige, heterogene Keimstellen zugeordnet.

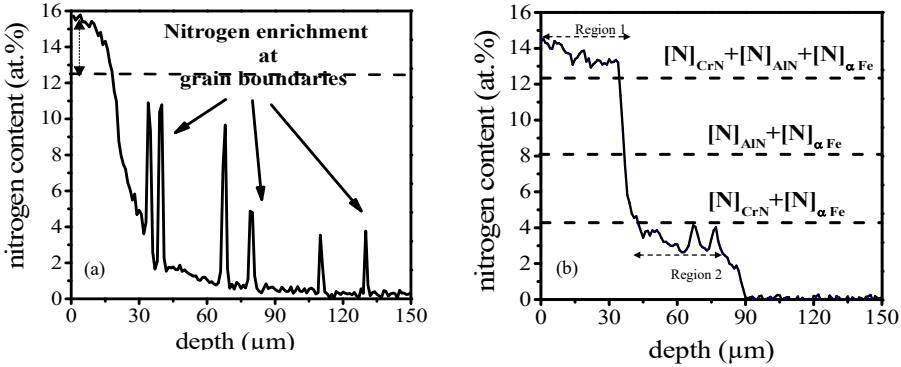

Abbildung 8-1. An Querschliffen von a) rekristallisierten und b) kaltgewalzten Fe-Cr-Al-Proben nach dem Nitrieren für 144 h aufgenommene Stickstoffgehalt-Tiefenprofile (Elektronenstrahlmikrosonden-untersuchungen, ESMA). Der oberhalb der obersten gestrichelten Linie (in a) als Doppelpfeil gezeigt) aufgenommene Stickstoff wird „Excess-Stickstoff" genannt. Anreicherung von Stickstoff an Korngrenzen in a) zeigt die heterogene Keimbildung der Nitride an Korngrenzen. Gestrichelte horizontale Linien in b) zeigen die zu erwartenden Stickstoffgehalte in verschiedenen Szenarien der Nitridbildung.

Bei der Ausscheidung von kohärenten Nitriden mit Fehlpassung während des Nitrierens von dünnen Folien binärer Fe-*Me* (*Me*: Cr und V) Legierungen resultiert eine hydrostatische Zugkomponente der Gitterdehnung durch die elastische Aufnahme der Volumenfehlpassung von Nitriden und Ferritmatrix. Die Änderung des Gitterparameters der Ferritmatrix kann während der Ausscheidung der Nitride mit Röntgenbeugungsmessungen verfolgt werden. Die ursprünglich (von Eshelby) für Fehlstellen in Festkörpern entwickelte Theorie liefert eine quantitative Beschreibung der Gitterparameteränderungen der Matrix, der Nitride und des Aggregats (Matrix + Nitride) als Funktion des Volumenanteils und der Art der Nitride. Da gelöster Stickstoff eine zusätzliche Aufweitung des Matrixgitters hervorruft, wurden die gelösten Stickstoffatome aus der Probe durch Denitrieren entfernt (d.h. Wasserstoffreduzierung), wie schematisch in Abbildung 8-2 gezeigt. Kohärente Beugung des Aggregats, bestehend aus Matrix und kohärenten Nitriden, trat bei nitrierten Fe-*Me* (*Me*: Cr und V) Legierungen auf. Eine gute Übereinstimmung der experimentellen Ergebnisse mit den Modellvorhersagen wurde gefunden (Abbildung 8-2) (Kapitel 3). Während des Alterns von homogen nitrierten Fe-Cr dünnen Folien, wurde eine Rückverschiebung der Beugungsmaxima zu höheren Beugungswinkeln beobachtet (Kapitel 4). Die während des Alterns von nitrierten Fe-Cr-Legierungen auftretende Vergröberung der CrN-Nitride verändert die Aufnahmeart der Volumenfehlpassung von elastisch zu plastisch. Diese Fehlpassungsrelaxation kann graduell durch kontinuierliche Vergröberung oder abrupt durch diskontinuierliche Vergröberung der CrN-Nitride erfolgen. Diese Fehlpassungsrelaxation kann über Röntgenbeugungsmessungen verfolgt werden.

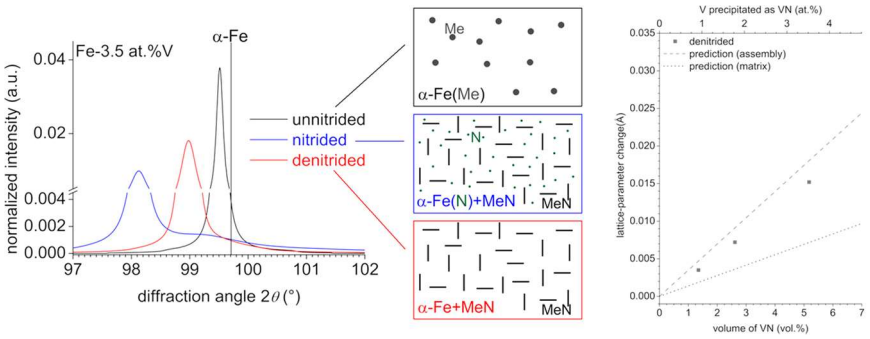

Abbildung 8-2. Die Veränderung des Röntgenreflexmaximums durch Nitrieren und anschließendes Denitrieren. Vergleich von Modellvorhersagen und experimentellen Daten der Differenz des Gitterparameters von denitrierten Fe-V Proben und des Gitterparameters von reinem, einphasigem Ferrit als Funktion der Menge an Nitridphase.

Im Allgemeinen ist es möglich, die Veränderung des Gitterparameters der Matrix, der Zweitphase und des Aggregats in Zweiphasensystemen mit Hilfe des Eshelbymodells vorherzusagen. Der Vergleich der experimentell mittels Röntgenbeugung bestimmten Gitterparameteränderung und der theoretischen Vorhersage des Gitterparameters zeigt eine gute Übereinstimmung. Für die Anwendung des Modells ist es wichtig die Art der Beugung (kohärent/inkohärent) und die Art der Fehlpassung (ausscheidungsbedingt/thermisch) anzugeben. Eine Übersicht solcher fehlpassungsinduzierter Veränderungen des Gitterparameters in Zweiphasensystemen wird in Kapitel 5 gegeben, eine Zusammenfassung zeigt Tabelle 8-1.

Tabelle 8-1. Systeme bestehend aus Matrix und Zweitphasenpartikeln mit Fehlpassung, gruppiert nach der Art des elastisch aufgenommenen Fehlpassung (Spalte 2) und der Art der Ausscheidungs/Matrix-Beugung (Spalte 3)

Art des Systems	Art der elastisch aufgenommenen Fehlpassung	Art der ausscheidungs/Matrix Beugung	Fallstudien
1	Umwandlungs-fehlpassung	kohärent	nitrierte Fe-Me Legierungen Co-Cluster in zersetzter Cu-Co Legierung
2	Umwandlungs-fehlpassung	inkohärent	Gealterte (bei RT) Fe-N Legierung
3	Thermische Fehlpassung	inkohärent	Gealterte AlSi Legierung Nitrierte und gealterte Fe-Cr Legierungen

Die Menge an Stickstoff, die während des Nitrierens von ferritischem Fe-4.5 at.% Cr und austenitischem Ni-5 at.5 Ti aufgenommen wird, ist eine Funktion der kristallographischen Orientierung der Oberflächenkörner. Daher unterscheiden sich nicht nur der Stickstoffgehalt an der Oberfläche, sondern auch die Nitriertiefe jedes Oberflächenkorns. In kubischen Materialien nehmen der Stickstoffgehalt an der Oberfläche und die Nitriertiefe mit zunehmendem Winkel zwischen Oberflächennormale und der Normale einer {100}-Ebene des jeweiligen Oberflächenkorns ab. Dieses Phänomen wurde dem sich in den unterschiedlich orientierten Oberflächenkörnern durch die elastische Anisotropie des Ferrits und Austenits unterschiedlich ausbildenden biaxialen Spannungszustand zugeordnet. Durch den Unterschied in der Höhe der auf verschieden orientierte Körner wirkenden biaxialen Spannung unterscheiden sich die Stickstoff-Gleichgewichtslöslichkeiten der jeweiligen Körner. Wie in Abbildung 8-3 gezeigt, tritt die jeweils niedrigste und höchste Stickstoffaufnahme in Körnern mit {111} und {100} Ebenen parallel zur Oberfläche auf (Kapitel 6).

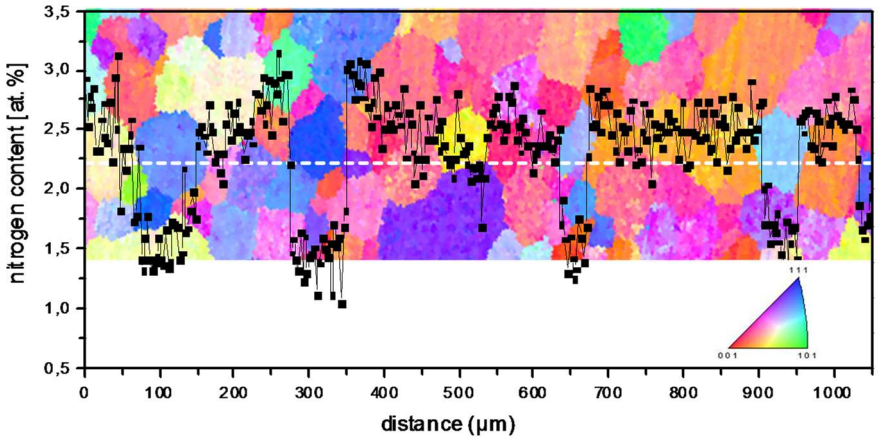

Abbildung 8-3. ESMA und EBSD (mit zugehöriger [001] inversen Polfigur (IPF)) Messungen auf der Oberfläche einer nitrierten Fe-4.5 at.% Cr Probe (450 °C, r_N=0.1 atm$^{-½}$, 3 h). Die gestrichelte weiße Linie gibt den Ort der ESMA-Linienanalyse an. Der Stickstoffgehalt ist in blauen Körnern niedrig (d.h. mit einer (111) Ebene parallel zur Oberfläche) und in roten Körnern hoch (d.h. mit einer (100) Ebene parallel zur Oberfläche).

List of publications

1. M. Akhlaghi, S.R. Meka, E. Bischoff and E.J. Mittemeijer. **Low temperature nitriding of ferritic Fe-Cr-Al alloys**, *Proceedings-European Conference on Heat Treatment and 21st IFHTSE Congress*, 2014, p 111-118, Munich, Germany (Chapter 2 of this thesis).

2. M. Akhlaghi, T. Steiner, S.R. Meka, A. Leineweber and E.J. Mittemeijer. **Lattice parameter change induced by accommodation of precipitate/matrix misfit; misfitting nitrides in ferrite**, *Acta Materialia*, Vol. 98, 2015, p. 254-262 (Chapter 3 of this thesis).

3. T. Steiner, M. Akhlaghi, S.R. Meka and E.J. Mittemeijer. **Diffraction-line shifts and broadenings in continuously and discontinuously coarsening precipitate-matrix systems; coarsening of initially coherent nitride precipitates in a ferrite matrix**, *Journal of Materials Science*, Vol. 50, 2015, p. 7075-7086 (Chapter 4 of this thesis).

4. M. Akhlaghi, T. Steiner, S.R. Meka and E.J. Mittemeijer. **Misfit induced changes of lattice parameters in two-Phase systems: coherent/incoherent precipitates in a matrix**, *Journal of Applied Crystallography*, 2015 (Chapter 5 of this thesis).

5. M. Akhlaghi, M. Jung, S.R. Meka, M. Fonovic, A. Leineweber and E.J. Mittemeijer. **Dependence of the nitriding rate of ferritic and austenitic substrates on the crystallographic orientation of surface grains; gaseous nitriding of Fe-Cr and Ni-Ti alloys,** *Philosophical Magazine*, 2015 (Chapter 6 of this thesis).

Acknowledgements

The work presented in this thesis has been performed at the Max Planck Institute for Intelligent Systems (formerly Max Planck Institute for Metals Research) and at the Institute for Materials Science, University of Stuttgart.

First of all, I would like to thank my thesis supervisor Prof. Dr. E.J. Mittemeijer for introducing me to this exciting field of nitriding and providing me the opportunity to work in his department. His commitment, guidance, encouragement and support, were a tremendous contribution for the successful completion of this thesis. I learned from him the ways to deal with scientific problems and how to solve them. His supportive attitude towards new and unusual ideas was inspiring for me. The instructive scientific discussions with him and other colleagues during regular internal meetings enhanced my specific knowledge and also my self-confidence as a female scientist, which I hope to use for my future career in science.

I would like to also express my special appreciation to Prof. Dr. J. Bill for being my second examiner (Mitberichter) for PhD examination and Prof. T. Schleid for accepting the position as the chairman (Prüfungsvorsitzender) for the PhD examination committee.

I would like to thank my daily supervisor Dr. S. Meka for his continuous cooperation, his interesting remakes and his encouragement. My special thanks to my friend and colleague T. Steiner for German translation of the summary.

I am thankful to the International Max Planck Research School for Advanced Materials for providing part of the financial support for my research and Dr. H.G. Libuda, the coordinator of IMPRS-CMS, for his kind help during my application process and during my study.

I am grateful to all friends, present and former colleagues in the department Mittemeijer, especially T. Steiner, Dr. M. Jung, Dr. H. Selg, Dr. E. Polatidis, Dr. B. Rheingans, Dr. S. Kurz and Dr. E. Jägle, for their assistance and the friendly environment which made my stay in the department pleasant and joyful. I am very grateful for all support and technical assistance I

experienced from the members of the institute. I would also like to thank all my friends outside the institute, particularly. Y. Unutulmazsoy and M. Schmidt for their helpful supports during my stay in Stuttgart.

Special thanks to my spouse and my dear friend, Reza, for his strong belief in my talents and his positive attitude towards difficulties and his endless care and support during this time. Everything which I have achieved in my life is because of my family. I am very grateful to my parents and my siblings.

Curriculum Vitae

Personal Data

Name:	Maryam Akhlaghi
Date of birth:	3rd February 1986
Place of Birth:	Tehran, Iran
Nationality:	Iranian

Education

2004-2008	**School of Metallurgy and Materials Engineering, University of Tehran, Tehran, Iran** B.Sc. in Metallurgy and Materials Engineering Thesis Title: *Stripping of D2EHPA from Fe (III) after Solvent Extraction of Zn*
2008-2010	**School of Metallurgy and Materials Engineering, University of Tehran, Tehran, Iran** M.Sc. in Materials Science and Engineering Thesis Title: *Deformation Energy of NiTi Shape Memory Alloys*

Dissertation

2012-2015	**Max Planck Institute for Intelligent Systems (formerly Max Planck Institute for Metals Research)** PhD Student Thesis Title: *Precipitation of nitrides in iron-based binary and ternary alloys; influence of defects and transformation-misfit stresses*

Erklärung über die Eigenständigkeit der Dissertation

Ich versichere, dass ich die vorliegende Arbeit mit dem Titel *Precipitation of nitrides in iron-based binary and ternary alloys; influence of defects and transformation-misfit stresses* selbständig verfasst und keine anderen als die angegebenen Quellen und Hilfsmittel benutzt habe; aus fremden Quellen entnommene Passagen und Gedanken sind als solche kenntlich gemacht.

Declaration of Authorship

I hereby certify that the dissertation entitled *Precipitation of nitrides in iron-based binary and ternary alloys; influence of defects* is entirely my own work except where otherwise indicated. Passages and ideas from other sources have been clearly indicated.

Name/Name: Maryam Akhlaghi

Unterschrift/Signed:

Datum/Date: 25.11.2015